



저작자표시-동일조건변경허락 2.0 대한민국

이용자는 아래의 조건을 따르는 경우에 한하여 자유롭게

- 이 저작물을 복제, 배포, 전송, 전시, 공연 및 방송할 수 있습니다.
- 이차적 저작물을 작성할 수 있습니다.
- 이 저작물을 영리 목적으로 이용할 수 있습니다.

다음과 같은 조건을 따라야 합니다:



저작자표시. 귀하는 원저작자를 표시하여야 합니다.



동일조건변경허락. 귀하가 이 저작물을 개작, 변형 또는 가공했을 경우에는, 이 저작물과 동일한 이용허락조건하에서만 배포할 수 있습니다.

- 귀하는, 이 저작물의 재이용이나 배포의 경우, 이 저작물에 적용된 이용허락조건을 명확하게 나타내어야 합니다.
- 저작권자로부터 별도의 허가를 받으면 이러한 조건들은 적용되지 않습니다.

저작권법에 따른 이용자의 권리는 위의 내용에 의하여 영향을 받지 않습니다.

이것은 [이용허락규약\(Legal Code\)](#)을 이해하기 쉽게 요약한 것입니다.

[Disclaimer](#)

이학박사학위논문

Raman Scattering of 4-Aminobenzenethiol and Its Analog Molecules on Ag,
Au, and Pt Nanostructures: Contribution of Photoinduced Charge-Transfer

은, 금, 그리고 백금 나노구조체들에 흡착된 4-아미노벤젠티올과
그 유도체 분자들의 라만 산란: 광유도된 전하 전이의 기여

2013 년 2 월

서울대학교 대학원
화학부 물리화학 전공

김 경 록

Raman Scattering of 4-Aminobenzenethiol and Its Analog Molecules on Ag,
Au, and Pt Nanostructures: Contribution of Photoinduced Charge-Transfer

은, 금, 그리고 백금 나노구조체들에 흡착된 4-아미노벤젠티올과
그 유도체 분자들의 라만 산란: 광유도된 전하-전이의 기여

지도교수: 김 관

이 논문을 이학박사 학위논문으로 제출함

2012년 12월

서울대학교 대학원

화학부 물리화학전공

김경록

김경록의 이학박사 학위논문을 인준함

2012년 12월

위 원 장 _____ ①

부위원장 _____ ①

위 원 _____ ①

위 원 _____ ①

위 원 _____ ①

Ph. D. Thesis

Raman Scattering of 4-Aminobenzenethiol and Its Analog Molecules on Ag,
Au, and Pt Nanostructures: Contribution of Photoinduced Charge-Transfer

Supervisor: Professor Kwan Kim

Major: Physical Chemistry

By Kyung Lock Kim

Department of Chemistry

Graduate School of Seoul National University

2013

Abstract

The surface-enhanced Raman scattering (SERS) of 4-aminobenzeneethiol (4-ABT) has seen a surge of interest recently, since its SERS spectral features are dependent not only on the kinds of SERS substrates but also on the measurement conditions. A problem was initially encountered in the interpretation of the SERS spectrum of 4-ABT due to difficulty in correlating several peaks therein with the normal Raman peaks, but the SERS spectral pattern of 4-ABT looked similar to that of 4,4'-dimercaptoazobenzene (4,4'-DMAB). To clarify the issue, the SERS characteristics of 4-ABT and its analog molecules adsorbed on metal surfaces are carefully reinvestigated to understand the charge-transfer chemical enhancement mechanism in this Ph.D. thesis.

In chapter 1, the general overview of the Raman scattering theory and SERS mechanisms are described concisely. SERS is an abnormal surface optical phenomenon resulting in strongly increased Raman signals for molecules adsorbed onto nanostructured coinage metals. In recent years, it has been reported that even single-molecule detection is possible by surface-enhanced resonance Raman scattering (SERRS), suggesting that the enhancement factor (EF) can reach as much as 10^{14} - 10^{15} . Two enhancement mechanisms, one called a long-range electromagnetic (EM) effect and the other called a short-range charge-transfer (CT) chemical effect, are simultaneously operative. Both mechanisms suggest the possibility of enhanced absorption and enhanced photochemistry for surface-adsorbed molecules.

In chapter 2, the current status of SERS studies on 4-ABT are described. For a

long time, 4-ABT, also known as p-aminothiophenol (PATP) or p-mercaptoaniline (pMA), is one of the important surface probe molecules in SERS community and the nanoscience field. The main reasons are that 4-ABT molecules are strongly and easily adsorbed onto the most metal substrates and generate a strong and unique SERS signal which is very sensitive to the type of substrates and measurement conditions. The normal Raman (NR) spectrum of 4-ABT is mostly featureless in the region of $1100\sim 1500\text{ cm}^{-1}$, but three to four peaks appear newly in that region in its SERS spectra. Since these peaks can be assigned to the b_2 -type vibration, which are arising from charge transfer process through the Herzberg-Teller vibronic coupling term, 4-ABT has been regarded for two decades as a model adsorbate for probing the CM effect in SERS. Very recently, however, a number of researchers have come up with a different explanation for the appearance of these b_2 -type bands that the b_2 -type bands appearing in the SERS of 4-ABT must be the N=N stretching vibrations of 4,4'-DMAB produced from 4-ABT via a catalytic coupling reaction on the metal substrates. The elucidation of the SERS characteristics of 4-ABT and its analog molecules including 4,4'-DMAB is thus needed to see another or why we have made a wrong assignment during the past 15 years.

In chapter 3, the SERS characteristics of 4-ABT and 4-ABT adsorbed on Pt nanoparticles are investigated. Pt is a well-known catalyst that has a high catalytic activity. It is found, however, that 4-nitrobenzenethiol (4-NBT) is barely subjected to photoreaction on a Pt surface. On the contrary, the SERS spectra of 4-ABT on Pt clearly show that the b_2 -type bands are increasing in relative intensity toward

shorter wavelength. In addition, the SERS spectral pattern of 4-ABT on Pt is variable not only with changes in the electrode potential but also by altering the excitation wavelength. These spectral variations could be understood by presuming that the chemical enhancement mechanism is also operating in this system, along with the electromagnetic enhancement. Interestingly, similar spectral variation is also observed even under ambient conditions by exposure of 4-ABT on Ag to volatile organic chemicals (VOCs) such as acetone and ammonia. Based on the potential-dependent SERS data, the effect of acetone appeared to correspond to an application of +0.15 V to the Ag substrate vs a saturated Ag/AgCl electrode, while the effect of ammonia corresponded to the application of -0.45 V to Ag.

In chapter 4, as one of several attempts to explore the origin of the b_2 -type bands observable in the SERS of 4-ABT, the pH dependence has been investigated. Consulting the claim that those b_2 -type bands might be associated with a surface-induced photoreaction product such as 4,4'-DMAB, the pH dependence of the SERS spectral feature of 4,4'-DMAB was also examined. Distinct differences were observed in the SERS spectra of 4-ABT and 4,4'-DMAB. The SERS spectral feature of 4,4'-DMAB had virtually no dependence either on the excitation wavelength or on the kind of metal substrate or even on the solution pH. On the other hand, the SERS spectral pattern of 4-ABT displayed substantial changes, depending not only on the excitation wavelength and the kind of SERS substrates but also on the solution pH. It is presumed that when the amine group of 4-ABT is protonated at acidic pHs, the electron population in the benzene ring moiety decreases, resulting in the up-shift of the LUMO level of 4-ABT, as revealed by

UV-vis spectra and from an ab initio calculation, thereby prohibiting the charge transfer resonance chemical enhancement.

In chapter 5, the similarity and dissimilarity in the SERS of 4-ABT and 4,4'-DMAB, along with the SERS spectrum of their analog molecule 4,4'-dimercaptohydrazobenzene (4,4'-DMHAB) were carefully examined. Under ambient conditions, the SERS spectra of 4-ABT, 4,4'-DMAB, and 4,4'-DMHAB on Ag looked in fact comparable to one another, but the spectral dissimilarity was evidenced not only from the SERS spectra taken after treating the probing substrates with a borohydride solution but also from the potential-dependent SERS spectra. It was found that 4,4'-DMAB on Ag could convert to 4-ABT not only by contact with a 100 mM borohydride but also by lowering the potential below -1.0 V. The reverse reaction from 4-ABT on Ag to 4,4'-DMAB appeared insignificant electrochemically as well as photochemically. Furthermore, it was found that the conversion of 4,4'-DMAB to 4-ABT on Ag is a more feasible process upon irradiation with a 514.5-nm (not 632.8-nm) laser under ambient conditions. The SERS spectral pattern of 4,4'-DMAB on Ag varied as a function of laser irradiation time, finally becoming the same as that of 4-ABT on Ag. The photoconversion of 4,4'-DMAB upon 514.5-nm radiation was further confirmed not only by the coupling reaction with 4-cyanobenzoic acid to form amide bonds but also by the selective growth of calcium carbonate.

After considering all the experiments conducted in the work, it is concluded that the appearance of the so-called b_2 -type bands in the SERS of 4-ABT must be attributed wholly to the involvement of the chemical enhancement mechanism, not

due to the formation of 4,4'-DMAB.

Keywords: Raman spectroscopy, surface-enhanced Raman scattering (SERS), electromagnetic mechanism (EM), chemical enhancement mechanism (CM), 4-aminobenzenethiol (4-ABT), 4,4'-dimercaptoazobenzene (4,4'-DMAB)

Student Number: 2009-30846

Contents

Abstract	i
Contents	vi
List of Figures	x
List of Tables	xxi
List of Scheme	xxi
Chapter 1. General Concepts	1
1. Raman Scattering Theory	2
2. Raman Spectroscopy	5
3. Surface-enhanced Raman Scattering (SERS)	7
4. The Electromagnetic Theory of SERS	9
5. SERS from Transition Metal	15
6. The Chemical Enhancement Theory of SERS	18
References	24
Chapter 2. History of 4-Aminobenzenethiol (4-ABT) from SERS Field	28
1. Introduction	29
2. United Experimental Section	34
3. References	40
Chapter 3. The SERS of 4-ABT on Pt and The Volatile Organic Chemicals (VOCs) Effects of 4-ABT on Ag	43
3-1. SERS on Aggregates of Pt Nanoparticles with Definite Size	44

1. Introduction	44
2. Results and Discussion	46
3. Summary and Conclusion	61
4. References	62
3-2. Effect of VOCs on SERS of 4-ABT on Ag: Comparison with the Potential Dependence	65
1. Introduction	65
2. Results and Discussion	68
3. Summary and Conclusion	79
4. References	81
Chapter 4. SERS of 4-ABT And 4,4'-Dimercaptoazobenzene (4,4'- DMAB) on Ag And Au: pH Dependence of b₂-Type Bands	84
1. Introduction	85
2. Results and Discussion	87
3. Summary and Conclusion	97
4. References	98
Chapter 5. Similarity and Dissimilarity in SERS of 4-ABT And Its Analog molecules	100
5-1. Similarity And Dissimilarity in SERS of 4-ABT, 4,4'-DMAB, And 4,4'- Dimercaptohydrazobenzene (4,4'-DMHAB) on Ag	101
1. Introduction	101
2. Results and Discussion	104

3. Summary and Conclusion	118
4. References	119
5-2. Photoreduction of 4,4'-DMAB on Ag Revealed by Raman Scattering Spectroscopy	122
1. Introduction	122
2. Results and Discussion	125
3. Summary and Conclusion	138
4. References	142
5-3. Visible-Light Response of 4-ABT and 4,4'-DMAB Silver Salts	145
1. Introduction	145
2. Results and Discussion	147
3. Summary and Conclusion	160
4. References	161

IV. Appendix

1. List of Publications	164
2. List of Presentations	167
Abstract (Korean)	169

List of Figures

Chapter 1

Figure 1. Light scattering by an induced dipole moment due to an incident EM wave.

Figure 2. Diagram of the Rayleigh and Raman scattering processes.

Figure 3. Schematic of plasmon oscillation for a particle, showing the displacement of the conduction electron charge cloud relative to the nuclei.

Figure 4. (a) Dielectric constants of Ag and Pt. (b) Dependence of the surface enhancement factor (G) for two-dimensional Ag and Pt nanospheroids array on the wavelength of the incident plane wave. The semiminor axis and aspect ratio of spheroids are 20 nm and 2:1, respectively. The probe molecule is assumed to be located at the tip of spheroids.

Figure 5. (a) Energy level scheme for molecule-metal system. The discrete molecular levels are I and K, between which a transition is assumed to be allowed. The continuous metal levels of the conduction band of the metal are shown on the left. The conduction band ranges between ω_A and ω_B and is assumed to have a constant density of states ρ_0 . The filled levels range up to ω_F , the Fermi level, and are depicted by lines, while the unfilled levels are depicted by dots. (b) The scheme for molecule-to-metal CT transitions between the ground molecular state and unfilled levels of the metal. Transition borrows intensity from the allowed transition by means of vibronic coupling between metals and the excited molecular

level through the matrix element h_{MK} . (c) The scheme for metal-to-molecule CT transitions between filled level of the metal and the excited molecular state. The transition borrows intensity from the allowed transition by means of vibronic coupling between metal levels and the ground molecular state through the matrix element h_{IM} .

Chapter 3-1

Figure 1. (a) TEM images of four different Pt nanoparticles and (b) their histograms; the magnified TEM images of 46 nm sized and 105 nm sized Pt nanoparticles are also shown in the insets. (c) UV-vis extinction spectra of Pt nanoparticles in a colloidal state (particle concentrations are the same in all spectra) and (d) the peak maximum drawn versus the size of Pt nanoparticles.

Figure 2. (a) UV-vis spectra of Pt S6 films assembled on ITO: See text. (b) FE-SEM images of Pt S6 films assembled on silicon wafers. (c) CVs of Pt S6 films in 0.1 M H₂SO₄ solution (scan rate) 0.05 V/s) (d) CVs of Pt S1 ~ S6 films fabricated using 105 nm sized Pt particles. (e) Cathodic current in (c) drawn versus size of Pt particles used in fabricating S6 films.

Figure 3. (a) Raman spectra of BT adsorbed on four different Pt S6 films, i.e., S6(Pt-28 nm)/ITO, S6(Pt-46 nm)/ITO, S6(Pt-72 nm)/ITO, and S6(Pt-105 nm)/ITO films, measured at 514.5 nm excitation: For comparison, the NR spectrum of BT in the neat state is also shown. (b) Peak intensity of ν_{8a} band of BT (normalized with respect to that of a silicon wafer at 520 cm⁻¹) measured at 514.5 nm excitation

drawn versus the number of layers (S1 ~ S6) of four different Pt particles. (c) Normalized peak intensity of the ν_{8a} band of BT on S6 films drawn versus the size of Pt nanoparticles, as well as the excitation wavelengths.

Figure 4. XRDs of (a) S6(Pt-7 nm) and (b) S6(Pt-105 nm) films assembled on silicon wafers: For comparison, the XRDs of (c) Pt laser ablated sol film and (d) a polycrystalline Pt foil are also shown.

Figure 5. SERS spectra of 4-ABT on S6(Pt-105 nm)/ITO film taken using (a) 488, (b) 568, and (c) 632.8 nm radiation as the excitation source: (d) NR spectrum of 4-ABT in neat solid state taken at 568 nm excitation.

Figure 6. (a) NR spectrum of 4-NBT in neat solid state and (b) SERS spectrum of 4-NBT on S6(Pt-105 nm)/ITO film measured at 488 nm excitation. SERS spectra of 4-ABT on S6(Pt-105 nm)/ITO measured under (c) static and (d) spinning at 3000 rpm at 488 nm excitation.

Figure 7. Potential-dependent SERS spectra of 4-ABT on S6(Pt-105 nm)/ITO measured using (a) 488, (b) 568, and (c) 632.8 nm radiation as the excitation source.

Figure 8. Normalized peak intensity of ring 19b band at 1439 cm^{-1} in Figure 7 drawn versus the electrode potential at (a) 488 or (b) 568 or (c) 632.8 nm excitation: Solid lines represent the Gaussian fitting.

Figure 9. CVs of (a) 4-ABT and (b) 4-NBT on S6(Pt-105 nm)/ITO in 0.1 M, NaClO_4 aqueous solution. The solid and dashed lines show the first and second cycles, respectively.

Chapter 3-2

Figure 1. (a) TEM image of Ag nanoparticles and (b) a histogram of the particle size distribution. (c) FE-SEM image of Ag nanoaggregates in a film state. (d) UV-vis extinction spectra of Ag nanoparticles in colloid (broken line) and film (full line) states.

Figure 2. (a) NR of 4-ABT in a neat solid state and (b) its SERS spectra on Ag measured under the flow of N₂ using 488, 514.5, 568, and 632.8 nm radiation as the excitation sources, and (c) the normalized peak intensities of the 3, 9b, and 19b bands relative to the 7a band in (b) drawn versus the excitation wavelength.

Figure 3. SERS spectra of 4-ABT on Ag measured under the flow of (a) acetone and (b) ammonia using 488, 514.5, 568, and 632.8 nm radiation as the excitation sources. (c) Normalized intensities of 19b, 9b, and 3 bands relative to 7a band, plotted in terms of VOCs and excitation wavelengths used in this study. (d) The intensity ratio of the 19b to 7a bands determined under the alternative flow of NH₃ and N₂.

Figure 4. Cyclic voltammograms measured at a scan rate of 50 mV s⁻¹, using either a bare Ag or 4-ABT-adsorbed Ag or dodecanethiol adsorbed Ag electrode soaked in an aqueous solution composed of 0.1 M KCl and 1 mM K₃Fe(CN)₆.

Figure 5. Potential-dependent SERS spectra of 4-ABT adsorbed on Ag nanoparticles on an ITO electrode, measured in 0.1 M NaClO₄ using (a) 488, (b) 514.5, and (c) 632.8 nm radiation as the excitation sources. (d) Relative intensities of ring 19b and 7a bands drawn against the electrode potential in (a)–(c). Three sets of normalized 19b intensities determined under the flow of acetone or nitrogen or ammonia are

overlapped in (d), marking the regions of best overlap in dotted lines (see the filled circles, triangles, and squares).

Chapter 4

Figure 1. NR spectra of 4-ABT (a) in neat solid state and aqueous solution at pH (b) 3 and (c) 10. NR spectra of 4,4'-DMAB (d) in neat solid state and aqueous solution at pH (e) 4 and (d) 10.

Figure 2. (a) TEM images and (b) UV-vis spectra of Au and Ag nanoparticles in as-prepared state. (c) UV-vis spectra of Au and Ag nanoparticles films assembled on 3-APS-modified glass substrates.

Figure 3. SERS spectra of 4-ABT on Ag measured in ambient conditions in air using (a) 514.5 and (b) 632.8 nm radiation as the excitation source, and (c) SERS spectrum of 4-ABT on Au taken under similar condition at 632.8 nm. SERS spectra of 4,4'-DMAB on Ag measured in ambient conditions in air using (d) 514.5 and (e) 632.8 nm radiation as excitation source, and (f) SERS spectrum of 4,4'-DMAB on Au taken under similar conditions at 632.8 nm.

Figure 4. SERS spectra of 4-ABT on Ag taken at pH 10 and 2 using (a) 514.5 (b) 632.8 nm radiation as the excitation source. (c) SERS spectra of 4-ABT on Au taken at pH 10 and 2 using 632.8 nm radiation as the excitation source. (d) Relative intensity of a typical b_2 -type band at $\sim 1437\text{ cm}^{-1}$ (19b) and an a_1 band at $\sim 1076\text{ cm}^{-1}$ (7a) measured following repeated changes in the solution pH between 10 and 2.

Figure 5. SERS spectra of (a) 4,4'-DMAB and (b) 4-ABT on Au measured as a

function of solution pH using 632.8 nm radiation as the excitation source. (c) Relative intensity of the band at $\sim 1437\text{ cm}^{-1}$ and the band at 1076 cm^{-1} , drawn versus the solution pH for both spectra in (a) and (b).

Figure 6. UV-vis spectra of 4-ABT at various solution pHs.

Chapter 5-1

Figure 1. (c) TEM image of Ag nanoparticle film. (d) UV – vis extinction spectra of Ag nanoparticles in the colloidal state (solid line) and in the film state (dot line).

Figure 2. (a) NR spectra of 4,4'-DMAB, 4-ABT, and 4,4'-DMHAB in the neat state taken using 488 nm radiation as the excitation source. SERS spectra of 4,4'-DMAB, 4-ABT, and 4,4'-DMHAB on Ag taken under ambient conditions using (b) 488, (c) 514.5, and (d) 632.8 nm radiation as the excitation sources.

Figure 3. (a) Normalized peak intensities of 7a analogue-bands in Figure 2b–d drawn versus the excitation wavelength. Intensities of (b) 19b, (c) 3, and (d) 9b analogue-bands with respect to that of the 7a analogue-band in Figure 2b–d drawn versus the excitation wavelength.

Figure 4. (a) A series of SERS spectra of 4,4'-DMAB on Ag taken under ambient conditions after soaking for 10 min in a solution of borohydride at different concentrations. Excitation wavelength was 632.8 nm. (b) Intensity of the 7a analogue-band at 1072 cm^{-1} in panel a, drawn versus the concentration of borohydride. For comparison, authentic intensities of the 7a analogue-bands of 4,4'-DMAB (black) and 4-ABT (white) are shown together. (c) Intensity of the 19b

analogue-band with respect to that of the 7a analogue-band drawn versus the concentration of borohydride. For comparison, relative intensities of the authentic bands of 4,4'-DMAB (black) and 4-ABT (white) are shown together. (d) Spectral comparison of 4-ABT on Ag (thick line) with that of 4,4'-DMAB on Ag after treatment with a 100 mM solution of borohydride (gray line); see, for comparison, the authentic SERS spectrum of 4,4'-DMAB on Ag (thin line); all SERS spectra were normalized with respect to the intensity of the 7a analogue-band.

Figure 5. (a) pH dependency of SERS spectrum of 4,4'-DMAB on Ag measured before and after being soaked in a 100 mM borohydride solution: Excitation wavelength was 632.8 nm. (b) Variation of the 19b analogue-band intensity with respect to that of the 7a analogue-band measured as a function of time at pH 2 (filled circles) and 10 (open circles) before and after treating with borohydride.

Figure 6. (a) Potential-dependent SERS spectra of 4,4'-DMAB on Ag in 0.1 M NaClO₄ solution taken using 488, 514.5, and 632.8 nm radiation as the excitation sources. Spectra in red were measured from 0.0 V after excursing first down to -1.2 V. (b) Variation of the 19b analogue-band intensity with respect to that of the 7a analogue-band in panel a, drawn versus the potential applied: the filled triangles correspond to the data observable under the very first measurement; the empty triangles correspond to the data observable after the potential was excursed once down to -1.2 V; the filled circles represent the data measured separately for 4-ABT on Ag.

Figure 7. (a) Potential-dependent SERS spectra of 4,4'-DMAB adsorbed on Ag measured after being soaked for 10 min in a 100 mM borohydride solution taken

using 488, 514.5, and 632.8 nm radiation as the excitation sources. (b) Variation of the 19b analogue-band intensity with respect to that of the 7a analogue-band in panel a, drawn versus potential applied (empty circles); see, for comparison, the data obtained from the authentic SERS spectra of 4-ABT (filled circles) and 4,4'-DMHAB (filled squares) on Ag.

Figure 8. (a) Potential-dependent SERS spectra of 4,4'-DMHAB on Ag in 0.1 M NaClO₄ solution taken using 488, 514.5, and 632.8 nm radiation as the excitation sources. (b) Variation of 19b analog-band intensity with respect to that of 7a analog-band in (a) drawn versus potential applied: the filled triangles and empty triangles correspond to the data observable under the first forward and second backward sweep measurement, respectively.

Chapter 5-2

Figure 1. (a) FE-SEM image of Ag nanoparticle film (b) UV-vis extinction spectra of Ag nanoparticles in the colloidal state (solid line) and film state (dashed line). SERS spectra of BT on Ag nanoparticle film measured using (c) 514.5-nm and (d) 632.8-nm radiation as the excitation source. Insets show the variation of the SERS peak intensity as a function of laser irradiation time.

Figure 2. NR spectra of 4-ABT in the neat state measured using (a) 514.5-nm and (b) 632.8-nm radiation as the excitation source. NR spectra of 4,4'-DMAB in the neat state measured using (c) 514.5-nm and (d) 632.8-nm radiation as the excitation source.

Figure 3. SERS spectra of (a) 4-ABT and (b) 4,4'-DMAB on Ag nanoparticle film measured using 514.5-nm radiation as the excitation source. Spectra measured over time are shown by different lines. (c) Normalized peak intensities of 7a-analog bands in (a) (empty circles) and (b) (filled circles) shown versus laser irradiation time. (d) The data shown in (c) corrected for the degradation of the SERS activity of the Ag film by referring to the SERS data of BT in Figure 1(c). (e) Relative intensity of the 19b- to 7a-analog bands in (a) and (b) shown versus laser irradiation time.

Figure 4. (a) SERS spectra of 4-ABT and 4,4'-DMAB on Ag measured before an EDC coupling reaction with 4-CBA. (b) SERS spectrum of 4-ABT on Ag measured after an EDC coupling reaction with 4-CBA. The EDC coupling reaction was performed for 30 min by injecting 0.02 M 4-CBA in DMF containing 0.02 M EDC into a glass capillary coated with 4-ABT-adsorbed Ag nanoparticle film. SERS spectra of 4,4'-DMAB on Ag measured after EDC coupling (c) without irradiation and (d) following 514.5-nm laser irradiation for 2.5 h.

Figure 5. FE-SEM images of calcite crystals grown on (a) 4-ABT and (b) 4,4'-DMAB on roughened Ag foil. Inset shows the magnified image of (b).

Figure 6. FE-SEM images of calcite crystals grown on 4,4'-DMAB on roughened Ag foil after irradiation with a 514.5-nm laser beforehand at different locations, each with either one, two, three, or four spots. Inset shows the Raman spectrum of the grown calcite.

Figure 7. SERS spectra of (a) 4-ABT and (b) 4,4'-DMAB on Ag nanoparticle film

measured using 632.8-nm radiation as the excitation source. Spectra measured over time are shown by different lines. (c) Normalized peak intensities of 7a-analog bands in (a) (empty circles) and (b) (filled circles) shown versus laser irradiation time. (d) The data shown in (c) corrected for the degradation of the SERS activity of the Ag film by referring to the SERS data of BT in Figure 1(d). (e) Relative intensity of the 19b- to 7a-analog bands in (a) and (b) shown versus laser irradiation time.

Chapter 5-3

Figure 1. FE-SEM images of (a) Ag-4ABT and (b) Ag-4,4'DMAB, and XRD patterns of (c) Ag-4ABT and (d) Ag-4,4'DMAB. Insets in (c) and (d) display the interlayer spacings derived from different XRD reflections.

Figure 2. Schematic structures of (a) Ag-4ABT and (b) Ag-4,4'DMAB, and (c) their TGA and DSC data.

Figure 3. Raman spectra of (a) 4-ABT, (b) Ag-4ABT, (c) 4,4'-DMAB, and (d) Ag-4,4'DMAB measured using 514.5 nm radiation for excitation. The salt spectra in (b) and (d) were measured with spinning at 3000 rpm.

Figure 4. Temporally evolved Raman spectra of (a) Ag-4ABT and (b) Ag-4,4'DMAB under 514.5 nm light illumination and static conditions. Spectra measured over time are shown by different lines. (c) Temporal variation of the normalized peak intensities of the a₁-analog band at $\sim 1080\text{ cm}^{-1}$ for Ag-4ABT (empty circles) and Ag-4,4'DMAB (filled circles) shown versus laser irradiation

time. (d) Temporal variation of the relative intensity of the b_2 -analog bands at $\sim 1433\text{ cm}^{-1}$ with respect to the a_1 -analog band at $\sim 1080\text{ cm}^{-1}$ in (a) and (b) shown versus laser irradiation time.

Figure 5. TEM images of Ag nanoparticles obtained from the photolysis of (a) Ag-4ABT and (b) Ag-4,4'DMAB using 514.5 nm radiation as excitation source, (c) Ag-4ABT and (d) Ag-4,4'DMAB using 632.8 nm radiation as excitation source, respectively.

Figure 6. Temporally evolved Raman spectra of (a) Ag-4ABT and (b) Ag-4,4'DMAB under 632.8 nm light illumination and static conditions. Spectra measured over time are shown by different lines. (c) Temporal variation of the normalized peak intensities of the a_1 -analog band at $\sim 1080\text{ cm}^{-1}$ for Ag-4ABT (empty circles) and Ag-4,4'DMAB (filled circles) shown versus laser irradiation time. (d) Temporal variation of the relative intensity of the b_2 -analog bands at $\sim 1433\text{ cm}^{-1}$ with respect to the a_1 -analog band at $\sim 1080\text{ cm}^{-1}$ in (a) and (b) shown versus laser irradiation time.

Figure 7. (a) The first-order kinetic plot for the photoreduction of Ag-4,4'DMAB to 4-ABT on Ag; I_t , $I_{t=0}$, and $I_{t=\infty}$ are the intensity ratios of the b_2 -analog band at $\sim 1433\text{ cm}^{-1}$ and the a_1 -analog band at $\sim 1080\text{ cm}^{-1}$ measured at time t , $t=0$, and $t=\infty$, respectively, after the irradiation of the 514.5 nm light at five different laser powers. (b) Log-log plot of the slope in (a) versus the laser power.

List of Tables

Table 1. Raman spectral peaks of 4-Aminobenzenethiol measured in free and surface adsorbed states using the excitation laser of 488, 514.5, and 632.8 nm.

Table 2. Normalized intensities of 19b, 3, and 9b bands relative to the 7a band measured under various VOCs at different excitation wavelengths in this study.

Table 3. Binding energies of acetone and ammonia interacting with a single Ag atom, and the accompanying change in the net charges of the Ag atom.

Table 4. Vibrational assignments for the normal Raman and SERS spectra of 4,4'-DMAB and 4-ABT.

List of Schemes

Scheme 1. A schematic diagram showing how to measure the effect of VOCs on the SERS of 4-ABT adsorbed on an Ag nanoparticle film on mica.

Scheme 2. Structure formula of 4-ABT, 4,4'-DMAB, and 4,4'-DMHAB.

Scheme 3. Schematic representation of the photoreduction of 4,4'-DMAB on Ag to 4-ABT.

Chapter 1

General Concepts

1-1. Raman Scattering Theory

The scattering of light may be thought of as the redirection of light that takes place when an electromagnetic wave as an incident light ray encounters an obstacle or non-homogeneity, normally the scattering material as solid, liquid or gas [1]. As the electromagnetic wave interacts with the matter, the electron orbits within the constituent molecules are perturbed periodically with the same frequency (ν_0) as the electric field of the incident wave [1]. The oscillation or perturbation of the electron cloud results in a periodic separation of charge within the molecules, which is called an induced dipole moment. As illustrated in Figure 1, the oscillating induced dipole moment is manifest as a source of electromagnetic radiation, thereby resulting in scattered light. The majority of light scattered is emitted at the identical frequency (ν_0) of incident light, a process referred to as elastic scattering. However, additional light is scattered at different frequencies, a process referred to as inelastic scattering. Since the discovery of Sir, C. V. Raman in 1927, Raman scattering is one such example of inelastic scattering [1-2].

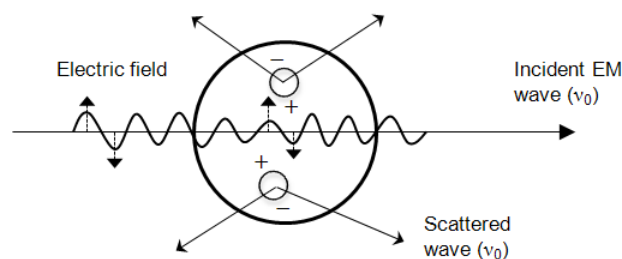


Figure 1. Light scattering by an induced dipole moment due to an incident EM wave

As can be seen in Figure 1-1, an incident electromagnetic wave induces a dipole moment during the light-material interaction [1]. The strength of the induced dipole

moment, P , is given by

$$P = \alpha \bar{E} \quad (1)$$

where α is the polarizability and \bar{E} is the strength of electric field of the incident electromagnetic wave. The polarizability is material property that depends on the molecular structure and nature of the bonds. For the incident electromagnetic wave, the electric field may be expressed as

$$\bar{E} = E_0(\cos 2\pi\nu_0 t) \quad (2)$$

where ν_0 is the frequency (Hz) of the incident electromagnetic ($\nu_0 = c / \lambda$). Substituting Equation (2) into (1) yields the time-dependent induced dipole moment,

$$P = \alpha E_0(\cos 2\pi\nu_0 t) \quad (3)$$

because the ability to perturb the local electron cloud of a molecule structure depends on the relative location of the individual atoms, it follows that polarizability is a function of the instantaneous position of constituent atoms. For any molecular bond, the individual atoms are confined to specific vibrational modes, in which the vibrational energy levels are quantized in a manner similar to electronic energies. The vibrational energy of a particular mode is given by

$$E_{\text{vib}} = \left(j + \frac{1}{2}\right) h\nu_{\text{vib}} \quad (4)$$

where j is the vibrational quantum number ($j = 0, 1, 2, \dots$), ν_{vib} is the frequency of the vibrational mode, and h is the Planck constant. The physical displacement dq of the atoms about their equilibrium position due to the particular vibrational mode

may be expressed as

$$dQ = Q_0 \cos(2\pi\nu_0 t) \quad (5)$$

where Q_0 is maximum displacement about the equilibrium position. For a typical diatomic molecule as N_2 , the maximum displacement about 10% of the bond length. For such a small displacement, the polarizability may be approximated by Taylor series expansion, That is,

$$\alpha = \alpha_0 + \left(\frac{\partial\alpha}{\partial Q}\right) dQ \quad (6)$$

where α_0 is the polarizability of the molecular mode at equilibrium position. Based on the vibrational displacement of Equation (5), the polarizability may be given as

$$\alpha = \alpha_0 + \left(\frac{\partial\alpha}{\partial Q}\right) Q_0 \cos(2\pi\nu_0 t) \quad (7)$$

Finally, Equation (7) may be substituted into Equation (3), which yields

$$P = \alpha \bar{E}_0 \cos(2\pi\nu_0 t) + \left(\frac{\partial\alpha}{\partial Q}\right) Q_0 E_0 \cos(2\pi\nu_0 t) \cos(2\pi\nu_{\text{vib}} t) \quad (8)$$

Using a trigonometric identity, the above relation may be recast as

$$P = \alpha \bar{E}_0 \cos(2\pi\nu_0 t) + \left(\frac{\partial\alpha}{\partial Q}\right) \left(\frac{Q_0 E_0}{2}\right) [\cos\{2\pi(\nu_0 - \nu_{\text{vib}})t\} + \cos\{2\pi(\nu_0 + \nu_{\text{vib}})t\}] \quad (9)$$

Examination of the above equation reveals that induced dipole moments are created at three distinct frequencies as in Figure 2, that is, ν_0 is $(\nu_0 - \nu_{\text{vib}})$, and $(\nu_0 + \nu_{\text{vib}})$, which results in scattered radiation at these same three frequencies. The first scattered frequency corresponds to the incident frequency, hence is elastic scattering (e.g. Mie or Rayleigh), while the latter two frequencies are shifted to lower or higher frequencies and are therefore inelastic processes. The scattered

light in these latter two cases is referred to as Raman scattering, with the down-shifted frequency or longer wavelength referred to as Stokes scattering, and the up-shifted frequency or shorter wavelength referred to as anti-Stokes scattering [1-2].

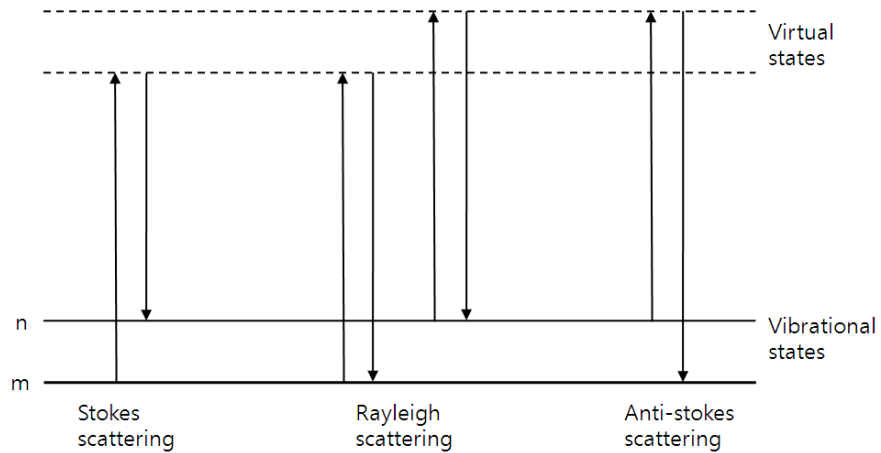


Figure 2. Diagram of the Rayleigh and Raman scattering processes.

1–2. Raman Spectroscopy

In practice, Raman spectroscopy is generally performed with a laser as the excitation source because this intense, collimated monochromatic light source enables measurement of relatively small Raman shifts, while the intense beam allows for improved spatial resolution and signal-to-noise ratio [2]. In general, the Raman signal intensity is orders of magnitude weaker than the elastic scattering intensity, hence stray light can be a considerable issue. For instance, diatomic nitrogen (N_2) has an elastic scattering cross-section (i.e. Rayleigh scattering) of $8.9 \times 10^{-28} \text{ cm}^2/\text{sr}$, and a Raman scattering cross-section of $5.5 \times 10^{-31} \text{ cm}^2/\text{sr}$, at the 488 nm wavelength excitation source [2]. Therefore, the Raman scattering signal is more than 1,000 times weaker than the Rayleigh scattering signal. For solids, this

difference can be more than 10^6 . While spectrometers are commonly used to separate the elastic scattering and Raman scattering signals, the large mismatch in scattering intensity can enable the elastically scattered light to dominate the Raman light via stray light. Therefore, notch filters or edge filters (This is called sharp cut-off high pass filters) are used to reject the elastically scattered light prior to entering the spectrometer. Selection of the excitation (or) laser wavelength source depend on several factors. The Raman differential scattering cross-section (cm^2/sr) varies inversely with the fourth power of the excitation wavelength by the proportionality formula [2],

$$\sigma' \propto (\nu_0 - \nu_{\text{vib}})^4,$$

where ν_0 is the wavenumber of the incident radiation ($1/\lambda_0$) and ν_{vib} is the wavenumber of the vibrational mode (ν_{vib}/c). The common unit for wavenumber (here is considered a unit of energy) is the cm^{-1} , and ν_{vib} generally ranges from about 200~4000 cm^{-1} . The N_2 such as discussed above has a fundamental vibrational mode corresponding to $\nu_{\text{vib}} = 2331 \text{ cm}^{-1}$. The cross-section of $5.5 \times 10^{-31} \text{ cm}^2/\text{sr}$ at 488 nm laser wavelength would be reduced to $1.7 \times 10^{-31} \text{ cm}^2/\text{sr}$ at 632.8 nm laser wavelength, a reduction of more than a factor of 3 [2]. Therefore, selecting a shorter laser wavelength can increase the Raman scattering cross-section. However, as laser energies reach into the shorter visible and UV wavelength range, fluorescence (That is, a different inelastic scattering process in which incident photons are absorbed, undergo internal conversion, and are subsequently re-emitted at longer wavelengths) can become pronounced, which

may interface with weaker Raman signals. Moreover, the Raman shift is constant with regard to vibrational energy, hence constant in wavenumber, but not wavelength. To better understand for a Raman shift, consider again the N_2 vibrational mode of $\nu_{\text{vib}} = 2331 \text{ cm}^{-1}$. An incident wavelength of 355 nm would be shifted to a wavelength of 387 nm, for a difference of 32 nm. Alternately, an incident wavelength of 632.8 nm would be shifted to a wavelength of 741.2 nm, for a difference of 108.4 nm. A greater Raman shift makes separating the elastically scattered and Raman scattered light much easier, possibly resulting in improved signal-to-noise ratios and the ability to measure smaller Raman Shifts [2]. In the summary, the Raman excitation wavelength should be selected in consideration of the Raman scattering cross-section, the magnitude of the Raman shifts in wavelength, and the potential for fluorescence.

1–3. Surface-enhanced Raman Scattering (SERS)

Conventional Raman spectroscopy is a powerful technique for determining structural information about a molecular system itself, but, the small cross section of Raman scattering typically results in low resolution and (or) the need for high concentrations of analyte. For analytes near rough metal surfaces, the signal can be enhanced due to the strong local field arising from the plasmon excitation combined with the direct chemical interactions between the molecule and the metal surface. This is known as a surface-enhanced Raman scattering (SERS) phenomenon as well as it is one of the strongest and most enigmatic effects in physics and optics [3-4]. Historically, SERS phenomenon was first observed from

pyridine molecule adsorbed on a electrochemically roughed silver electrode system by Fleischman et al. in 1974, the unusual intensity of the Raman signals was attributed to the increased surface area of the rough substrate [5]. However, they did not find the scattered intensity particularly remarkable, attributing it to the many absorption sites available on a highly roughened (fractal like) surface and the possibility of multilayer adsorption at the time. Since then, it was Van Dyne and Creighton who point out that the intensification of the effective Raman cross section was far in excess of the increased number of molecules interrogated as a result of the surface's roughness factor, as well as the magnitude of the Raman scattering signal can be greatly enhanced (enhancements of $10^5 \sim 10^6$) when the very low concentrations of molecule is placed on or near a roughened silver substrate [6,7]. In 1978, Moskovits was also proposed new theory that the huge increase in Raman cross section was a result of the excitation of surface plasmons [8]. That is, strong electromagnetic fields are generated when the localized surface plasmon resonance (LSPR) of diverse metal nano-scale architectures, such as it have a specific shape metal nanoparticles, and metal pattern by e-beam lithography and so on. For this reason, SERS can be generally observable in coinage metals as silver, gold, and copper, then transition metals such as platinum, palladium, and ruthenium, and even the other poorly conducting materials.

Recently another area of great interest in the SERS field concerns the observation of single molecules SERS (SMSERS). Two independent reports in 1997 [9,10], on the observation of single molecule (SM) detection using SERS triggered a renewed interest in this technique, due to the enhancement factor can be as much as 10^{14} to

10^{15} for dye molecules including the contribution of the resonance Raman scattering. But it is very difficult to providing wide spread applicability so far because the limited numbers of molecules and substrates for which successful observations have been made. Especially, almost all of the observations to date have been with dye molecules such as rhodamine 6G (R6G) or crystal violet (CV), which specifically have larger Raman intensities for non-SERS applications than non-resonant molecules like aromatic thiols as likely benzenethiol by factors of 10^4 or more [11]. Moreover, for some kind of substrates that SMSERS earned larger signal limited in colloidal aggregate structure. That is, a greater understanding of SMSERS and (or) SERS with LSPR properties is still needed to facilitate the transition to the area of applications in the future work [11-13]. Nevertheless, due to its great sensitivity and strongly enhanced signal, SERS has still been proposed for a variety of ultrasensitive chemical and biological sensing applications [12,13]. More recently, sensing application of SERS was even studied on plasmonic transport properties which the converted light into surface plasmon propagating along nanometer scale noble metal nanowires, which are then back-converted into visible light after traveling distances of many microns [14,15].

1–4. The Electromagnetic Theory of SERS

Generally, it has long been believed that two enhancement mechanisms in SERS, There are two primary theories that can account for the signal enhancement, one being the electromagnetic field enhancement (EM) theory and the other being the chemical enhancement (CM) theory [3-12]. The EM mechanism is based on the

excitation of localized surface plasmons (LSPR), while the CM mechanism assumes the formation of charge-transfer complexes [3-12]. Normally, the EM mechanism is responsible for the major contribution to the SERS enhancement [3-12].

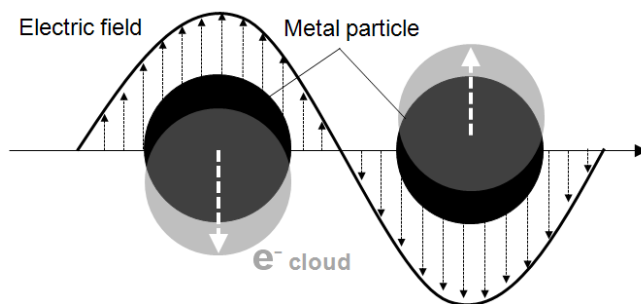


Figure 3. Schematic of plasmon oscillation for a particle, showing the displacement of the conduction electron charge cloud relative to the nuclei.

As can be seen in Figure 3, to understand the electromagnetic enhancement, a small metal isolated particle as one model system is useful in defining of the basic standard in order to see intense SERS [8, 16]. A surrounding illuminated small metal particle will sustain oscillating surface plasmon multi-dipoles induced by electric field of the incident light. The surface plasmons are collective oscillations of the conduction electrons against the background of ionic metal cores [8]. Moreover, incident light can induce a host of other excitations in the metal particle interband transitions. For a particle much smaller than the wavelength of the exciting light, the dipolar plasmon can be ignored. Therefore, a small particle systems with most of free electron gas will be sustained such excitations. When the exciting laser light is resonant with the dipolar plasmon, the metal particle will radiate light characteristic of dipolar radiation. This radiation is a coherent process

with exciting field and is characterized by a spatial distribution of field magnitudes in which the light intensity from certain portions of space surrounding the particle is enhanced. Finally, when electromagnetic radiation with the same frequency is incident upon the metal particle, the electric field of radiation drives the conduction electrons into collective oscillation. Electromagnetic fields depend on Raman active molecules being confined within these electromagnetic fields. In addition, simple theoretical modeling in physical view has been expressed to provide insight into SERS with electromagnetic enhancement by noble metal particles [8,17,18]. Therefore, it can be also expressed to the field enhancement averaged over the surface of the particle, g . [8]

$$E_S = gE_0$$

where E_S is the average magnitude of the near field at the metal particle surface, E_0 is the magnitude of the incident field. The average molecule adsorbed on metal particles surface will be excited by a field E_S , and the Raman scattered light produced by molecule will have a field strength is $E_R \propto \alpha_R E_S \propto \alpha_R g E_0$, where α_R is the appropriate combination of components of the Raman tensor. And then, metal particle can scatter light at the Raman-shifted wavelength enhanced by a factor, g' . The amplitude of the SERS-scattered field will therefore be given by

$$E_{\text{SERS}} \propto \alpha_R g g' E_0$$

and the average SERS intensity can be proportional to the square molecules of E_{SERS} . That is, $I_{\text{SERS}} \propto |\alpha_R|^2 |g g'|^2 I_0$, where I_{SERS} and I_0 are the intensities of SERS-scattered and incident fields, respectively. For low frequency bands when

$g \cong g'$ the SERS intensity will be enhanced by a factor proportional to the fourth power of the enhancement of the local incident near field, $|E_L|^4 = |g^4|$, while the Raman modes for higher frequency of SERS intensity will be a more complicated function of the plasmon resonant properties of the metal particle according to the precise wavelengths at which the incident and Raman scattered light fall. It has been reported that for fractal aggregates the correct sum over the cluster leads to a $|E_L|^3$ rather than the fourth power of the local field [18]. Therefore, it is defined the SERS enhancement G as the ratio of the Raman scattered intensity in the presence of the metal particle to its value in the absence of the particle,

$$G = \left| \frac{\alpha_R}{\alpha_{R_0}} \right| |gg'|^2,$$

where α_R is the Raman polarizability of the isolated molecule. For example, about silver at 400 nm, g is only ~ 30 , that applied to a Raman enhancement $G \sim 8 \times 10^{-5}$ assuming the Raman polarizability to be unchanged from that isolated molecule. SERS excitation is near field phenomenon in especially near a metal surface. It can also have spatial components that decay more rapidly with distance than the spatial variation in the far field. Therefore, actually it may be observed that normally forbidden vibrational modes and dipole-forbidden fluorescences to occur in the SERS spectrum. However, practical SERS active systems are consist of interacting two particles, its more SERS active than only a single particle [3-19]. As noted above, it is well established that single nanoparticles with a complex shape can give sizable enhancement, in particular when the molecule is placed in crevices [17-20]. Larger aggregates of metallic nanoparticles have been used as SERS

substrates for a long time [17-20]. Recently, it has been also shown that they can give enhancement factors high enough to allow single molecule detection, very likely without any molecular resonance Raman contribution [11-13]. These aggregates have a fractal nature. It has been demonstrated, both theoretically and experimentally, that fractal metal-particle aggregates are capable of inhomogeneously redistributing in their volume the intensity of an EM field acting on them, thus creating regions of very high electric field, named “Hot spots” [17-31]. In SERS of a molecule adsorbed on a fractal aggregate, one should distinguish between two EM enhancement mechanisms: first is the structure of the aggregate in close proximity of the chromophore provides an enhancement due, for instance, to crevices, very similar to what happens for isolated particles dimers. Second is the aggregate as a whole is responsible for the existence of hot spots involving different metal particles. At any rate, theories of SERS that immediately followed its discovery considered molecules bound to metal spheroids [21-24]. Hemispheroids on flat surfaces was model emulating rough surfaces [25]. A general formula expressing the SERS intensity enhancement for molecule bound at a position r_0 in terms of local $E(r)$ at this location,

$$g^R = \left(\frac{|E(r)|^2}{|E_0|^2} \right)^2, \quad (1)$$

where $|E_0|^2$ is the excitation electric optical field amplitude. In this expression a factor of

$$I(r) \equiv \frac{|E(r)|^2}{|E_0|^2} \quad (2)$$

takes into account the enhancement of the excitation rate due to the local field intensity increase by $I(r)$ times. The common problem with SERS models based on spheroids is that the enhancement, in accord with (1), surface plasmon resonance peak, while experimentally when the SERS enhancement is giant, $g^R \gtrsim 10^5$, its spectral maximum is broad and shifted to the red (near-infrared) region [8]. To explain such a behavior, it has been proposed that it is due to aggregates of nanoparticles. First, the simplest of such aggregates, a dimer of nanospheres, was considered [26]. There was a significant red shift of the SERS enhancement predicted in such dimers when the surface-to-surface distance between the individual spheres becomes small relative to their sizes. However, the enhancement spectral peaks still were narrow, and the magnitude of enhancement was not as large as in experiments. Generally, fractal-like clusters in aggregates are experimentally the most efficient enhancers of SERS [27], have specific properties conducive to the giant SERS enhancement [28-30]. One of these properties is the giant fluctuations of the local fields in fractals [31]. Because the SERS enhancement is quadratic in the local field intensity enhancement, it is increased by the giant fluctuations. The spectrum of the surface plasmon resonances in fractals does allow one to explain the broad spectrum of the SERS enhancement and its increase toward the red spectral region [29]. The other reason for the SERS efficiency of fractals is their self-similarity, which is the defining property of fractals. The self-similarity leads to the transfer of the excitation down the scale of sizes enhancing its intensity [30].

In summary, EM theory of SERS, despite its simple physical concept, can account for all major SERS observations. There is first need for a nanostructured material such as fractal-like clusters, the second is the observation that some metals form good SERS active systems, the third is the observation that strongly interacting metal nanoparticles more effective SERS active systems than isolated single nanoparticles, and the last one is the observed polarization sensitivity shown by nanoparticle aggregates. However, the EM model does not account for all that is learned through SERS because there is existed the molecular resonances, charge transfer transitions and other processes in SERS phenomenon.

1–5. SERS from Transition Metal

The major obstacle hampering the generality of SERS is that only the coinage metals such as Ag, Au, Cu, and some alkali metals can provide the large enhancement because they belong to free electron metals whose surface plasmon resonance (SPR) can be efficiently excited by visible light, and only Ag, Au, and Cu can be used for practical SERS application [3-8]. This fact severely limited the SERS application in other materials. Therefore, it may be necessary for the development of extending SERS study to transition metals. Whereas transition metals have a much wider application in modern industries and technologies, such as electrochemistry, corrosion, and catalysis, they had been commonly considered as non-SERS active substrates in vibrational spectroscopy and surface science [32]. General strategy reported by Tian and coworkers that direct roughing method for intrinsic transition metal itself by electrochemically potential-controlled oxidation

and reduction cycles (ORCs) and current-controlled ORCs [37,38]. The molecular level investigation of diverse adsorbates at various transition metal electrodes can be realized by Raman spectroscopy. The important adsorbates or SERS probes can also be studied as CO, SCN⁻, CN⁻, pyridine, pyrazine and so on [37,38]. It has been demonstrated that SERS can be widely used to study electrochemical interfaces including many transition metal based systems, such as electrochemical adsorption and reaction, electrocatalysis, corrosion and fuel cells [32,36-38].

In EM theory, EM field of the light at the surface can be greatly enhances under corrective electron resonance for free electron metals [3,8]. But, the transition metals cannot be well described by the electron model. For the transition metals in periodic table of the elements, the *3d*, *4d*, and *5d* shells are always strongly mixed with the *4s*, *5s*, and *6s* states [39]. From the physical point of view, the Fermi level of transition metals locates at the *d* band. Therefore, the interband transition occurs very possibly in the visible light region [40,41]. The coupling between the high density of states and interband electronic transitions depresses the quality of the SPR of transition metals [8]. Therefore, to meet the conditions of good SPR, the metal usually needs a small value of the imaginary component of the dielectric constant [42]. However, this is impossible for the transition metals because of their large values of the imaginary part of dielectric constants in the visible light region. The dielectric constants in the Figure 4(a) are derived from the experimentally determined optical constants [43,44] through the relationships of $\epsilon_r = n^2 - k^2$, $\epsilon_i = 2nk$. Figure 4(b) illustrates dramatic differences in the SPR character between Pt and Ag elliptical nanoparticles with an aspect ratio of 2:1. The calculation is

based on a two-dimensional array model proposed by Chu and Wang [45]. It can be seen that the enhancement factor of the coinage metal increases sharply when the frequency of the excitation light is close to the frequency of the SPR.

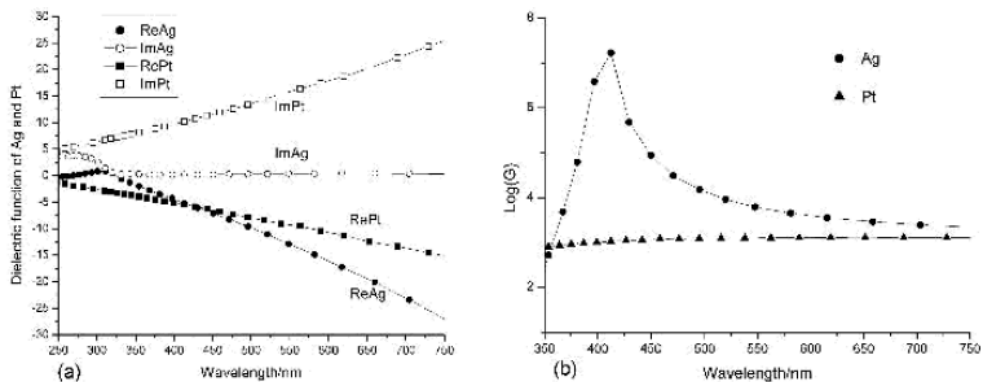


Figure 4. (a) Dielectric constants of Ag and Pt. (b) Dependence of the surface enhancement factor (G) for two-dimensional Ag and Pt nanospheroids array on the wavelength of the incident plane wave. The semiminor axis and aspect ratio of spheroids are 20 nm and 2:1, respectively. The probe molecule is assumed to be located at the tip of spheroids.

In contrast, the curves are much broader for Pt. SERS of Pt does not show any distinct character of SPR, and the enhancement factors just show a slight variation with incident photon energy. This means that the SERS intensity of Pt will not vary much with the excitation wavelength in the visible region. For example, Tian and coworkers shows experimentally that a Pt observes almost the same SERS enhancement if it changes the excitation laser from 632.8 nm (1.96 eV) to 514.5 nm (2.41 eV) while keeping all other conditions unchanged. Although the intrinsic optical property of transition metals prevents them from exhibiting intense SERS, the EM enhancement still exists in the transition metal systems with different characteristics.

1–6. Chemical Enhancement Mechanism of SERS

In all the SERS mechanism, there was considerable debate as to the exact origin of the enhancement. However, most investigators in the SERS community field agree even that there are at least two possible origins for the enhancement [46-50]. The one is EM mechanism with the surface plasmon resonances (SPR) properties which due to collective electrons oscillation in the conduction band of the metal particle. The second important contribution is a similar resonance Raman (RR) process has been observed in the SERS of some molecules that do not absorb in the visible range and it has been related to the excitation of new electronic states of the metal-adsorbate system with charge-transfer features. This is generally known as the charge-transfer (CT) chemical enhancement mechanism [46-56]. CT process can occur in either direction depending on the relative energies of the metal Fermi level and the highest occupied molecular orbital (HOMO) and lowest unoccupied molecular orbital (LUMO) levels of the adsorbed molecule. And there have been shown experimentally that the CT does take place in both directions which metal-to-molecule or molecule-to-metal depending on the nature of the molecule [46]. Molecules with low-lying unfilled orbitals experienced metal-to-molecule transfer, while those without low-lying unfilled orbitals tended to transfer electrons to the metal. The CT mechanism was first observed electrochemically as a likely discovery of SERS itself, in which resonance Raman (RR) – like process could be obtained by varying the applied potential [46-48]. The observed wavelength dependence of these resonances also showed that CT between the

molecule and the metal conduction band was responsible for this effect. CT effect is also very often acting in the SERS of molecular systems with a π -system such as benzene-like derivatives as well as the involvement of a photoinduced electronic excitation up to these resonant CT states cannot be ruled out in the SERS of aromatic molecules [51-55]. However, the recognition of these processes is a difficult task since there is very little information about the CT states [56]. Each of these resonances have a somewhat different effect on the appearance of the resulting Raman spectrum, and it is found necessary to invoke one or more of these resonances in order to completely describe a particular experiment. However, it is impossible to completely describe all the observations of the SERS phenomenon by ignoring one of these contributions [56]. Especially, a CT mechanism due to resonance of incident light with an excitation from the metal to the adsorbate, a molecular resonance mechanism where the incident light is resonant with molecular excitation, and enhancement due to non-resonant interactions between the surface and the adsorbate. It is impossible to realize that the two mechanisms are not independent of each other, but rather one or more of the two mechanisms will work in concert to give the total enhancement depending on the wavelength used in the experiment and the specific adsorbate and metal. Even though it may not always be possible to separate these different mechanisms experimentally or theoretically, certain limits can be established where one mechanism is dominating. This is evident from the work by Lombardi and Birke who theoretically presented a general expression for a metal-molecule system describing SERS based on a Herzberg-Teller vibronic coupling mechanism into the expression for the

polarizability following Tang and Albrecht [46]. There are carried out to second order in perturbation theory by allowing for breakdowns in the Born-Oppenheimer approximation. In RR scattering, assume that the three different enhancement mechanisms are involved. According to Albrecht [47], Raman tensor elements can be represented by three terms under resonance Raman conditions as follows:

$$\alpha_{\sigma\rho} = A + B + C$$

where A is sum of terms with only Frank-Condon integrals in the numerators. Far from a resonance, it vanishes, while near a resonance, one of the terms in the expression for A can become large. However, only totally symmetric Raman lines are allowed by this term. It is usually considered to be responsible for resonance Raman spectra. The sums B and C represent Herzberg-Teller contributions and stem from molecule-to-metal or metal-to-molecule CT transitions, respectively. These transitions are so called “Borrow intensity” from nearby allowed molecular transitions via the Herzberg-Teller coupling constant (h). These sums display allowed transitions both to totally symmetric and to non-totally symmetric vibrational modes and the resulting intensity can be enhanced by SPR or CT processes. Whenever SERS spectra display intensity in non-totally symmetric normal modes, the B or C sums or both must be involved, as well as its may also contribute to the totally symmetric bands, as do the A expressions.

At the beginning, considering the expression derived by Tang and Albrecht, especially C term ignored because it is observed that in most molecular systems the energy gap between the ground state and all the other states is much larger than the gaps between excited states, or that $|\omega_{IM}| \gg |\omega_{KM}|$. However, Lombardi and

Birke are assumed that states $|I_e, 0\rangle$ and $|K_e, 0\rangle$ are ground and excited zero order Born-Oppenheimer states of the molecule, while the states $|M\rangle$ are chosen to be the metal states as represent the conduction band [46]. They also assume that states $|M\rangle$ may lie between $|I\rangle$ and $|K\rangle$ and therefore C term cannot be discarded as illustrated in Figure 5(a). On this basis, they apply the Herzberg-Teller conditions a molecule-metal system without the approximation that the lowest energy gap is large, thereby maintaining the C term.

$$A_f = \left(\frac{2}{\hbar}\right) \sum_M M_{MI}^\sigma \langle i|k\rangle \langle k|f\rangle \frac{\omega_{MI} + \omega_f}{(\omega_{MI} + \omega_f)^2 + \omega^2}$$

while for $|I\rangle = |M\rangle$

$$A_k = \left(\frac{2}{\hbar}\right) \sum_M M_{KM}^\sigma M_{KM}^\rho \langle i|k\rangle \langle k|f\rangle \frac{\omega_{KM} + \omega_k}{(\omega_{KM} + \omega_k)^2 + \omega^2}$$

$$B = -\left(\frac{2}{\hbar}\right) \sum_{K \neq I} \sum_{M < K} M_{KI}^\sigma M_{MI}^\rho + M_{KI}^\rho M_{MI}^\sigma \frac{(\omega_{KI}\omega_{MI} + \omega^2)h_{KM}\langle i|q|f\rangle}{(\omega_{KI}^2 - \omega^2)(\omega_{MI}^2 - \omega^2)}$$

$$C = -\left(\frac{2}{\hbar}\right) \sum_{K \neq I} \sum_{M > I} M_{MK}^\sigma M_{KI}^\rho + M_{MK}^\rho M_{KI}^\sigma \frac{(\omega_{KI}\omega_{KM} + \omega^2)h_{IM}\langle i|q|f\rangle}{(\omega_{KI}^2 - \omega^2)(\omega_{MI}^2 - \omega^2)}$$

where ω_k and ω_f are the frequencies of particular excited or ground state vibration, respectively. Term A_f represents resonant molecule-to-metal CT from ground state to one of the unfilled metal levels M, while A_k represents resonant metal-to-molecule charge transfer from a filled metal state M to an excited state K. The sum over vibrational state k has been removed. Term B represents molecule-to-metal charge transfer from the molecular ground state to one of the unfilled metal levels M. This transition obtain its intensity *via* M_{MI} through intensity borrowing from the allowed transition $I \rightarrow K$. This is illustrated in Figure 5(b). The

borrowing mechanism is vibronic coupling through h_{KM} which represents coupling of the metal to excited molecular states through some vibrational mode. The requirement that this term be nonvanishing imposes some symmetry restrictions on the vibrations which may be responsible for the mixing. Note that the enhancement come through the resonance denominator $\omega_{KI}^2 - \omega^2$.

Term C represents metal-to-molecule charge transfer from one of the filled metal levels M to the excited states K. This transition obtains its intensity *via* M_{MK} through intensity borrowing from the allowed $I \rightarrow K$ transition. h_{KM} represents vibronic coupling of the metal to the ground molecular level through some vibrational mode. This illustrated in Figure 5(c). Note that the enhancement come through the resonance denominator $\omega_{KM}^2 - \omega^2$.

B and C terms indicate that in order for B or C to be nonvanishing $\langle i|q|f \rangle$ must be nonzero. This leads to the usual selection rule that $f = i \pm 1$ in the harmonic oscillator approximation. It is further required for B that neither h_{KM} nor appropriate components of M_{KI} and M_{MI} vanish. For C term, its require neither h_{IM} nor components of M_{MK} and M_{KI} vanish. For B term assuming a totally symmetric ground state, these observations imply that the symmetry species Γ_M and Γ_K of these electronic states must each correspond to Γ_ρ , the species of at least one translation. At the same time the direct product $\Gamma_K \times \Gamma_Q \times \Gamma_M$ must contain the totally symmetric representation to prevent h_{KM} from vanishing.

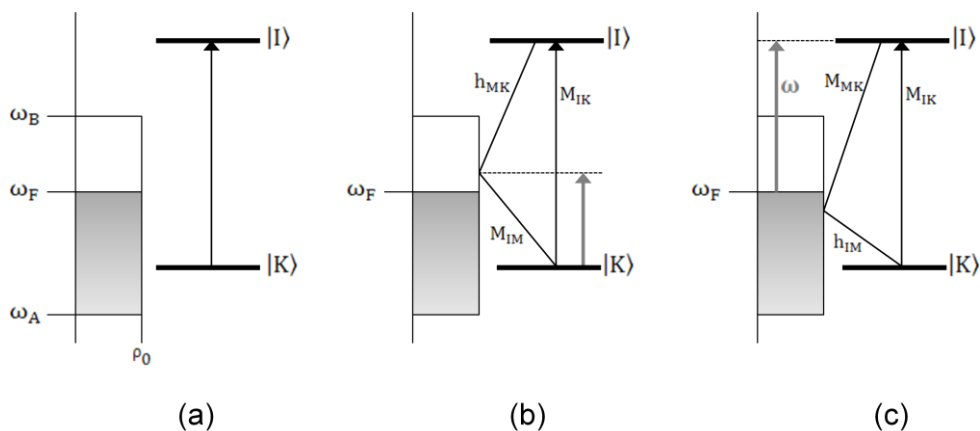


Figure 5. (a) Energy level scheme for molecule-metal system. The discrete molecular levels are I and K, between which a transition is assumed to be allowed. The continuous metal levels of the conduction band of the metal are shown on the left. The conduction band ranges between ω_A and ω_B and is assumed to have a constant density of states ρ_0 . The filled levels range up to ω_F , the Fermi level, and are depicted by lines, while the unfilled levels are depicted by dots. (b) The scheme for molecule-to-metal CT transitions between the ground molecular state and unfilled levels of the metal. Transition borrows intensity from the allowed transition by means of vibronic coupling between metals and the excited molecular level through the matrix element h_{MK} . (c) The scheme for metal-to-molecule CT transitions between filled level of the metal and the excited molecular state. The transition borrows intensity from the allowed transition by means of vibronic coupling between metal levels and the ground molecular state through the matrix element h_{IM} .

By Γ_Q means the irreducible representation for which $\left(\frac{\partial H'}{\partial Q}\right)$ is a basis which is the same as that for Q. Thus if $\Gamma_K = \Gamma_\rho$ and $\Gamma_M = \Gamma_{\rho'}$ it is required that Γ_Q must correspond to at least one of the species contained in $\Gamma_\rho \times \Gamma_{\rho'}$ which are the normal selection rules for the Raman effect. A similar analysis for C term lead to the identical conclusion. However, here is recognized that the symmetry species considered above belongs to the point group corresponding to the molecule-metal system, which will most likely be of lower symmetry than that of the molecule

alone. In fact unless the surface is considered perfectly smooth and some symmetry axis of the molecule is exactly perpendicular to the surface plane, or that the active site in which the molecule sits is relatively symmetric, it is more than likely that no symmetry elements will exist. Thus all irreducible representations above will trivially be totally symmetric, implying all vibrations allowed, and furthermore no particular variation in the depolarization ratios among the various normal modes.

As mentioned above, the CT resonance chemical enhancement mechanism have been well described theoretically, however, the experimental understanding of CT contribution to enhancement is still limited due to the lack of appropriate system. As the explosive development of analysis and detecting techniques based on SERS, the further understanding and exploiting the CT contribution becomes particularly important.

References

1. Long, D. A. *The Raman Effect*. John Wiley & Sons, New York, **2002**.
2. Weber, A. *Raman Spectroscopy of Gases and Liquids*. Topics in Current Physics. John Springer-Verlag, Berlin, **1979**.
3. Chang, R. K.; Furtak, T. E. *Surface Enhanced Raman Scattering*, Plenum Press: New York, **1982**.
4. Kniepp, K.; Moskovits, M.; Kniepp, H. *Topic Appl. Phys.* **2006**, *103*, 1.
5. Fleishman, M.; Hendra, P. J.; McQuillan, A. J. *Chem. Phys. Lett.* **1974**, *26*, 123.
6. Jeanmaire, D. L.; Van Duyne, R. P. *J. Electroanal. Chem.* **1977**, *84*, 1.
7. Albrecht, M. G.; Creighton, J. A. *J. Am. Chem. Soc.* **1977**, *99*, 5215.

8. Moskovits, M. *Rev. Mod. Phys.* **1985**, *57*, 783.
9. Nie, S.; Emory, S. R. *Science* **1997**, *275*, 1102.
10. Kneipp, K.; Wang, Y.; Kneipp, H.; Itzkan, I.; Dasari, R. R.; Feld, M. S. *Phys. Rev. Lett.* **1996**, *76*, 2444.
11. Kleinman, S. L.; Ringe, E.; Valley, N.; Wustholz, K. L.; Phillips, E.; Scheidt, K. A.; Schatz, G. C.; Van Duyne, R. P. *J. Am. Chem. Soc.* **2011**, *133*, 4115.
12. Le Ru, E. C.; Grand, J.; Sow, I.; Somerville, W. R. C.; Etchegoin, P. G.; Treguer-Delapierre, M.; Charron, G.; Félidj, N.; Lévi, G.; Aubard, J. *Nano. Lett.* **2011**, *11*, 5013.
13. Kneipp, K.; Kneipp, H.; Itzkan, I.; Dasari, R.; Feld, M. *Chem. Rev.* **1999**, *99*, 2957.
14. Dickson, R. M.; Lyon, L. A. *J. Phys. Chem. B* **2000**, *104*, 6095.
15. Lee, S. J.; Moskovits, M. *J. Am. Chem. Soc.* **2012**, *134*, 11384.
16. Kelly, K. L.; Coronado, E.; Zhao, L.L.; Schatz, G. C. *J. Phys. Chem. B* **2003**, *107*, 668.
17. Xu, H. H.; Käll, M. *Chem. Phys. Chem.* **2003**, *4*, 1001.
18. Xu, H. H.; Aizpurua, J.; Käll, M.; Apell, P. *Phys. Rev. B* **2000**, *62*, 4318.
19. Stockman, M. I. *Phys. Rev. E* **1997**, *56*, 6494.
20. Shalaev, V. M.; Sarychev, K. *Phys. Rev. B* **1998**, *57*, 13265.
21. Gersten, J. I. *J. Chem. Phys.* **1980**, *72*, 5779.
22. Gersten, J. I.; Nitzan, A. *J. Chem. Phys.* **1981**, *75*, 1139.
23. McCall, S. L.; Platzman, P. M.; Wolff, P. A. *Phys. Lett. A* **1980**, *77*, 381.
24. Wang, D.-S.; Kerker, M.; Chew, H. W. *Appl. Opt.* **1980**, *77*, 381.

25. Ruppin, R. *Solid State Commun.* **1981**, 39, 903.
26. Aravind, P. K.; Nitzan, A.; Metiu, H. *Surf. Sci.* **1981**, 110, 189.
27. Wang, Z. J.; Pan, S. L.; Krauss, T. D.; Du, H.; Rothberg, L. J. *Proc. Nat. Acad. Sci. USA* **2003**, 100, 8638.
28. Shalaev, V. M.; Stockman, M. I. *Sov. Phys. JETP* **1987**, 65, 287.
29. Stockman, M. I.; Shalaev, V. M.; Moskovits, M.; Botet, R.; George, T. F. *Phys. Rev. B* **1992**, 46, 2821.
30. Li, K.; Stockman, M. I.; Bergman, D. J. *Phys. Rev. Lett.* **2003**, 91, 227402.
31. Stockman, M. I.; Pandey, L. N.; Muratov, L. S.; George, T. F. *Phys. Rev. Lett.* **1994**, 72, 2486.
32. Tian, Z. Q.; Ren, B.; Wu, D. Y. *J. Phys. Chem. B* **2002**, 106, 9463.
33. Van Dyne, R. P.; Haushalter, J. P. *J. Phys. Chem.* **1983**, 87, 2999.
34. Rubim, J. C.; Kannen, G.; Schumacher, D.; Dunnwald, J.; Otto, A. *Appl. Surf. Sci.* **1989**, 37, 233.
35. Fleishmann, M.; Tian, Z. Q. *J. Electroanal. Chem.* **1987**, 217, 385.
36. Leung, L. W. H.; Weaver, M. J. *J. Am. Chem. Soc.* **1987**, 109, 5113.
37. Tian, Z. Q.; Ren, B.; Li, J.-F.; Yang, Z.-L. *Chem. Comm.* **2007**, 3514.
38. Tian, N.; Zhou, Z.-Y.; Sun, S.-G.; Cui, L.; Ren, B.; Tian, Z. Q. *Chem. Comm.* **2006**, 4090.
39. Ebert, H. *Rep. Prog. Phys.* **1996**, 59, 1665.
40. Weaver, J. H. *Phys. Rev. B* **1975**, 11, 1416.
41. Ordal, M. A.; Bell, R. J.; Alexander, R. W.; Long, L. L.; Querry, M. R. *Appl. Opt.* **1985**, 24, 4493.

42. Gersten, J.; Nitzan, A. *J. Chem. Phys.* **1980**, *73*, 3023.
43. Johnson, P. B.; Christy, R. W. *Phys. Rev. B* **1972**, *6*, 4370.
44. Palik, E. D. *Handbook of Optical Constants of Solids*, Academic, New York, **1985**.
45. Chu, L. C.; Wang, S. *Phys. Rev. B* **1985**, *31*, 693.
46. Lombardi, J. R.; Birke, R. L.; Lu, T.; Xu, J. *J. Chem. Phys.* **1986**, *84*, 4174.
47. Tang, J.; Albrecht, A. C. in *Raman Spectroscopy, Theory, and Practice*, Edited by Szymanski, H. A. Plenum, New York, **1970**, Vol. 2, p. 33.
48. Lombardi, J. R.; Birke, R. L. *J. Phys. Chem. C* **2008**, *112*, 5605.
49. Champion, A.; Kambhampati, P. *Chem. Soc. Rev.* **1998**, *27*, 241.
50. Kneipp, K.; Kneipp, H.; Itzkan, I.; Dasari, R.; Feld, M. *J. Phys.: Condens. Matter* **2002**, *14*, R597.
51. Osawa, M.; Matsuda, N.; Yoshii, K.; Uchida, I. *J. Phys. Chem.* **1994**, *98*, 12702.
52. Valley, N.; Jensen, L.; Autschbach, J.; Schatz, G. C. *J. Chem. Phys.* **2010**, *133*, 054103.
54. Chao, Y.; Zhou, Q.; Li, Y.; Yan, Y.; Wu, Y.; Zheng, J. *J. Phys. Chem. C* **2007**, *111*, 16990.
55. Jensen, L.; Aikens, C. M.; Schatz, G. C. *Chem. Soc. Rev.* **2008**, *37*, 1061.
56. Otto, A.; Mrozek, I.; Grabhorn, H.; Akemann, W. *J. Phys.: Condens. Matter* **1992**, *4*, 1143.
57. Lombardi, J. R.; Birke, R. L. *Acc. Chem. Res.* **2009**, *42*, 734.

Chapter. 2

History of 4-Aminobenzenethiol (4-ABT)

From SERS field

1. Introduction

The 4-aminobenzenethiol (4-ABT) (also known as para-aminothiophenol or para-mercaptoaniline) is unusual molecule, which has a thiol group substituted at the para position of aniline in centered benzene ring is one of the important surface probe molecules in SERS community and the nanoscience field [1,2]. The main reasons are that it can be strongly and easy adsorbed onto most SERS substrates as well as it obtained a strong and unique SERS signal. Moreover, the SERS signal is very sensitive to depending on the type of substrate and measurement conditions [3-24]. However, for the enhancement mechanism in SERS of 4-ABT on metal surfaces is still unclear and there are also have the three interpretations in the SERS community [3-24].

Since the Osawa and co-workers observed for the first time the Raman spectra of 4-ABT, first claim is that the bands are the b_2 -type bands of 4-ABT arising from the CT chemical enhancement mechanism through the Herzberg-Teller vibronic coupling term [3-5]. The second claim is that the b_2 -type bands appearing in the SERS of 4-ABT must be the N=N stretching vibrations of 4,4'-dimercaptoazobenzene (4,4'-DMAB) produced from 4-ABT via a catalytic coupling reaction on the metal substrates [7-11]. According to first claim by Osawa and coworkers, they found that the main vibrational bands in the SERS spectra of 4-ABT adsorbed on Ag electrode based on the measurement an applied potential, wavelength-dependent SERS, surface-enhanced infrared absorption (SEIRA) spectroscopy, cyclic voltammetry and UV resonance Raman (UVRR) of 4-ABT

itself [3]. They reported that the 4-ABT assigned to the vibrational modes with a_1 symmetry, which in the normal Raman (NR) spectrum, only peaks assignable to totally symmetric (a_1) vibrations are observed, including the bands at ~ 1190 and $\sim 1177 \text{ cm}^{-1}$. Another is assigned to the vibrational modes with b_2 symmetry, which in the SERS spectrum, non- a_1 -type (or b_2) peaks are also usually identified, including the bands at ~ 1573 , ~ 1440 , ~ 1391 , and $\sim 1142 \text{ cm}^{-1}$. They already tried to interpret the SERS spectrum of 4-ABT from the EM mechanism proposed by Creighton and by Moskovits and Suh [25,26]. According to the surface selection rules from the enhancement factors of the EM mechanism, a 4-ABT adsorbed on Ag surface with a C_{2v} symmetry point group should obey the relationship of $b_2 \approx b_1 > a_2$ when its C_{2v} axis is perpendicular to the metal surface and if the molecule were lying flat, the enhancement order should be $a_2 \approx b_1 > b_2$. However, for 4-ABT molecule adsorbed on noble metal surfaces, Raman bands that were assigned to the b_2 modes were found to be significantly enhanced, even stronger than that of the a_1 modes. In the end, all b_2 modes could not be explained by the EM mechanism for any other considerable orientations [3]. In electrochemical environments, the intensity of the a_1 modes is insensitive to the variation of the applied potential because this mode is also believed to be enhanced only by the EM mechanism, experimentally. Meanwhile, the intensity of the b_2 modes is very sensitive to the change of the applied potential, whose intensity increases and then decreases in potential range of 0.2 V to -1.0 V vs. SCE. That is, b_2 mode bands not only show resonance shaped intensity profiles as a function of applied potential, but also the intensity-potential profiles shift to positive potentials

as the excitation energy increases by using 488, 514.5, and 632.8 nm excitation sources. More interestingly, the b_2 modes were also observed in the UVRR of 4-ABT excited by a laser with a wavelength of 299.1 and 309.1 nm lines, located in the L_b band of the UV absorption spectrum of the 4-ABT molecule itself. Therefore, they believed that electron transfer from Ag metal-to-(4-ABT) via C term from Herzberg-Teller contribution (as proposed by Lombardi and Birke) is the main reason for the appearance of the b_2 modes through carefully designed experiments and the good correlation between the laser excitation energy and the electrode potential profiles.

In addition, they are also suggested that the difference in enhancement pattern for the reason why the b_2 type bands are not very strong in the UVRR scattering as in the SERS. Considering the excitations used in the present UVRR study are far from the allowed $B_{a,b}$ transition, they assumed the contribution of the A term is small. And for weakly allowed transition, Raman scattering may be enhanced from B term. B term is large because of the weakly allowed resonance state occurred to the vibronic coupling to a nearby strongly allowed state. Therefore, totally and nontotally symmetric modes can be enhanced via B term. For substituted benzenes model the L_a transition is also coupled to the a component of the $B_{a,b}$ transition via the normal coordinate ν_{8a} and, to a lesser extent, via ν_{9a} . The ν_{8b} mode can also couple the L_a transition with the b component of the $B_{a,b}$ transition. On the other hand, the L_b transition is couple to the $B_{a,b}$ transition via ν_{8a} , ν_{8b} , ν_{19a} , and ν_{9a} modes. Accordingly, these vibrational modes are greatly enhanced by the

intensity borrowing from the $B_{a,b}$ transition. In the B term contribution, they make a same conclusion for a SERS pattern of 4-ABT on Ag system. As described in chapter I-6, the A term represents the Franck-Condon contribution, and only totally symmetric modes are enhanced by this mechanism, as a case of resonance Raman scattering. On the other hand, B and C terms arise from the Herzberg-Teller contribution and represent the enhancement from molecule-to-metal CT and metal-to-molecule CT, respectively. Totally and nontotally symmetric modes are enhanced by B and C terms. 4-ABT on Ag in CT directions is metal-to-molecule, the nontotally b_2 symmetric modes are be enhanced from the C term. The vibronic coupling in the SERS is between metal Fermi level and the ground state of the molecule. Therefore, the difference enhancement patterns in the 4-ABT SERS and UVRR are attributed to the difference in electronic states vibronically coupled. Consulting the Term C from chapter I-6, they are account for b_2 type bands that the molecular z -axis is oriented normal to the metal surface for 4-ABT on Ag, $\Gamma_M = a_1$ and $\Gamma_K = b_2$ if the K state is LUMO. Therefore, only b_2 modes can be enhanced from the C term. If second and third LUMOs were the K state, a_1 and both a_1 and b_2 modes should be enhanced, respectively. Therefore, the affinity level is identified as LUMO. On the other hand, the other claim by Tian and Sun is that the b_2 -type bands appearing in the SERS of 4-ABT must be the N=N stretching vibrations of 4,4'-dimercaptoazobenzene (4,4'-DMAB) produced from 4-ABT via a catalytic coupling reaction on the metal substrates [7-11]. They are also asserted that experimentally and theoretically 4-ABT was to be oxidized to form 4,4'-

DMAB on a electrochemically roughened Ag electrode during the SERS measurement. Experimentally, this assumption based on the SERS and surface mass spectroscopic (SMS) measurement. And it is also theoretically predicted that 4,4'-DMAB can be produced from 4-ABT by electrochemically switching cycle of a single 4,4'-DMAB between two Ag nanosurfaces.

If this is correct, there are need to re-examine the SERS characteristics of 4-ABT with 4,4'-DMAB and its analog molecules more carefully to understand why so many researchers made the wrong assignment for the past two decades in view of the vibrational spectroscopy and surface analysis. Therefore, to clarify the origin of the b_2 -type bands for SERS of the 4-ABT, section 1~6 in this chapter will demonstrate a lot of the experimental results that 4-ABT and its analogs include 4,4'-DMAB adsorbed on various substrate such as Ag, Au and Pt under various measurement conditions such as vapor organic chemicals (VOCs), solution pH, NaBH_4 , electrochemical potential and laser wavelength. After considering all the factors, these observations consequentially will support also present proposition that the b_2 -type bands appearing in the SERS of 4-ABT must be attributable to the chemical enhancement of 4-ABT itself.

2. United Experimental Section.

2-1. Chemicals and Materials

Ag wire (99.99%), Pt wire (99.99%), silver nitrate (AgNO_3 , 99.99%), hydrogen chloroaurate (HAuCl_4 , 99.99%), Chloroplatinic acid hexahydrate ($\text{H}_2\text{PtCl}_6 \cdot 6\text{H}_2\text{O}$), sodium citrate (99.9%), sodium borohydride (NaBH_4 , 99.9%), L-ascorbic acid, 3-aminopropyltrimethoxysilane (3-APS, 99%), disodium hydrogen phosphate (Na_2HPO_4 , $\geq 99.0\%$) and toluene (99.8%) were purchased from Aldrich and used as received. Methyl alcohol (99.5%), hydrochloric acid (HCl , 37%) and sodium perchlorate monohydrate ($\text{NaClO}_4 \cdot \text{H}_2\text{O}$, 98%) were purchased from Samchun chemicals). Potassium hydroxide ($>85\%$, Daejung chemicals), and absolute ethanol (99.0%) was purchased from J. T. Baker. 4-aminobenzenethiol (4-ABT, 97%) and benzenethiol (BT, 97%) were purchased from Aldrich and used as received.

4,4'-DMAB (MW = 246.4) and 4,4'-DMHAB (MW = 248.37) were custom synthesized by Medigen Co. Specifically, 4,4'-DMAB was delivered as a light-yellow-colored solid; the parent mass peak (m/z) corresponding to the protonated form of the compound was identified at 247.3 ($[\text{M}+\text{H}]^+$), and three different protons were identified in the proton NMR spectrum, namely, at 3.6 ppm for SH, at 7.4 ppm for 2-CH, and at 7.8 ppm for 3-CH. On the other hand, 4,4'-DMHAB was delivered as a light-beige-colored solid; the parent mass peak corresponding to the molecular weight of the compound was identified at 249.3, and four different

protons were identified in the proton NMR spectrum, namely, at 3.6 ppm for SH, at 4.5 ppm for NH, at 6.6 ppm for 2-CH, and at 7.1 ppm for 3-CH.

Other chemicals, unless specified, were reagent grade, and triply distilled water of resistivity greater than 18.0 M Ω -cm was used throughout. Different pH solutions ranging from pH 2 to 10 were prepared by mixing aqueous solutions of 0.1 M HCl (or 0.1 M NaOH) and 0.1 M disodium hydrogen phosphate.

2-2. Preparation Methods of Silver, Gold and Size-controlled Pt sols and Their SERS-active films

Ag and Au sols were prepared by following the modified recipe by Grabar et al. from the recipes of Lee and Meisel [27,28]. For the Au sol, 500 mL of 0.01% aqueous solution of H₂AuCl₄ was brought to the boil, 7 mL of 1% sodium citrate was added therein under vigorous stirring, and boiling was continued for 30 min. For the Ag sol, a solution of 45 mg AgNO₃ in 250 mL of deionized water was brought to boil with vigorous stirring. To this solution was added 15 mL of 1% sodium citrate, and boiling was continued for 30 min.

Pt sols were prepared by following the seed-mediated growth method reported by Bigall et al [29]. Initially, small platinum seeds of 5–7 nm diameter were prepared. At first, 3 mL of a 0.2% solution of chloroplatinic acid hexahydrate was added to 39 mL of boiling deionized water. After 1 min, 0.92 mL of 1% sodium citrate was added, followed half a minute later by a quick injection of 0.46 mL of a freshly prepared 0.08% solution of sodium borohydride also containing 1% sodium citrate. After 10 min, the sol solution was cooled down to room temperature. The seeds

obtained in this way were used in preparing ~30 nm sized Pt particles. Specifically, to 30 mL of deionized water was added consecutively 1 mL of the platinum seed solution, 0.045 mL of 0.4 M chloroplatinic acid solution, and then 0.5 mL of 1.25% L-ascorbic acid solution containing also 1% sodium citrate. The mixture was slowly heated to the boiling point and left to boil for 30 min with stirring. According to the transmission electron microscopy (TEM) analysis, the size of the Pt nanoparticles was 28 nm. These 28 nm-sized Pt particles were used as seeds in preparing ~46 nm-sized Pt particles. The reaction mixture for 46 nm-sized Pt particles was comprised of 26 mL of deionized water, 1 mL of 28 nm-sized Pt solution, 0.045 mL of chloroplatinic acid, and a 0.5 mL mixture solution of 1% sodium citrate and 1.25% L-ascorbic acid. To prepare 72 (or 105) nm-sized Pt particles, the reaction mixture was comprised of 29 mL of deionized water, 1 (or 0.25) mL of 46 (or 72) nm-sized Pt solution, 0.045 mL of chloroplatinic acid, and a 0.5 mL mixture solution of 1% sodium citrate and 1.25% L-ascorbic acid. As before, the reaction mixture was boiled for 30 min with stirring, and then cooled down to room temperature. The reaction products gathered by centrifugation (Centrifuge operated at 1000~13500 rpm depending on the nanoparticle size) were washed three times with deionized water, and then stored by dispersing in water.

Ag, Au, and Pt nanoaggregate films were prepared by dropping the respective Ag, Au, and Pt sol solution onto an ITO/Glass or Si wafer. Initially, the ITO/Glass and Si wafers were subjected to ozonolysis to render them hydrophilic at a water contact angle $<5^\circ$. They were subsequently reacted with 3-APS, following the protocol given in the literature, in order to possess amine-terminated functionalities

[28]. A Viton O-ring of i.d. 5 mm was subsequently placed on the ITO/Glass or Si wafer, and then multiples of 10 μL of Ag or Au or Pt sol were injected inside the O-ring. The injected substrate was left to dry under ambient conditions to form a uniform and circular nanoaggregate film. The film was washed with deionized water and then dried under an N_2 atmosphere. Ag, Au, and six different sized Pt nanoaggregate films were prepared by injecting 10, 20, 30, 40, 50 and 60 μL of Pt sol onto an ITO/Glass or Si wafer, and their dried films were named S1, S2, S3, S4, S5 and S6, respectively. Especially, these Pt films case were cleaned in an electrochemical cell *via* a hydrogen evolution reaction in 0.1 M, H_2SO_4 aqueous solution, lastly washed with water and air dried. When adsorbing organic probe molecules onto Ag, Au, and Pt, all the nanoaggregate films were soaked in 1~5 mM ethanolic solution of various probe molecules for 1~3 h and then washed with ethanol again.

To fabricate Au and Ag nanoparticle-adsorbed glass capillaries, the inside surface of glass capillaries was first reacted with 3-APS to make it possess amine-terminated functionalities, and then Au or Ag sol solution was injected, using a syringe, into the capillaries and left in that state for 12 h; the unbound Au or Ag colloids were sucked out later using a syringe. Subsequently, 4-ABT or 4,4'-DMAB was adsorbed onto the Au or Ag nanoparticles by injecting their ethanolic solution (2 mM); after 2 h, the capillary was washed with ethanol and air dried.

2–3. Preparation of Silver Thiolate Salts

Silver salts of 4-ABT and 4,4'-DMAB were prepared using a one or two-phase method. First, a 3 mL aqueous solution of 0.1 M AgNO₃ was added dropwise to a 7 mL toluene solution of 0.1 M 4-ABT or 4,4'-DMAB with vigorous stirring in a flask that was wrapped in Al foil to minimize the effect of ambient light. After 3 h of vigorous stirring, the bright yellow Ag-4ABT or red Ag-4,4'DMAB precipitates were removed via filtration, consecutively washed with ethanol, toluene, and cold water, and then dried in vacuo. Elemental analyses corresponded to 1:1 compounds with Ag(I) ions for both 4-ABT and 4,4'-DMAB. For Ag-4ABT, weight percent values of C 33.46, H 3.12, N 6.32, S 14.61 and Ag 42.49 were found, which correspond well with the calculated weight percent values for a 1:1 adduct of C 32.06, H 2.61, N 6.04, S 13.82, and Ag 45.47. For Ag-4,4'DMAB, weight percent values of C 42.32, H 2.43, N 8.11, S 19.67, and Ag 27.47 were found, and the calculated weight percent values for a 1:1 adduct were C 40.92, H 2.29, N 7.95, S 18.21, and Ag 30.63.

2–4. EDC Coupling and Crystal Growth Methods

To fabricate SERS-active glass capillaries, the inside surfaces of the glass capillaries were first reacted with 3-APS, and then the Ag sol was injected into the capillaries using a syringe. The capillaries were left in that state for 12 h, then the unbound Ag colloids were sucked out using a syringe. Subsequently, ethanolic solutions of 4-ABT or 4,4'-DMAB (2 mM) were injected into the capillaries. After

5 h, the capillaries were washed with ethanol and air dried. These capillaries were subjected to Raman spectral analyses in the presence of an EDC coupling reagent composed of 0.02 M 4-CBA and 0.02 M EDC in DMF [30]. This work also prepared the SERS-active silver substrate by immersing an Ag foil in dilute (1:1) HNO₃ to demonstrate the growth of a crystal. The crystallization of calcium carbonate was conducted by soaking the laser-irradiated sample in a 10 mM NaHCO₃ aqueous solution (10 mL) for 10 h, followed by addition of a 10 mM CaCl₂ solution (10 mL).

2–5. Instruments

UV-visible (UV-vis) spectra were obtained with a SCINCO S-4100 spectrometer. The transmission electron microscopy (TEM) images of Ag nanoparticles were obtained with a JEM-200CX transmission electron microscope at 200 kV. The field-emission scanning electron microscopy (FE-SEM) images were obtained with a JSM-6330F field emission electron microscope operating at 5 kV. X-ray diffraction (XRD) patterns were obtained on a MAC Science M18XHF-SRA diffractometer over a 2θ range of 3° to 60° at an angular resolution of 0.02° using Cu K α (1.5419 Å) radiation. Elemental analyses (EA) were performed using a Thermo Electron Model Flash EA 1112 analyzer. Thermogravimetric analysis (TGA) and differential scanning calorimetry (DSC) data were performed using a TA Instrument 2050 thermogravimetric analyzer in a nitrogen atmosphere at a heating rate of 10 °C/min.

Raman spectra were obtained using a Renishaw Raman system Model 2000 spectrometer equipped with an integral microscope (Olympus BH2-UMA). The 514.5 nm line from a 20 mW Ar⁺ laser (Melles-Griot Model 351MA520) or the 488 and 568 nm lines from a 20 mW Ar⁺/Kr⁺ laser (Melles-Griot Model35KAP431) or the 632.8 nm line from a 17 mW He/Ne laser (Spectra Physics Model 127) were used as the excitation source. Raman scattering was detected over a 180° range with a Peltier cooled (-70°C) charged-coupled device (CCD) camera (400 × 600 pixels). The laser beam was focused onto a spot approximately 1 μm in diameter and the laser power at the sampling position was 2.1 and 1.1 mW for 514.5- and 632.8-nm line, respectively. The Raman band of a silicon wafer at 520 cm⁻¹ was used to calibrate the spectrometer, and the accuracy of the spectral measurement was estimated to be better than 1 cm⁻¹.

The potential of the electrochemical cell was controlled using a CH Instruments model 660A potentiostat, which employed CHI 660A electrochemical analyzer software (version 2.03) running on an IBM-compatible PC. All potentials are reported with respect to the saturated Ag/AgCl or saturated calomel electrode (SCE). Separately, an electrochemical potential measurement was made using a silver wire electrode after dipping it in variously diluted aqueous NaBH₄ solutions.

References

1. Zhou, Q.; Li, X.; Fan, Q.; Zhang, X.; Zheng, J. *Angew. Chem., Int. Ed.* **2006**, *45*, 3970.
2. Ward, D. R.; Halas, N. J.; Ciszek, J. K.; Tour, J. M.; Wu, Y.; Nordlander, P.; Natelson, D. *Nano Lett.* **2008**, *8*, 919.
3. Osawa, M.; Matsuda, N.; Yoshii, K.; Uchida, I. *J. Phys. Chem.* **1994**, *98*, 12702.
4. Lombardi, J. R.; Birke, R. L. *Acc. Chem. Res.* **2009**, *42*, 734.
5. Lombardi, J. R.; Birke, R. L.; Lu, T.; Xu, J. *J. Chem. Phys.* **1986**, *84*, 4174.
6. Hill, W.; Wehling, B. *J. Phys. Chem.* **1993**, *97*, 9451.
7. Huang, Y. F.; Zhu, H. P.; Liu, G. K.; Wu, D. Y.; Ren, B.; Tian, Z. Q. *J. Am. Chem. Soc.* **2010**, *132*, 9244.
8. Fang, Y.; Li, Y.; Xu, H.; Sun, M. *Langmuir* **2010**, *26*, 7737.
9. Sun, M.; Xu, H. *Small* **2012**, *8*, 2777.
10. Wu, D.-Y.; Liu, X.-M.; Huang, Y.-F.; Ren, B.; Xu, X.; Tian, Z. Q. *J. Phys. Chem. C* **2009**, *113*, 18212.
11. Sun, M.; Huang, Y.; Xia, L.; Chen, X.; Xu, H. *J. Phys. Chem. C* **2011**, *115*, 9629.
12. Zong, S.; Wang, Z.; Yang, J.; Cui, Y. *Anal. Chem.* **2011**, *83*, 4178.
13. Zhou, Q.; Li, X.; Fan, Q.; Zhang, X.; Zheng, J. *Angew. Chem. Int. Ed.* **2006**, *45*, 3970.
14. Uetsuki, K.; Verma, P.; Yano, T.-A.; Saito, Y.; Ichimura, T.; Kawata, S. *J. Phys. Chem. C* **2010**, *114*, 7515.
15. Park, W.-H.; Kim, Z. H. *Nano Lett.* **2010**, *10*, 4040.

16. Kim, N. J. *J. Phys. Chem. C* **2010**, *114*, 13979.
17. Ikeda, K.; Suzuki, S.; Uosaki, K. *Nano Lett.* **2011**, *11*, 1716.
18. Wang, X.; Shi, W.; She, G.; Mu, L. *J. Am. Chem. Soc.* **2011**, *133*, 16518.
19. Kim, K.; Shin, D.; Lee, H. B.; Shin, K. S. *Chem. Commun.* **2011**, *47*, 2020.
20. Ye, J.; Hutchison, J. A.; Uji-i, H.; Hofkens, J.; Lagae, L.; Maes, G.; Borghsa, G.; Van Dorpea, P. *Nanoscale* **2012**, *4*, 1606.
21. Kim, K.; Kim, K. L.; Shin, D.; Choi, J.-Y.; Shin, K. S. *J. Phys. Chem. C* **2012**, *116*, 4774.
22. Kim, K.; Shin, D.; Choi, J.-Y.; Kim, K. L.; Shin, K. S. *J. Phys. Chem. C* **2011**, *115*, 24960.
23. Kim, K.; Shin, D.; Kim, K. L.; Shin, K. S. *Phys. Chem. Chem. Phys.* **2012**, *14*, 4095.
24. Kim, K.; Kim, K. L.; Lee, H. B.; Shin, K. S. *J. Phys. Chem. C* **2012**, *116*, 11635.
25. Creighton, J. A. *Surf. Sci.* **1977**, *62*, 31.
26. Moskovits, M.; Suh, J. S. *J. Phys. Chem.* **1984**, *88*, 5526.
27. Lee, P. C.; Meisel, D. *J. Phys. Chem.* **1982**, *86*, 3319.
28. Grabar, K. C.; Freeman, R. G.; Hommer, M. B.; Natan, M. J. *Anal. Chem.* **1995**, *67*, 735-743.
29. Bigall, N. C.; Härtling, T.; Klose, M.; Simon, P.; Eng, L. M.; Eychemüller, A. *Nano Lett.* **2008**, *8*, 4588.
30. Han, S. W.; Lee, I.; Kim, K. *Langmuir* **2002**, *18*, 182.

Chapter 3

The SERS of 4-ABT on Pt And Volatile
Organic Chemicals (VOCs) Effects of 4-ABT
on Ag

3-1. Surface-Enhanced Raman Scattering on Aggregates of Pt Nanoparticles with Definite Size

Introduction

Firstly, one of the clarifications the origin of the b_2 -type bands for SERS of the 4-ABT, this study demonstrated that 4-ABT adsorbed on transition metal such as platinum (Pt) by SERS, compared to the previous reports such as 4-ABT onto Ag system [1-3]. Tian and coworkers reported that transition metals themselves could be made to be SERS-active, via an electrochemical roughening process, with the EFs ranging from 1 to 3 orders of magnitude [4-9]. The other way as an attenuated total reflection (ATR) method to excite the surface plasmon polariton (SPP) was applied to transition metals, like Pt, as well as noble metals to improve the sensitivity level of classical Raman spectroscopy [10,11]. However, it is still difficult to obtain Raman spectra of molecules adsorbed on transition metals like Pt, especially in non-electrochemical environments or without a sophisticated ATR-SPP setup.

For SERS to occur via the EM enhancement mechanism, the Raman excitation wavelength has to be close to that of the surface plasmon oscillation of metal nanoparticles or nanoaggregates. Earlier, Creighton and Eadon calculated the optical absorption of Pt nanoparticles based on the Mie theory and showed that a

plasmon peak should appear at 215 nm [12]. Experimentally, Henglein et al. showed that a peak really exists around 215 nm for nanoparticles prepared by the radiolytic reduction of PtCl_4^{2-} [13,14]. So far, the Pt particles prepared by the chemical reduction of PtCl_4^{2-} are mostly smaller than ~10 nm, showing negligible absorption in the visible region. This suggests that SERS spectra are hard to obtain for molecules assembled on Pt nanoparticles, at least under visible light excitation and in a non-electrochemical environment. However, it is also possible to record SERS spectra from the previous reports, even with visible excitation, for organic monolayers assembled on Pt nanoparticles, specifically those with diameters of ~17 nm, prepared by a laser-ablation method [15-17]. In that work, the EF estimated using benzenethiol (BT) as a model adsorbate was as large as 1.4×10^3 with an excitation of 514.5 nm [15]. In the UV/vis spectra, no characteristic peak was identified in the sol state, but a very broad band developed around 550 nm as 17 nm-sized Pt particles were deposited onto an indium tin oxide (ITO) substrate. Accordingly, the origin of the Raman enhancement at Pt nanoaggregates was assumed to be electromagnetic. Since then, it has been questioned whether the EM effect would increase further by using Pt particles greater than 17 nm.

Very recently, it has been reported by Bigall et al. that Pt particles even greater than 100 nm can be prepared in laboratory conditions [16]. The SERS characteristics of those Pt nanoparticles films have thus been investigated in this work. Specifically, Pt particles with a nominal diameter of 28, 46, 72, and 105 nm were prepared and then the particles were packed into columns (film appearance).

Firstly, in view of the EM effect, a higher extinction in the visible region was

observed from the film assembled with larger Pt particles. The highest EF was obtained from a film comprised of 105 nm-sized Pt particles, in agreement with the EM enhancement mechanism. The EF of the film was not, however, greater than that of our earlier film fabricated using laser ablated 17 nm-sized Pt nanoparticles. This unexpected observation was explained by the fact that the Pt nanoparticles prepared by a seed-mediated growth method were actually composed of smaller (~7 nm in diameter) particles. Secondly, this study also finds that the chemical enhancement mechanism is operating, along with the electromagnetic enhancement mechanism, in the SERS of 4-ABT on Pt to show its b_2 -type bands, similarly to that on Ag.

Result and Discussion

Figure 1(a) shows the TEM images of four different Pt nanoparticles prepared in this work. Note that they are mostly spherical, and according to the histograms in Figure 1(b), their mean diameters are determined to be either 28 ± 7 or 46 ± 5 or 72 ± 4 or 105 ± 6 nm: the particles are highly monodispersed at all sizes. Figure 1(c) shows the UV/vis extinction spectra of these Pt particles in a colloidal state: the particle concentrations are the same in all UV/vis spectra. As can be seen in Figure 1(d), the wavelength of the peak maximum associated with the surface plasmon resonance is red-shifted from 250 to 500 nm almost linearly in proportion to the size of Pt nanoparticles.

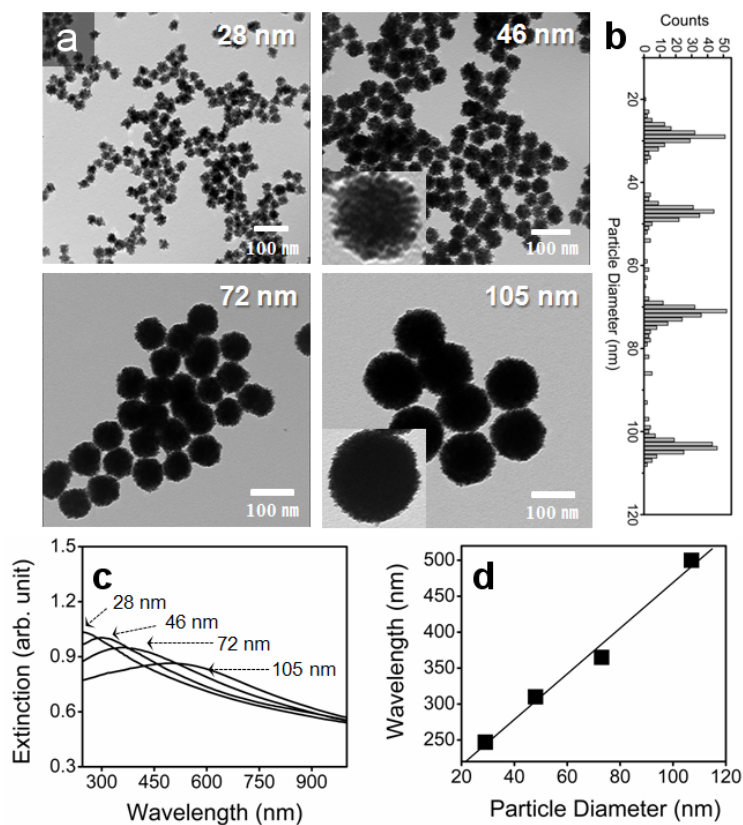


Figure 1. (a) TEM images of four different Pt nanoparticles and (b) their histograms; the magnified TEM images of 46 nm sized and 105 nm sized Pt nanoparticles are also shown in the insets. (c) UV-vis extinction spectra of Pt nanoparticles in a colloidal state (particle concentrations are the same in all spectra) and (d) the peak maximum drawn versus the size of Pt nanoparticles.

Figure 2(a) shows the UV/vis spectra of Pt nanoparticles films assembled on ITO. Hereafter the film made of 60 μL of 28 nm-sized Pt sol on ITO, for instance, is labeled S6(Pt-28 nm)/ITO, and others are similarly labeled: remember that particle concentration was the same in all Pt sols.

For all Pt films, a broad but distinct band occurs at ~ 330 nm, and then the absorbance decreases slowly until reaching a minimum in the infrared region: the

absorbance itself is increasing with increase in the size of the Pt nanoparticles.

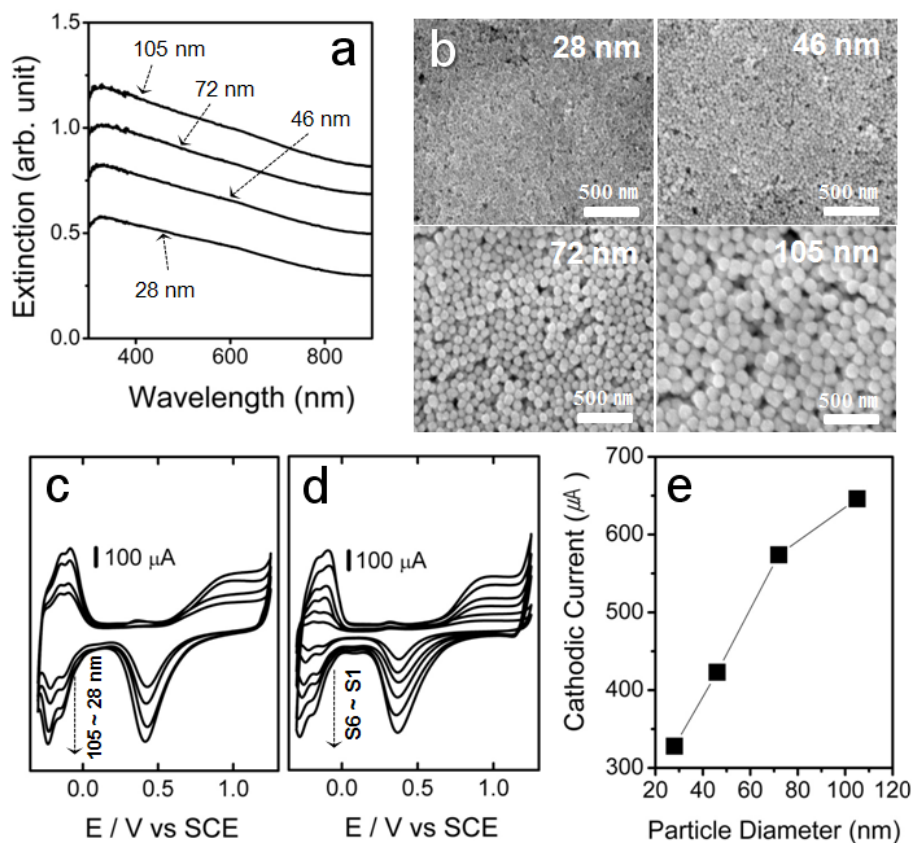


Figure 2. (a) UV-vis spectra of Pt S6 films assembled on ITO: See text. (b) FE-SEM images of Pt S6 films assembled on silicon wafers. (c) CVs of Pt S6 films in 0.1 M H₂SO₄ solution (scan rate) 0.05 V/s) (d) CVs of Pt S1 ~ S6 films fabricated using 105 nm sized Pt particles. (e) Cathodic current in (c) drawn versus size of Pt particles used in fabricating S6 films.

Herein, different spectral changes compared with the colloid samples must be attributable to the close-packed structure of Pt nanoparticles in the film state. In a colloid state, the maximum absorbance is identified around 500 nm, but in a film state, a broad but distinct band occurs at ~330 nm and then the absorbance

decreases in the visible region. Different spectral changes compared with the colloid sample could be attributable to the scattering-dominated extinction spectrum of Pt nanoparticles in the film state: the SPR absorption band might be completely buried in the extinction spectrum. Figure 2(b) shows the FE-SEM images of four S6 films with different particle diameters assembled on silicon wafers, i.e., S6(Pt-28 nm)/ITO, S6(Pt-46 nm)/ITO, S6(Pt-72 nm)/ITO, and S6(Pt-105 nm)/ITO. In all films, the Pt particles are packed closely as expected. Figure 2(c) shows the CVs of the four S6 films, comprised of differently sized Pt nanoparticles, measured by potential cycling between -0.30 and +1.25 V at 0.05 V/s in an aqueous 0.1 M H₂SO₄ solution. All CV profiles are identical, and also similar to that obtained with a conventional polycrystalline Pt electrode under the same conditions [17-22]. The peak appearing at -0.22 V at the cathodic site is due to the reduction of protons to gaseous hydrogen, and the peak around 0.4 V is associated with the desorption of gaseous oxygen. As expected, the cathodic current increases in proportion to the number of layers of Pt particles. Figure 2(d) shows the CVs measured using S1-S6 electrodes fabricated with 105 nm-sized Pt particles. As can be seen in Figure 2(e), the redox current also increases proportionally to the size of Pt particles in S6 films: A larger cathodic current is measured when larger particles are packed together. Recalling the fact that the charge density associated with the adsorption and desorption of H atoms on a polycrystalline Pt electrode amounts to 210 $\mu\text{C}/\text{cm}^2$ [17], the roughness factors of the S6(Pt-28 nm)/ITO, S6(Pt-46 nm)/ITO, S6(Pt-72 nm)/ITO, and S6(Pt-105 nm)/ITO films are determined to be 109, 137, 182, and 213, respectively. Similarly,

the roughness factors of the S1 to S5 films assembled from 105 nm Pt particles are 25, 61, 89, 128, and 157, respectively. Hence, the S6(Pt-105 nm)/ITO film has, among others, the highest electrochemical roughness factor in this work.

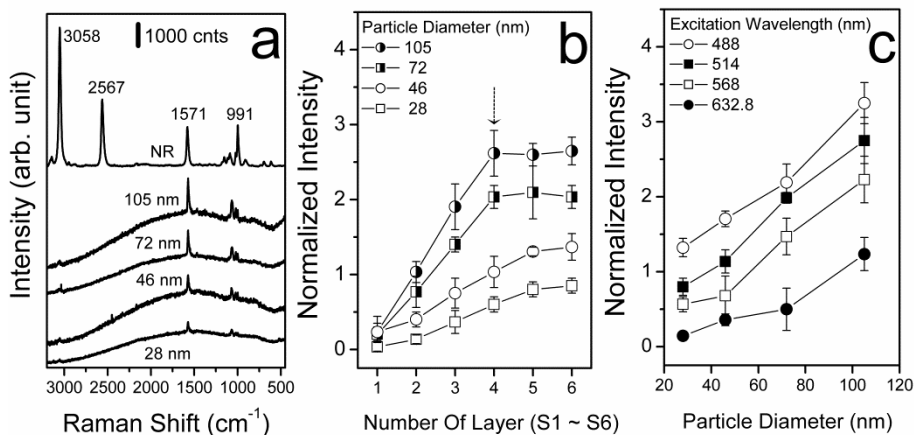


Figure 3. (a) Raman spectra of BT adsorbed on four different Pt S6 films, i.e., S6(Pt-28 nm)/ITO, S6(Pt-46 nm)/ITO, S6(Pt-72 nm)/ITO, and S6(Pt-105 nm)/ITO films, measured at 514.5 nm excitation: For comparison, the NR spectrum of BT in the neat state is also shown. (b) Peak intensity of ν_{8a} band of BT (normalized with respect to that of a silicon wafer at 520 cm^{-1}) measured at 514.5 nm excitation drawn versus the number of layers (S1 ~ S6) of four different Pt particles. (c) Normalized peak intensity of the ν_{8a} band of BT on S6 films drawn versus the size of Pt nanoparticles, as well as the excitation wavelengths.

Figure 3(a) shows the Raman spectra of BT adsorbed on four different S6 films measured using 514.5 nm radiation as the excitation source. The strongest Raman signal was observed from the S6(Pt-105 nm)/ITO film. All the peaks can be attributed to BT [23,24]. This is evident by comparing it with the normal Raman (NR) spectrum of BT, also shown in Figure 3(a). In the NR spectrum, the peaks at 3058, 1571, and 999 cm^{-1} are due to CH stretching, ring CC stretching (ν_{8a}), and ring CCC in-plane bending (ν_{12}) modes of BT, respectively, while the peaks at

2567 and 917 cm^{-1} are due to SH stretching and CSH bending vibration, respectively. In the Raman spectra of BT on Pt, one cannot find the counterparts of the latter two vibrational bands. Otherwise, all the peaks can be correlated with those in the NR spectrum. The absence of the SH group bands can be understood by presuming that BT is adsorbed on Pt as a thiolate by forming a Pt–S bond [24]. In Figure 3(b) is collectively summarized the variation in peak intensity of the ν_{sa} band of BT (normalized with respect to that of silicon wafer at 520 cm^{-1}) measured at 514.5 nm excitation in terms of the number of layers of four different Pt particles. Overall, a stronger signal is observed in the order of S6 > S5 > S4 > S3 > S2 > S1 films. However, for the films assembled with 72 and 105 nm-sized Pt particles, the Raman signal becomes saturated by the signal from the S4 films. Maxwell et al. reported a similar leveling off behavior of SERS intensity from a nanostructured thin film made of Ag nanoparticles [25]. In Figure 3(c) is collectively summarized the variation in peak intensity of the ν_{sa} band of BT on S6 films in terms of the size of Pt nanoparticles and the excitation wavelengths. Signal strength is observed in the order of size of the Pt particles, i.e. 105 > 72 > 46 > 28 nm, and 488 > 514.5 > 568 > 632.8 nm excitation. This correlates with the variation of the UV/vis absorbance of Pt films shown in Figure 2(a), suggesting that the electromagnetic enhancement mechanism is indeed operative in these films to show a strong SERS signal. On the other hand, the fact that the Raman signal is strongly dependent on the size of the Pt particles suggests that the chemical enhancement mechanism is rather insignificant in the present system. As observed here, the S4~S6(Pt-105 nm)/ITO films exhibited the strongest Raman signal for BT, so that subsequent

measurements were conducted using those kind of films. In particular, the surface enhancement factor (EF) was estimated using the S4(Pt-105 nm)/ITO film.

To estimate the EF [26], this study uses the following relationship: $EF = (I_{SERS}/I_{NR})(N_{NR}/N_{SERS})$ in which I_{SERS} and I_{NR} are the SERS intensity of BT on Pt and the NR intensity of BT in bulk, respectively, and N_{SERS} and N_{NR} are the number of BT molecules illuminated by the laser light to obtain the corresponding SERS and NR spectra, respectively. I_{SERS} and I_{NR} were measured for the ν_{8a} band and N_{SERS} and N_{NR} were calculated on the basis of the estimated concentration of surface BT species, the density of bulk BT, and the sampling areas. The surface concentration of BT on S4(Pt-105 nm)/ITO is assumed to be the same as that on gold and silver, i.e. $\sim 7.1 \times 10^{-10}$ mol/cm² [27]. Taking the sampling area (ca. 1 μ m in diameter) as well as the surface roughness factor (~ 128) into account, $N_{SERS} = 7.1 \times 10^{-16}$ mol. When taking the NR spectrum of pure BT, the sampling volume will be the product of the laser spot and the penetration depth (~ 15 μ m) of the focused beam; in a separate experiment, this work confirmed that the Raman signal reaches a steady state when the thickness of an organic film becomes greater than 15 μ m. As the density of BT is 1.07 g/cm³, N_{NR} is calculated to be 1.1×10^{-13} mol. Since the intensity ratio, I_{SERS}/I_{NR} , is measured to be ~ 1 at 514.5 nm excitation, EF can then be as large as 1.5×10^2 . This clearly indicates that SERS can be induced to occur even on a Pt substrate by visible laser irradiation. Nonetheless, it is also disappointing that the EF of a Pt film comprised of 105 nm-sized particles is smaller than that ($\sim 1.4 \times 10^3$) of our earlier Pt film fabricated with laser-ablated 17 nm-sized particles: Here, the earlier reported value, 1.9×10^2 , is modified to $1.4 \times$

10^3 by considering the newly estimated penetration depth of the laser beam.

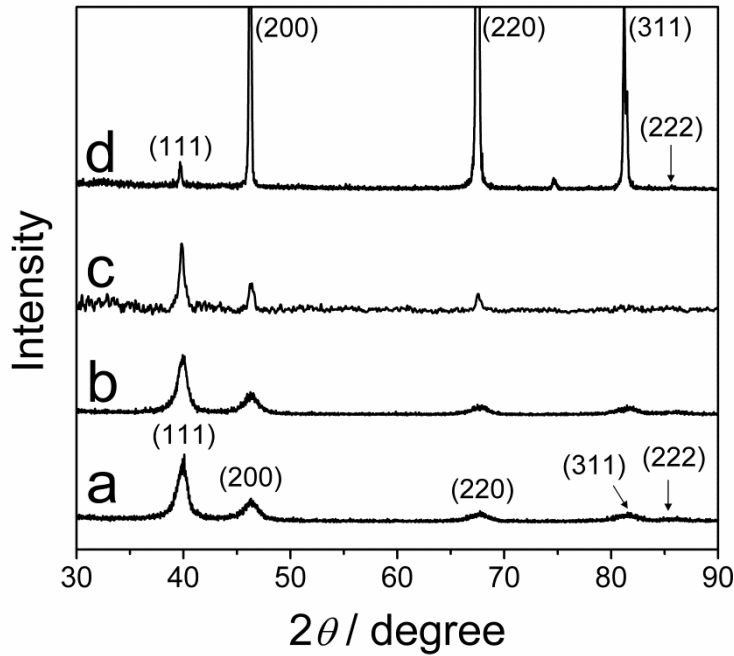


Figure 4. XRDs of (a) S6(Pt-7 nm) and (b) S6(Pt-105 nm) films assembled on silicon wafers: For comparison, the XRDs of (c) Pt laser ablated sol film and (d) a polycrystalline Pt foil are also shown.

A clue to explain the lower EF values is obtained from the XRD data. Figures 4(a) and (b) show the XRDs of two S6 Pt films fabricated with either the initial seed particles or the 105 nm-sized particles. For comparison, the XRD of a Pt film comprised of laser-ablated particles, as well as that of a polycrystalline Pt foil, were also included in Figures 4(c) and (d). In all diffractograms, the peaks at 2θ values of 39.7° , 46.2° , 67.4° , and 81.2° can be attributed to the reflections of (111), (200), (220), and (311) crystalline planes of cubic Pt, respectively. It is seen that the (111) peak is dominant in the XRD of Pt particle films, although the peak is negligibly weak in the XRD of a Pt foil: the intensity ratio of the (111) and (200) reflections,

i.e. $I_{(111)}/I_{(200)}$, is 2.9 (Pt seed), 2.9 (Pt 105 nm), 2.4 (Pt laser), and 0.07 (Pt foil). This suggests that the (111) surface is energetically the most favorable in the nanoparticle realm: Pt nanoparticles prepared by chemical method in this work exhibit the (111) surface more abundantly than those prepared by laser ablation method. Another noteworthy point in Figure 4 is that there are significant differences in the bandwidths. Using the Scherrer equation [28], the average sizes of Pt particles estimated by analyzing the (111) peak widths at half-maximum of the XRD data. The sizes determined were 7.1 nm (Pt seed), 7.2 nm (Pt 105 nm), 16 nm (Pt laser), and 57 nm (Pt foil). We already reported that the size of laser ablated Pt particles determined by TEM analysis (17 nm) is hardly different from that determined by the analysis of XRD peaks (16 nm) [13-15]. For the film assembled in this work using Pt seeds, the TEM and XRD analyses also resulted in the same size (~7 nm). However, the film supposedly composed of 105 nm-sized Pt particles (in accordance with the TEM analysis) turns out, from the XRD analysis, to be comprised of 7.2 nm-sized particles. The latter size is exactly the same as that of the seed. Hence, all Pt nanoparticles prepared here by a seed-mediated growth method are assumed to consist of smaller (~7 nm in diameter) particles; magnified TEM images of the 46 nm-sized and 105 nm-sized Pt nanoparticles composed of ~7 nm-sized particles are shown in the insets of Figure 1(a). This must be why the EF of a Pt film comprised of 105 nm-sized particles was smaller than that of a Pt film fabricated using laser-ablated particles [13-15].

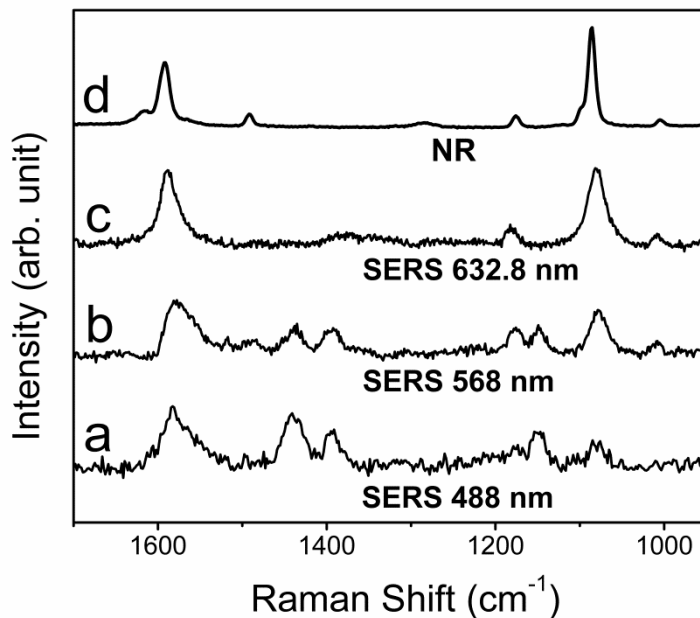


Figure 5. SERS spectra of 4-ABT on S6(Pt-105 nm)/ITO film taken using (a) 488, (b) 568, and (c) 632.8 nm radiation as the excitation source: (d) NR spectrum of 4-ABT in neat solid state taken at 568 nm excitation.

Figures 5(a), (b) and (c) show the Raman spectra of 4-ABT on a S6(Pt-105 nm)/ITO film taken using 488, 568, and 632.8 nm radiation as the excitation source, respectively. For comparison, the NR spectrum of 4-ABT is shown in Figure S1-5(d). The NR spectral pattern of 4-ABT is independent of the excitation wavelength, but it is seen in Figures 5(a), (b) and (c) that the SERS spectral pattern of 4-ABT on Pt is highly dependent on the excitation wavelength. All the SERS peaks of 4-ABT in Figure 5(c) can be correlated with those in the NR spectrum in Figure 5(d). In the SERS spectra in Figures 5(a) and (b), however, there are additional peaks present that are difficult to correlate with the NR peaks in Figure 5(d).

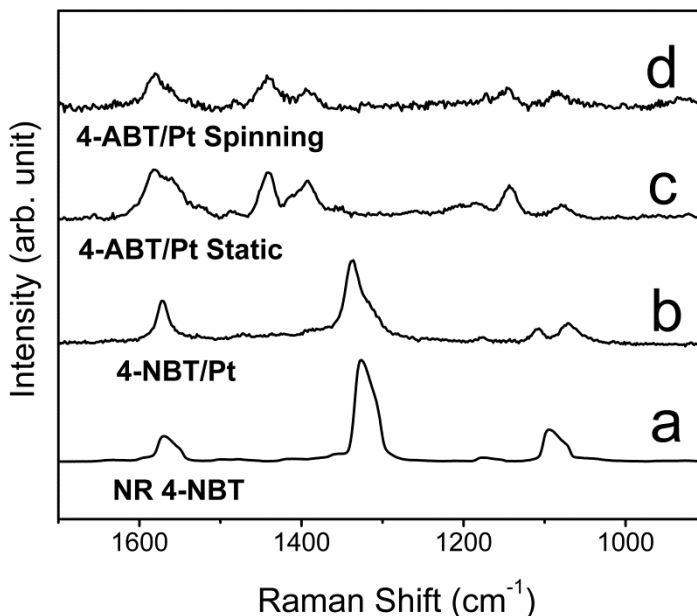


Figure 6. (a) NR spectrum of 4-NBT in neat solid state and (b) SERS spectrum of 4-NBT on S6(Pt-105 nm)/ITO film measured at 488 nm excitation. SERS spectra of 4-ABT on S6(Pt-105 nm)/ITO measured under (c) static and (d) spinning at 3000 rpm at 488 nm excitation.

For a long time, those bands were classified as the b_2 type bands of 4-ABT and their appearance in the SERS spectra (on Ag nanoaggregates) was attributed to the involvement of the chemical enhancement mechanism in SERS [1]. Figure 5 clearly shows that the b_2 type bands, which are markers for chemical enhancement, are increasing in relative intensity toward shorter wavelength; this indicates an onset of a charge-transfer resonance in the SERS spectral feature of 4-ABT on Pt. Very recently, however, Tian et al. reported that those bands (observable using a roughened Ag electrode) should result from the photoreaction of 4-ABT, most probably azo molecules [3]. Nonetheless, the fact that such bands can be seen even in a nanogap electrode, in which 4-ABT is first self-assembled on planar Au and

then Au (or Ag) nanoparticles are adsorbed on the pendent amine groups, suggests that the photoreaction may not be the sole reason for the appearance of those bands [32-34]. Therefore, this study in more detail examined the Raman spectral feature of 4-ABT on Pt by measuring spectra not only at different excitation wavelengths but also at different potentials. In this study is examined, firstly, whether the Pt film is photoactive. It is well known that 4-NBT on Ag is converted to give a SERS spectrum of 4-ABT by the irradiation of a visible laser [35-39]. As shown in Figure 6(b), the SERS spectrum of 4-NBT assembled on a S6(Pt-105 nm)/ITO film is invariant, however, even after prolonged exposure to 488 nm radiation. For comparison, the NR spectrum of 4-NBT is also shown in Figure 6(a). On the other hand, we have to mention that, as can be seen in Figures 6(c) and (d), the SERS spectral pattern of 4-ABT on Pt is also invariant, regardless of the spinning of the sample even up to 3000 rpm, as long as the excitation wavelength is fixed. These observations suggest that 4-ABT is hardly subjected to photoreaction on a Pt surface. The additional peaks observed in Figures 5(a) and (b) would then be due to the b_2 -type bands of 4-ABT, not due to a photoreaction product like an azo compound. On this basis, this study measured the potential-dependent SERS spectra of 4-ABT on Pt at various excitation wavelengths.

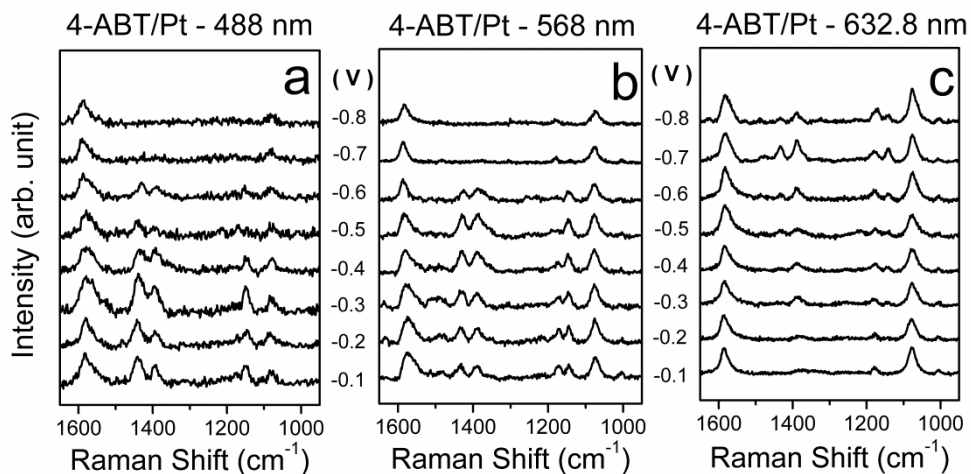


Figure 7. Potential-dependent SERS spectra of 4-ABT on S6(Pt-105 nm)/ITO measured using (a) 488, (b) 568, and (c) 632.8 nm radiation as the excitation source.

Figures 7(a), (b) and (c) show the potential-dependent SERS spectra of 4-ABT measured using 488, 568, and 632.8 nm radiation as the excitation sources, respectively. Note that all the spectra were reversibly observed during the potential cycling between -0.1 and -0.8 V. Variation in the SERS spectral pattern of 4-ABT on Pt is affected, however, not only by the electrode potential but also by the excitation wavelength. This is evident from Figure 8, which shows the normalized peak intensity of the ring 19b band, a typical b_2 -type band of 4-ABT, drawn versus the electrode potential at three different excitation wavelengths.

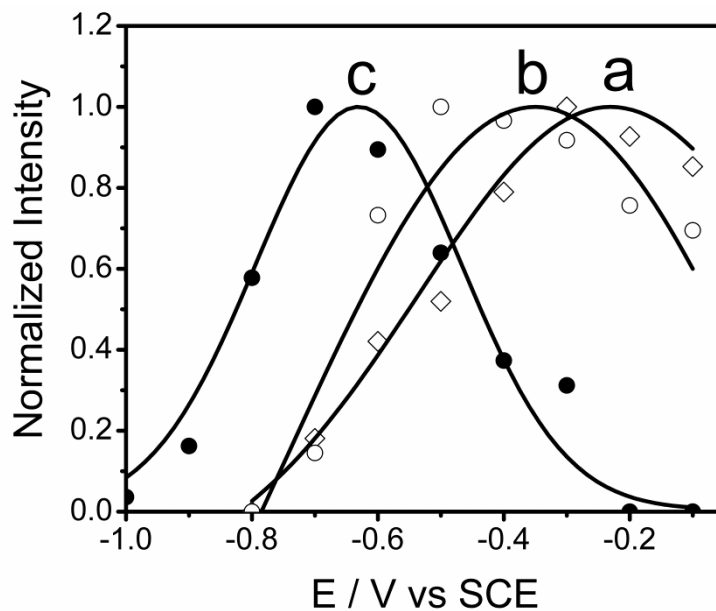


Figure 8. Normalized peak intensity of ring 19b band at 1439 cm^{-1} in Figure 7 drawn versus the electrode potential at (a) 488 or (b) 568 or (c) 632.8 nm excitation: Solid lines represent the Gaussian fitting.

The solid lines in Figure 8 represent the Gaussian fitting of the peak intensities. At higher excitation wavelengths, the peak maximum (E_{max}) occurs at lower electrode potentials: at -0.63 V at 632.8 nm (1.96 eV) excitation, at -0.35 V at 568 nm (2.19 eV) excitation, and at -0.24 V at 488 nm (2.54 eV) excitation. The $dE_{max}/d(h\nu)$ slope, the slope of the peak maximum as a function of excitation energy, obtained in this work by the linear fitting is 0.993 V/eV. The positive slope of the curve and the fact that it is close to unity can be taken as the evidence of the metal to molecule charge-transfer nature of the spectral intensities [1].

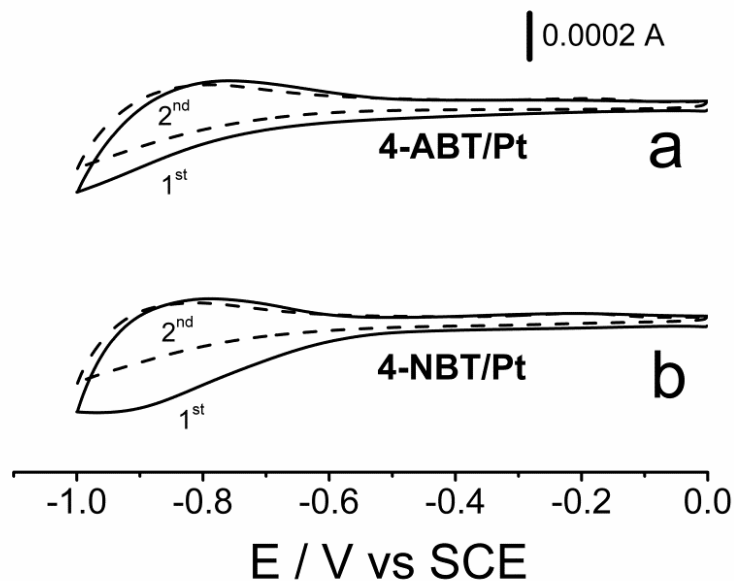


Figure 9. CVs of (a) 4-ABT and (b) 4-NBT on S6(Pt-105 nm)/ITO in 0.1 M NaClO₄ aqueous solution. The solid and dashed lines show the first and second cycles, respectively.

Additionally, as can be seen in Figure 9, the CV of 4-ABT/Pt is also invariant with respect to the potential cycling between 0 and -1.0 V. In the CV of 4-NBT/Pt, 4-NBT is reduced to 4-ABT in the first cycling, but once 4-ABT is formed, the CV of 4-NBT remains the same as that of 4-ABT. This study indicates that although 4-NBT on Pt can be reduced to 4-ABT on Pt by electrochemistry, 4-NBT on Pt is not photoreduced to 4-ABT on Pt. Therefore, all results can be understood by presuming that the b₂-type bands are associated with a chemical enhancement mechanism in SERS, similar to that claimed by Osawa et al. for 4-ABT adsorbed on Ag electrodes [1].

Summary and Conclusion

Four different Pt nanoparticles with nominal diameters of 28, 46, 72, and 105 nm were prepared by a seed-mediated growth method. Their UV/vis absorption maximum associated with the surface plasmon resonance varied almost linearly from 250 to 500 nm in proportion to the size of the Pt nanoparticles. When assembled into films on ITO, regardless of the size of the Pt nanoparticles, a broad but distinct band occurred at ~330 nm, and then the absorbance decreased slowly until reaching a minimum in the infrared region: A higher absorbance was, however, observed from a film assembled with larger Pt particles. In agreement with the electromagnetic enhancement mechanism in SERS, a higher Raman intensity was observed at shorter excitation wavelengths from adsorbates on a Pt film made of 105 nm-sized Pt particles. The enhancement factor (EF) determined at 514.5 nm excitation was, however, at best 1.5×10^2 , which is about an order of magnitude smaller than that of our earlier Pt film fabricated with laser-ablated 17 nm-sized particles. Consulting the XRD analyses, the smaller EF value was attributed to the fact that even the 105 nm-sized Pt particles were, in fact, composed of 7.2 nm-sized seed particles. Additionally, using the Pt film assembled in this work, it is found that 4-NBT is only weakly photoreactive, in contrast with that on Ag. In addition, there are found that the SERS spectral pattern of 4-ABT on Pt is variable not only with changes in the electrode potential but also by altering the excitation wavelength. These spectral variations could be understood by presuming that the chemical enhancement mechanism is also operating in this system, along with the electromagnetic enhancement, to show the b_2 -type bands of 4-ABT similarly to that

on Ag electrodes.

References

1. Osawa, M.; Matsuda, N.; Yoshii, K.; Uchida, I. *J. Phys. Chem.* **1994**, *98*, 12702.
2. Fang, Y.; Li, Y.; Xu, H.; Sun, M. *Langmuir* **2010**, *26*, 7737.
3. Huang, Y. F.; Zhu, H. P.; Liu, G. K.; Wu, D. Y.; Ren, B.; Tian, Z. Q. *J. Am. Chem. Soc.* **2010**, *132*, 9244.
4. Tian, Z. Q.; Ren, B.; Mao, B, W. *J. Phys. Chem. B* **1997**, *101*, 1338.
5. Tian, Z. Q.; Gao, J. S.; Li, X. Q.; Yao, L.; Ren, B.; Huang, Q. J.; Cai, W. B.; Liu, F. M.; Mao, B, W. *J. Raman Spectrosc.* **1998**, *29*, 703.
6. Tian, Z. Q.; Ren, B.; Wu, D.-Y. *J. Phys. Chem. B* **2002**, *106*, 9463.
7. Tian, Z. Q.; Ren, B.; Li, J.-F.; Yang, Z.-L. *Chem. Comm.* **2007**, 3514.
8. Tian, N.; Zhou, Z.-Y.; Sun, S.-G.; Cui, L.; Ren, B.; Tian, Z. Q. *Chem. Comm.* **2006**, 4090.
9. Cai, W. B.; Ren, B.; Li, X. Q.; She, C. X.; Liu, F. M.; Cai, X. W.; Tian, Z. Q. *Surf. Sci.* **1998**, *406*, 9.
10. Creighton, J. A.; Eadon, D. G. *J. Chem. Soc., Faraday Trans* **1991**, *87*, 3881.
11. Henglein, A.; Ershov, B. G.; Malow, M. *J. Phys. Chem.* **1995**, *99*, 14129.
12. Janata, E.; Henglein, A.; Ershov, B. *J. Phys. Chem.* **1996**, *100*, 1989.
13. Kim, N. H.; Kim, K. *Chem. Phys. Lett.* **2004**, *393*, 478.
14. Kim, N. H.; Kim, K. *J. Raman Spectrosc.* **2005**, *36*, 623.
15. Kim, N. H.; Kim, K. *J. Phys. Chem. B* **2006**, *110*, 1837.

16. Bigall, N, C.; Härtling, T.; Klose, M.; Simon, P.; Eng, L, M.; Eychmüller, A. *Nano Lett.* **2008**, *8*, 4588.
17. Bard, A. Faulkner, L, R. *Electrochemical Methods; Fundamentals and Applications*, 2nd ed., Wiley: New York, **2001**.
18. Park, S.; Yang, P.; Corredor, P.; Weaver, M, J. *J. Am. Chem. Soc.* **2002**, *124*, 2428.
19. Morzek, M, F.; Xie, Y.; Weaver, M, J. *Anal. Chem.* **2001**, *73*, 5953.
20. Zou, S.; Weaver, M, J. *Anal. Chem.* **1998**, *70*, 2387.
21. Gómez, R.; Pérez, J, M.; Solla-Gullón, J.; Montiel, V.; Aldez, A. *J. Phys. Chem. B* **2004**, *108*, 9943.
22. Gómez, R.; Solla-Gullón, J.; Pérez, J, M.; Aldez, A. *J. Raman Spectrosc.* **2005**, *36*, 613.
23. Joo, T, H.; Kim, M, S.; Kim, K. *J. Raman Spectrosc.* **1987**, *18*, 57.
24. Bryant, M, A.; Joa, S, L.; Pemberton, J, E. *Langmuir* **1992**, *8*, 753.
25. Maxwell, D, J.; Emory, S, R.; Nie, S. *Chem. Mater.* **2001**, *13*, 1082.
26. Yu, H, Z.; Zhang, J.; Zhang, H, L.; Liu, Z, F. *Langmuir* **1999**, *15*, 16.
27. Wan, L, J.; Terashima, M.; Noda, H.; Osawa, M. *J. Phys. Chem. B* **2000**, *104*, 3563.
28. Borchert, H.; Shevchenko, E, V.; Robert, A.; Mekis, I.; Kornowski, A.; Grübel, G.; Weller, H. *Langmuir* **2005**, *21*, 1931.
29. Xuan, S.; Wang, Y, J.; Yu, J, C.; Leung, K, C. *Chem. Mater.* **2009**, *21*, 5079.
30. Osawa, M.; Matsuda, N.; Yoshii, K.; Uchida, I. *J. Phys. Chem.* **1994**, *98*, 12702.
31. Huang, Y,-F.; Zhu, H,-P.; Liu, G,-K.; Wu, D,-Y.; Ren, B.; Tian, Z, Q. *J. Am.*

Chem. Soc. **2010**, *132*, 9244.

32. Kim, K.; Yoon, J, K. *J. Phys. Chem. B* **2005**, *109*, 20731.
33. Yoon, J, K.; Kim, K.; Shin, K, S. *J. Phys. Chem. C* **2009**, *113*, 1769.
34. Kim, K.; Lee, H, B.; Yoon, J, K.; Shin, D.; Shin, K, S. *J. Phys. Chem. C* **2010**, *114*, 13589.
35. Han, S, W.; Lee, I.; Kim, K. *Langmuir* **2002**, *18*, 182.
36. Lee, S, J.; Kim, Kim. *Chem. Phys. Lett.* **2003**, *378*, 122.
37. Kim, K.; Lee, I.; Lee, S, J. *Chem. Phys. Lett.* **2003**, *377*, 201.
38. Kim, K.; Lee, I. *Langmuir* **2004**, *20*, 7351.
39. Kim, K.; Lee, S, J.; Kim, K, L. *J. Phys. Chem. B* **2004**, *108*, 16208.

3-2. Effect of VOCs on SERS of 4-ABT on Ag: Comparison with the Potential Dependence

Introduction

It is usually difficult to identify the effect of volatile organic chemicals (VOCs) on the surface characteristics of metals. In most cases, the effect would be negligibly small, but in some cases, especially for nanodevices operating in ambient conditions, this could be pivotal in running them in optimal condition [1-8]. Unfortunately, no device is yet available to measure the effect directly, but Kim et al. reported recently that the VOC effect, at least on nanostructured gold and silver, can be identified, although indirectly, by means of SERS of isocyanides [9-11]. For instance, in the presence of acetone the NC stretching band of 2,6-dimethylphenylisocyanide (2,6-DMPI) on Au blue-shifted by as much as 6 cm^{-1} , while the same band red-shifted by as much as 20 cm^{-1} in the presence of ammonia [9]. By referring to ab initio molecular orbital calculations, the blue- and red-shifts could be understood by attributing them to the electron accepting and electron donating properties of acetone and ammonia from/to Au, respectively [10]. The lone pair electrons of the isocyanide group are antibonding with respect to the NC bond so that the donation of these electrons to Au, occurring in the presence of acetone, must result in the strengthening of the NC bond to show a blue-shift, while

the opposite occurs in the presence of ammonia [11]. Considering the fact that similar blue- and red-shifts are readily observed in the potential-dependent SERS spectra of isocyanides, the effect of VOCs can also be regarded as the alteration of the surface potential of metal substrates.

4-ABT is an unusual molecule in the sense that its SERS spectral features are dependent not only on the kinds of SERS substrates but also on the measurement conditions [12-17]. Although only peaks assignable to totally symmetric (a_1) vibrations are exclusively observed in the normal Raman (NR) spectrum, non- a_1 type peaks are additionally identified in the SERS spectrum. The relative intensity of these peaks with respect to the a_1 type bands is clearly dependent not only on the excitation wavelength but also on the electrode potential applied to the SERS substrate [18-22]. By assigning those bands to b_2 symmetry vibrations, their strong appearance was interpreted by Osawa et al. as the signature of an intensity borrowing from an intense $\pi \rightarrow \pi^*$ molecular transition (${}^1A_1 \rightarrow {}^1B_2$) at 300 nm [20]. For the past 15 years, 4-ABT has thus been regarded as a model compound for studying the chemical enhancement mechanism in SERS [18-22]. In line with this, Lombardi and Birke explained the SERS spectrum of 4-ABT using only the Herzberg-Teller surface selection rules [21]. Very recently, however, a number of researchers have come up with a different explanation for the appearance of these “ b_2 -type” bands. The most extreme explanation is that the bands assigned to b_2 symmetry by Osawa et al. are not due to 4-ABT after all but due to the a_g modes of dimercaptoazobenzene (DMAB) supposedly produced from 4-ABT via a catalytic coupling reaction on metal substrates [23,24].

Recently, Kim et al. and others have investigated the SERS of 4-ABT positioned in the gap of metal nanostructures [25-27]. When 4-ABT was adsorbed on a flame-annealed Au substrate, no Raman peak was identifiable, but as silver or gold nanoparticles were adsorbed further onto the pendent amine groups of 4-ABT, a very intense Raman spectrum was obtained. In those research, not only a_1 type bands but also the b_2 -type bands of 4-ABT were distinctly observed in these spectra. Considering the fact that an azo compound in *cis* configuration would be energetically unfavorable on an atomically flat gold terrace, it is unlikely that the b_2 -type bands observed were due to the formation of DMAB. In this sense, it is tempting to re-examine the SERS spectra of 4-ABT, especially on Ag, but this time subjected to different VOC environments. If the surface potential of nanostructured Ag is varied by VOCs, as surmised before, the b_2 -type bands will be variable over a wide range, as observed in electrochemical environments. Moreover, if azo compounds were to form from 4-ABT, the b_2 -type bands should appear more preferentially under the flow of VOCs which could increase the surface potential of Ag, and the opposite should occur under the flow of VOCs which were lowering the surface potential of Ag. If this were not to be the case, the appearance of the b_2 -type bands would have nothing to do with the surface-induced photoreaction. Their appearance would then have to be attributed to the intrinsic character of 4-ABT, possibly associated with the chemical enhancement mechanism in SERS. On this basis, the purpose of this work is to clarify the origin of the b_2 -type bands of 4-ABT by virtue of the VOC effect on Ag.

Results and Discussion

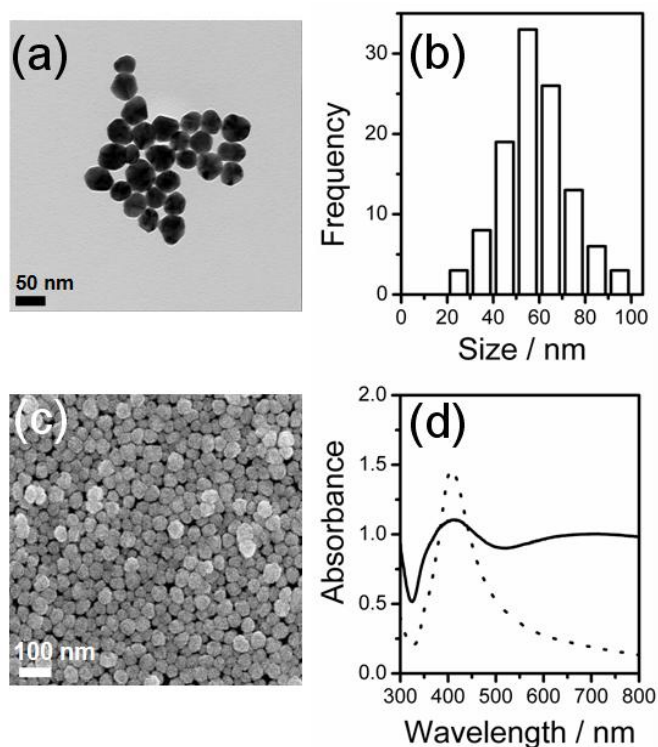


Figure 1. (a) TEM image of Ag nanoparticles and (b) a histogram of the particle size distribution. (c) FE-SEM image of Ag nanoaggregates in a film state. (d) UV-vis extinction spectra of Ag nanoparticles in colloid (broken line) and film (full line) states.

Figure 1(a) shows the TEM image of Ag nanoparticles prepared in this work. The nanoparticles are mostly spherical with a mean diameter of 55 nm (See size histogram in Figure 1(b)). As FE-SEM image shown in Figure 1(c), the Ag particles are packed closely in a film state. Figure 1(d) shows the UV-vis absorption spectra of Ag particles in a colloid state and in a film state. In the colloid state, the maximum absorbance is identified at 406 nm, but in the film state, a broad and featureless band occurs over the whole visible region. Consulting the

electromagnetic enhancement mechanism in SERS, it would then be possible to conduct an excitation wavelength dependence study specifically in the region of visible wavelengths [30].

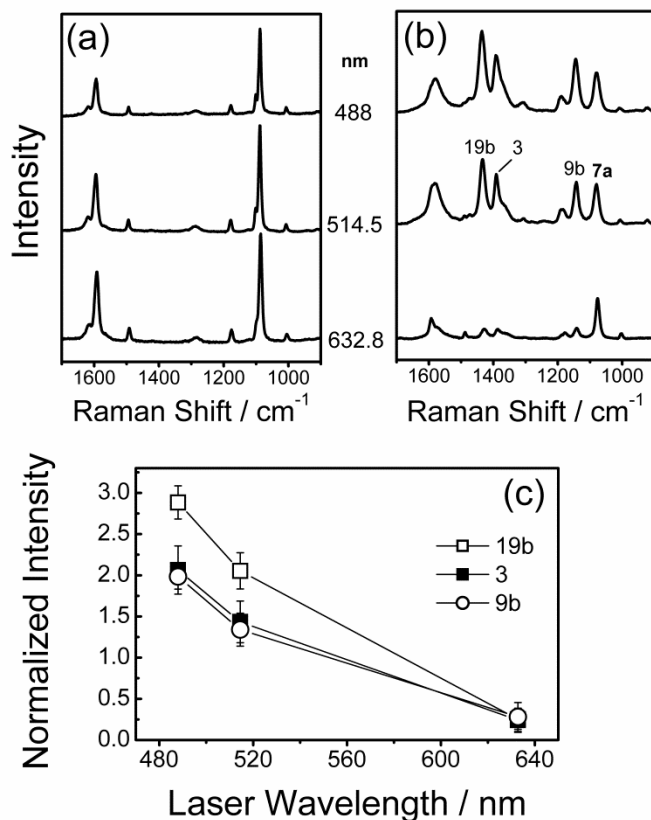
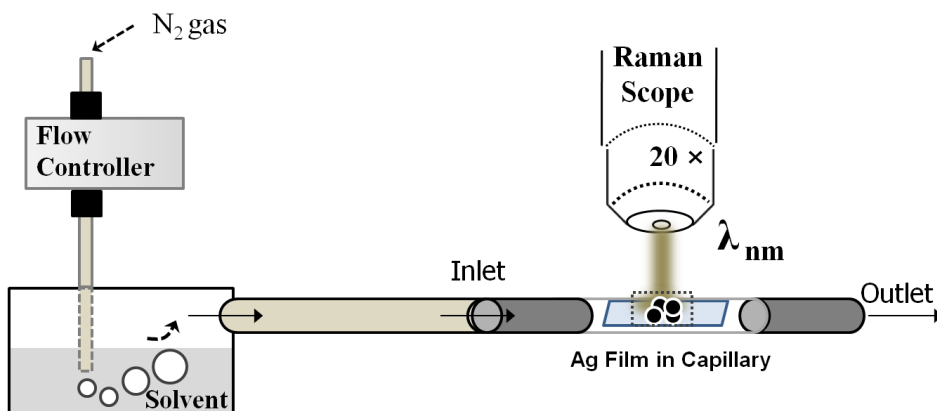


Figure 2. (a) NR of 4-ABT in a neat solid state and (b) its SERS spectra on Ag measured under the flow of N₂ using 488, 514.5, 568, and 632.8 nm radiation as the excitation sources, and (c) the normalized peak intensities of the 3, 9b, and 19b bands relative to the 7a band in (b) drawn versus the excitation wavelength.

Figure 2(a) shows the normal Raman (NR) spectra of 4-ABT in a neat solid state measured using 488, 514.5 or 632.8 nm radiation as the excitation source. The NR spectral pattern is largely independent of the excitation wavelength.



Scheme 1. A schematic diagram showing how to measure the effect of VOCs on the SERS of 4-ABT adsorbed on an Ag nanoparticle film on mica.

The major peaks summarized in Table 1 are mostly of a_1 type vibrations [25]. Figure 2(b) shows the SERS spectra of 4-ABT on Ag taken under the flow of N_2 using 488, 514.5 or 632.8 nm radiation as the excitation source (see Scheme 1). The SERS spectral pattern under the flow of N_2 was negligibly different from that found in ambient conditions. Nevertheless, the SERS spectral pattern was very susceptible to the excitation wavelength. It is important to mention that the SERS spectra were dominated by four bands, but whose counterparts were not found in the NR spectra, except for one at 1076 cm^{-1} . If no reaction had occurred, the three bands at 1144 , 1390 , and 1435 cm^{-1} could be attributed to the b_2 -type ring 9b, 3, and 19b modes of 4-ABT, respectively, while the remaining one at 1076 cm^{-1} could be assignable to the a_1 -type ring 7a mode (See Table 1).

Table. 1 Raman spectral peaks of 4-Aminobenzenethiol measured in free and surface adsorbed states using the excitation laser of 488, 514.5, and 632.8 nm

Normal Raman ^a	SERS			Vibrational assignment ^b
	488/nm	514.5/nm	632.8/nm	
Neat (Solid)				
3050vw				vCH, 2(a ₁)
2551vw				vSH
1616w				δNH
1593m	1591w	1591w	1591m	vCC, 8a(a ₁)
	1582m	1582m	1583w	vCC, 8b(b ₂)
1492vw	1488vw	1487w	1487w	vCC+δCH, 19a(a ₁)
	1435s	1435s	1434w	vCC+δCH, 19b(b ₂)
	1390m	1390m	1390w	vCC+δCH, 3(b ₂)
	1309vw	1309vw		vCC+δCH, 14(b ₂)
1176w	1187w	1187w	1184vw	δCH, 9a(a ₁)
	1144m	1144m	1143w	δCH, 9b(b ₂)
1087m	1076m	1076m	1075s	vCS, 7a(a ₁)
1008vw	1006w	1006w	1004vw	γCC+γCCC, 18a(a ₁)
	921vw	920vw	920vw	πCH, 5b(b ₁)
907vw				δSH
713vw	716vw	716vw	715vw	πCH+πCS+πCC, 4b(b ₁)
644w	639vw	639vw	641vw	γCCC, 12(a ₁)
519vw				γCCC, 16b(b ₁)

^a Wavenumber is in units of cm⁻¹. ^b Taken from ref. 27, v denoting stretch; δ and γ, bend; π, wagging; τ, torsion; vs, very strong; s, strong; m, medium; w, weak; and vw, very weak. The ring modes correspond to those of benzene under C_{2v} symmetry.

Overall, a more intense SERS spectrum was measured by excitation with radiation of 488 > 514.5 > 632.8 nm in that order. Since the b₂-type bands were observed only in the SERS spectra, it would be more practical to examine their intensity

variation after normalizing with respect to that of the 7a band. Figure 2(c) shows the normalized peak intensities of the 3, 9b, and 19b bands drawn as a function of the excitation wavelength. Clearly, all the b_2 -type bands become more enhanced as the excitation wavelength is decreased. The pattern of the intensity variation of the ring 19b mode differs, though only slightly, from those of the ring 3 and 9b modes. It is a natural supposition that if all of these b_2 -type bands were due to a single photoreaction product and if there were no SERS chemical enhancement effect, their intensity variation should have appeared the same.

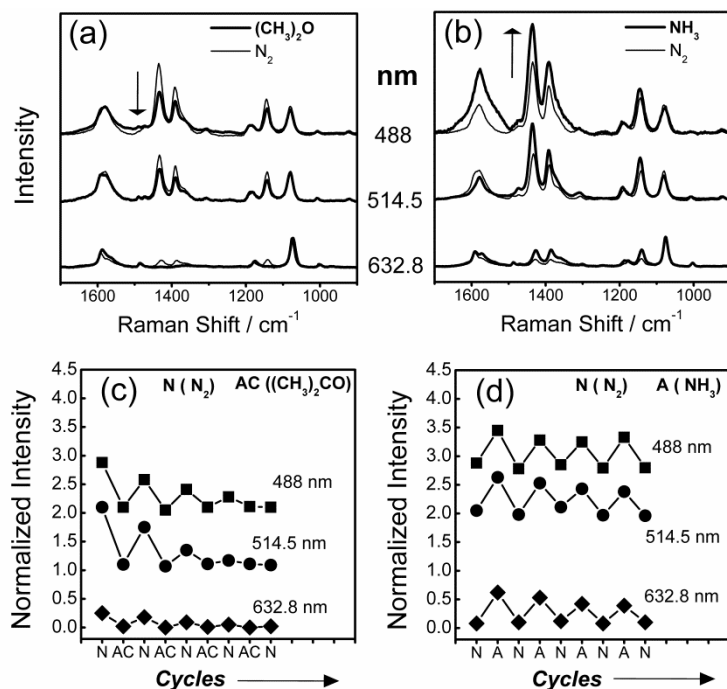


Figure 3. SERS spectra of 4-ABT on Ag measured under the flow of (a) acetone and (b) ammonia using 488, 514.5, 568, and 632.8 nm radiation as the excitation sources. (c) Normalized intensities of 19b, 9b, and 3 bands relative to 7a band, plotted in terms of VOCs and excitation wavelengths used in this study. (d) The intensity ratio of the 19b to 7a bands determined under the alternative flow of NH₃ and N₂.

Figures 3(a) and (b) show the SERS spectra of 4-ABT on Ag measured under the flow of acetone and ammonia, respectively, using 488, 514.5, and 632.8 nm radiation as the excitation sources. The peaks of acetone and ammonia were not observable, probably due to their intrinsically small Raman cross-sections and/or the presence of very limited amounts on Ag [9-11]. The SERS spectral pattern of 4-ABT was nonetheless affected by the presence of VOCs. Although a negligible peak shift was observed, the normalized peak intensities of the b_2 -type bands clearly varied in response to exposure to VOCs. Table 2 lists the values of these normalized intensities collectively in terms of VOCs and excitation wavelengths used in this study. It is evident that the normalized intensity of the b_2 -type bands is dependent not only on the excitation wavelength but also on the kind of VOCs to which 4-ABT on Ag is exposed.

Table 2. Normalized intensities of 19b, 9b, and 3 bands relative to 7a band in terms of VOCs and excitation wavelengths used in this study.

Nitrogen gas				
mode		19b	9b	3
Laser Wavelength (nm)	488	2.90	2.20	2.00
	514.5	2.10	1.40	1.30
	632.8	0.25	0.24	0.28
Acetone vapor				
mode		19b	9b	3
Laser Wavelength (nm)	488	2.10	1.40	1.00
	514.5	1.10	1.00	0.60
	632.8	0.02	0.00	0.00
Ammonia vapor				
mode		19b	9b	3
Laser Wavelength (nm)	488	3.50	2.50	2.40
	514.5	2.60	1.70	1.50
	632.8	0.62	0.57	0.58

There have to mention that the NR spectral pattern of 4-ABT was not affected at all by the VOCs of acetone and ammonia, either in a neat solid state or in a solution state dissolved in ethanol. This would mean that the direct molecular interaction of 4-ABT with $(\text{CH}_3)_2\text{CO}$ and NH_3 should be small. The SERS spectral variation in Figures 3(a) and (b) must then be caused by the interaction of VOCs with the Ag substrate. According to the cyclic voltammometry data shown in Figure. 4, there are multiple vacant sites on the Ag substrate even after the self-assembly of 4-ABT onto it in a concentrated solution.

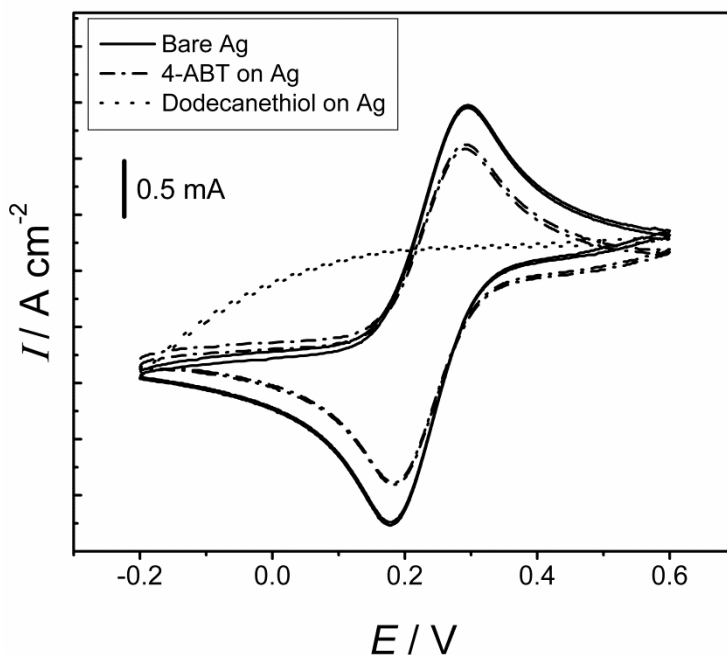


Figure 4. Cyclic voltammograms measured at a scan rate of 50 mV s^{-1} , using either a bare Ag or 4-ABT-adsorbed Ag or dodecanethiol adsorbed Ag electrode soaked in an aqueous solution composed of 0.1 M KCl and 1 mM $\text{K}_3\text{Fe}(\text{CN})_6$.

No redox peaks are observable using a dodecanethiol-adsorbed Ag electrode. Conversely, redox peaks due to ferricyanide can be distinctly observed using a 4-ABT-adsorbed Ag electrode, similar to a bare Ag electrode. This work noticed separately that the interaction of acetone with Ag should be fairly strong since the intensity variations of b_2 -type bands by the exposure to acetone did not restore to the original values by purging with N_2 after several cycles (Figure 3(c)). In contrast, the interaction of ammonia with Ag appeared weaker than that of acetone since the shifted b_2 -type bands were repeatedly restored to the original state simply by purging with N_2 , as illustrated in Figure 3(d).

Table 3. Binding energies of acetone and ammonia interacting with a single Ag atom, and the accompanying change in the net charges of the Ag atom.

	Ag (CH ₃) ₂ O	Ag NH ₃
Binding Energy (kJmol ⁻¹)	-7.6	-36.4
Net Charge of Ag Atom (e) ^b	+0.034	-0.143

^aComputed by use of the Gaussian 03W suite: LANL2DZ basis sets were used for Ag atoms, while 6-31+G(d) basis sets were used for all atoms of acetone and ammonia.

^bAtomic polar tensor-based net charge [31].

In order to see the possible interaction of acetone and ammonia with Ag, this work has carried out a simple ab initio quantum mechanical calculation [31]. At first, the binding energy and then the atomic polar tensor based charge population were computed for acetone and ammonia interacting with a single Ag atom using the Gaussian 03W suite at the B3LYP level theory. In this calculation, LANL2DZ basis sets were used for the Ag atom, while 6-31+G(d) basis sets were used for all atoms of acetone and ammonia. As one would expect, the Ag atom interacted either with

the oxygen atom of acetone or with the nitrogen atom of ammonia. As can be seen in Table 3, all the interactions were attractive. The interaction energy of acetone with Ag was, however, calculated to be lower than that of ammonia with Ag. This may not conform with the observation that the b_2 -type bands shifted by acetone do not restore completely to the original position by purging with N_2 , while the bands shifted by ammonia are repeatedly restored to the original state. To explain the discrepancy, one would have to presume the presence of a higher energy barrier for acetone, compared to ammonia, to adsorb/desorb onto/from Ag. Irrespective of this, when the Ag atom interacts with acetone, the net charge of the Ag atom was computed to be +0.034 e, while it was -0.143 e when interacting with ammonia. This suggests that acetone must act as an electron acceptor when interacting with Ag, while ammonia is acting as an electron donor when interacting with Ag. The SERS spectral variation in Figures 3(a) and (b) would then be associated with the surface potential of Ag nanoparticles varied by acetone or ammonia. Accordingly, this study subsequently took the potential-dependent SERS spectra of 4-ABT in an electrochemical environment.

Figures. 5(a), (b) and (c) show a series of potential-dependent SERS spectra of 4-ABT on Ag nanoparticles assembled on an ITO electrode, taken using 488, 514.5, and 632.8 nm radiation as the excitation sources, respectively. All the spectra were reversibly observed during the potential cycling between 0.0 and -1.2 V. The SERS spectral pattern was, however, affected not only by the electrode potential but also by the excitation wavelength.

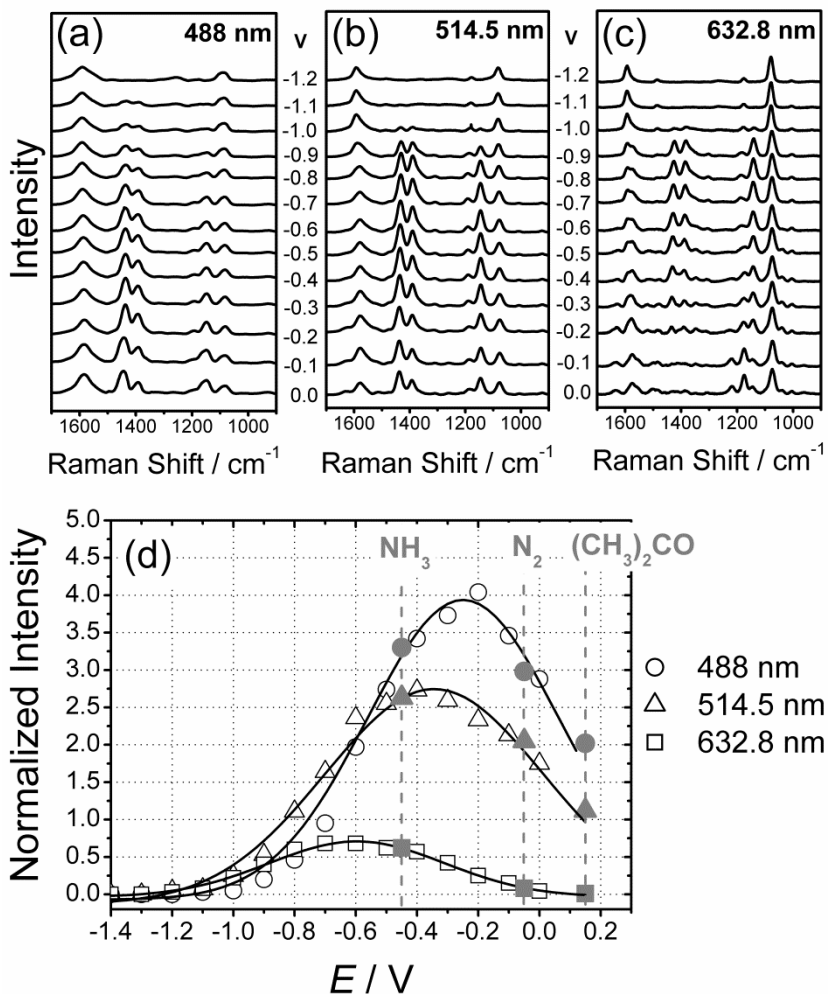


Figure 5. Potential-dependent SERS spectra of 4-ABT adsorbed on Ag nanoparticles on an ITO electrode, measured in 0.1 M NaClO₄ using (a) 488, (b) 514.5, and (c) 632.8 nm radiation as the excitation sources. (d) Relative intensities of ring 19b and 7a bands drawn against the electrode potential in (a)–(c). Three sets of normalized 19b intensities determined under the flow of acetone or nitrogen or ammonia are overlapped in (d), marking the regions of best overlap in dotted lines (see the filled circles, triangles, and squares).

This is evident from Figure 5(d), which shows the normalized peak intensity of the ring 19b band (a typical b₂-type band of 4-ABT) with respect to the 7a band (a

typical a_1 -type band), drawn versus the electrode potential at three different excitation wavelengths. The solid lines in Figure 5(d) represent the Gaussian fitting of the peak intensities. At higher excitation wavelengths, the peak maximum (E_{\max}) occurred at lower electrode potentials, specifically at -0.61, -0.31, and -0.14 V with the excitation at 632.8 (1.96), 514.5 (2.41), and 488 nm (2.54 eV), respectively. The $dE_{\max}/d(h\nu)$ slope, the slope of the peak maximum as a function of excitation energy, would then be approximately 0.8 V/eV. The positive slope of the curve and the fact that it is quite close to unity might be taken as evidence of the metal to molecule charge-transfer nature of the spectral intensities [18-21]. In principle, this accords with the presumption that the b_2 -type bands are associated with a chemical enhancement mechanism in SERS, similar to that claimed by Osawa et al. for 4-ABT adsorbed on Ag electrodes [20]. If the b_2 -type bands were due to a photoreaction product, the decrease in intensity shown in the right hand side of Figure 5(d) could not be understood, because it might then dictate the formation of a reduction product such as 4-ABT, during an anodic scan, from an oxidized species such as DMAB.

In the SERS spectra of 4-ABT on Ag measured under the flow of N_2 and shown in Figure 2(b), the 19b band intensity normalized with respect to that of the 7a band was determined to be 2.9, 2.1, and 0.25, corresponding to the excitation at 488, 514.5, and 632.8 nm, respectively. Conversely, in the spectra measured under the flow of acetone and ammonia and shown in Figures 3(a) and (b), respectively, the normalized 19b intensities were determined to be 2.1, 1.1, and 0.02 and 3.5, 2.6, and 0.62, respectively, corresponding to the excitation at 488, 514.5, and 632.8 nm,

respectively. An attempt was made to overlap each of these three sets of normalized intensities with the potential dependent data shown in Figure 5(d). For reference, the best overlaps are marked in dotted lines in Figure 5(d). Although the values do not lie exactly on the potential-dependent data, the effect of acetone can be regarded as corresponding to an application of +0.15 V to the Ag substrate *vs* a saturated Ag/AgCl electrode, while the effects of ammonia and nitrogen correspond, respectively, to the application of approximately -0.45 and -0.2 V to Ag. The SERS spectral variation of 4-ABT by VOCs can therefore be interpreted in terms of the surface potential change of Ag nanoparticles. Then, since the VOCs used in this study barely react chemically with 4-ABT or induce a reaction, the spectral variation observed in the presence of VOCs has nothing to do with any species (including DMAB) converted from 4-ABT, but is surely associated with the intrinsic character of 4-ABT.

Summary and Conclusion

This study have examined whether and how VOCs could affect the SERS spectral feature of 4-ABT on Ag. For that purpose, initially this work was prepared SERS-active Ag nanoparticle films by dropping 55 nm Ag particles onto a mica or ITO substrate. Subsequently, there are confirmed that more than three additional peaks appear distinctly in the SERS spectra, compared with the NR spectrum of 4-ABT. Recent debates have focused on whether their origin is due to either an Ag-to-4-ABT charge transfer or the formation of a photoreaction product such as DMAB. Interestingly, this study found that the peak intensity was very susceptible not only

to the excitation wavelength applied but also to the kind of VOCs to which the films were exposed. The effect of VOCs must be indirect because the VOCs used in this study, specifically acetone and ammonia, barely react directly with 4-ABT. A plausible explanation on the effect of VOCs would then be that the spectral variation observed is associated with the movement of electrons between VOCs and the Ag substrate. Supposedly, when electrons can flow from Ag to VOCs due to the electron accepting capability of VOCs, the surface potential of Ag nanoparticles will increase, but the surface potential of Ag must decrease when VOCs act as electron donor. These ideas were supported theoretically by a quantum mechanical calculation and further experimentally by the potential dependent SERS data. In the potential-dependent SERS measurement, the spectral peak intensities were, in fact, highly dependent on both the electrode potential and the excitation wavelength. On the other hand, acetone and ammonia were theoretically confirmed to function as an electron acceptor and an electron donor, respectively, thus being able to either increase or decrease the surface potential of Ag nanoparticles. Based on this evidence, the effect of acetone appeared to correspond to an application of +0.15 V to the Ag substrate vs a saturated Ag/AgCl electrode, while the effects of ammonia and even nitrogen corresponded, respectively, to the application of approximately -0.45 and -0.2 V to Ag. Explaining the effect of VOCs in this way, this study can finally conclude that the new peaks appearing in the SERS of 4-ABT have nothing to do with any surface-induced photoreaction product produced from 4-ABT, but they are intrinsically due to the b_2 type vibrations of 4-ABT, appearing in SERS spectra in association with the Ag-to-4-

ABT charge transfer phenomenon. A near reversible change in the peak intensity under the alternate flow of NH₃ and N₂ surely precludes the possibility of the formation of a photoreaction product. The excitation wavelength dependence has then to be understood similarly in terms of the charge-transfer mechanism operative in SERS.

References

1. Chern, J.-M.; Chou, S.-R. *Ind. Eng. Chem. Res.* **1999**, *38*, 3176.
2. Chiang, Y.-C.; Chiang P.-C.; Chang, E.-E. *J. Environ. Engineering* **2000**, *127*, 54.
3. Ruddy, E. N.; Carroll, L. N. *Chem. Engrg. Progress.* **1993**, 28.
4. St-Germain, F.; Mamer, O.; Brunet, J.; Vachon, B.; Tardif, R.; Abribat, T.; Des Rosiers, C.; Montgomery, J. *Anal. Chem.* **1995**, *67*, 4536.
5. Zhang, T.; Mubeen, S.; Myung, N. V.; Deshusses, M. A. *Nanotechnology* **2008**, *19*, 332001.
6. Bhatkhande, D. S.; Pangarkar, V. G.; Beenackers, A. *J. Chem. Technol. Biotechnol.* **2002**, *77*, 102.
7. Busca, G.; Berardinelli, S.; Resini, C.; Arrighi, L. *J. Hazard. Mater.* **2008**, *160*, 265.
8. Mudliar, S.; Giri, B.; Padoley, K.; Satpute, D.; Dixit, R.; Bhatt, P.; Pandey, R.; Juwarkar, A.; Vaidya, A. *J. Environ. Manage.* **2010**, *91*, 1039.

9. Kim, K.; Kim, K. L.; Shin, D.; Lee J. W.; Shin, K. S. *Chem. Comm.* **2010**, *46*, 3753.
10. Kim, K.; Kim, K. L.; Choi, J.-Y.; Shin, K. S. *Phys. Chem. Chem. Phys.* **2011**, *13*, 5981.
11. Shin, D.; Kim, K.; Shin, K. S. *Chem. Phys. Chem.* **2010**, *11*, 83.
12. Futamata, M. *J. Phys. Chem.* **1994**, *98*, 12702.
13. Park, W.; Kim, Z. H. *Nano Lett.* **2010**, *10*, 4040.
14. Kim, K.; Shin, D.; Lee H. B.; Shin, K. S. *Chem. Commun.* **2011**, *47*, 2020.
15. Uetsuki, K.; Verma, P.; Yano, T.; Saito, Y.; Ichimura, T.; Kawata, S. *J. Phys. Chem. C* **2010**, *114*, 7515.
16. Kim, N.-J. *J. Phys. Chem. C* **2010**, *114*, 13975.
17. Yoon, J. H.; Park, J. S.; Yoon, S. *Langmuir* **2009**, *25*, 12475.
18. Lombardi, J. R.; Birke, R. L. *Acc. Chem. Res.* **2009**, *42*, 734.
19. Lombardi, J. R.; Birke, R. L.; Lu, T.; Xu, J. *J. Chem. Phys.* **1986**, *84*, 4174.
20. Osawa, M.; Matsuda, N.; Yoshii, K.; Uchida, I. *J. Phys. Chem.* **1994**, *98*, 12702.
21. Lombardi, J. R.; Birke, R. L. *J. Phys. Chem. C* **2008**, *112*, 5605.
22. Cao, L.; Diao, P.; Tong, L.; Zhu, T.; Liu, Z. *Chem. Phys. Chem.* **2005**, *6*, 913.
23. Wu, D. Y.; Liu, X. M.; Huang, Y. F.; Ren, B.; Xu, X.; Tian, Z. Q. *J. Phys. Chem. C* **2009**, *113*, 18212.
24. Huang, Y. F.; Zhu, H. P.; Liu, G. K.; Wu, D. Y.; Ren, B.; Tian, Z. Q. *J. Am. Chem. Soc.* **2010**, *132*, 9244.
25. Kim, K.; Lee, H. B.; Yoon, J. K.; Shin, D.; Shin, K. S. *J. Phys. Chem. C* **2010**, *114*, 13589.

26. Yoon, J. K.; Kim, K.; Shin, K. S. *J. Phys. Chem. C* **2009**, *113*, 1769.
27. Kim, K.; Yoon, J. K. *J. Phys. Chem. B* **2005**, *109*, 20731.
28. Lee, P. C.; Meisel, D. *J. Phys. Chem.* **1982**, *86*, 3391.
29. Grabar, K. C.; Freeman, R. G.; Hommer, M. B.; Natan, M. J. *Anal. Chem.* **1995**, *67*, 735.
30. Moskovits, M. *Rev. Mod. Phys.* **1985**, *57*, 783.
31. Gaussian 03W (Revision C.01), Frisch, M. J.; Trucks, G. W.; Schlegel, H. B.; Scuseria, G. E.; Robb, M. A.; Cheeseman, J. R.; Zakrzewski, V. G.; Montgomery, J. A.; Stratmann, R. E.; Burant, J. C.; Dapprich, S.; Millam, J. M.; Daniels, A. D.; Kudin, K. N.; Strain, M. C.; Farkas, O.; Tomasi, J.; Barone, V.; Cossi, M.; Cammi, R.; Mennucci, B.; Pomelli, C.; Adamo, C.; Clifford, S.; Ochterski, J.; Petersson, G. A.; Ayala, P. Y.; Cui, Q.; Morokuma, K.; Malick, D. K.; Rabuck, A. D.; Raghavachari, K.; Foresman, J. B.; Cioslowski, J.; Ortiz, J. V.; Stefanov, B. B.; Liu, G.; Liashenko, A.; Piskorz, P.; Komaromi, I.; Gomperts, R.; Martin, R. L.; Fox, D. J.; Keith, T.; Al-Laham, M. A.; Peng, C. Y.; Nanayakkara, A.; Gonzalez, C.; Challacombe, M.; Gill, P. M. W.; Johnson, B. G.; Chen, W.; Wong, M. W.; Andres, J. L.; Head-Gordon, M.; Replogle, E. S.; Pople, J. A. Gaussian, Inc. Wallingford, CT, **2004**.

Chapter 4

SERS of 4-ABT And 4,4'-
dimercaptoazobenzene (4,4'-DMAB) on Ag
and Au: pH Dependence of b_2 -Type Bands

4. SERS of 4-ABT And 4,4'-dimercaptoazobenzene (4,4'-DMAB) on Ag and Au: pH Dependence of b₂-Type Bands

Introduction

The b₂-type bands were assigned in SERS signal of 4-ABT on Ag system, and their strong appearance was interpreted by Osawa et al. as the signature of an intensity borrowing from an intense $\pi \rightarrow \pi^*$ molecular transition ($^1A_1 \rightarrow ^1B_2$) at 300 nm [1]. For over a decade, 4-ABT has thus been regarded as a model compound for studying the charge-transfer (CT) chemical enhancement mechanism in SERS. In line with this, Lombardi and Birke explained the SERS spectrum of 4-ABT using only the Herzberg-Teller surface selection rules [2]. Very recently, however, a number of researchers have come up with a different explanation for the appearance of these b₂-type bands. The most extreme explanation is that the bands assigned to b₂ symmetry by Osawa et al. are not due to 4-ABT after all but due to the a_g modes of 4,4'-dimercaptoazobenzene (4,4'-DMAB) supposedly produced from 4-ABT via a catalytic coupling reaction on metal substrates [3]. However, according to the recent report [4], the appearance of the b₂-type bands is a general phenomenon in the SERS of 4-aminobenzenethiol analogs. This was mostly because, in the SERS spectra of 4-(diethylamino)benzenethiol (4-DEABT) and 4-(benzylideneamino)benzenethiol (4-BABT), the C–H stretching bands due to

two C_2H_5 groups in 4-DEABT and the $N=C$ stretching band due to the benzylidenamino group in 4-BABT were distinctly observed along with b_2 -type bands, indicating that the b_2 -type bands had nothing to do with any bond scission reaction of the amino group. Nonetheless, a separate preliminary work has shown that the intensity of the b_2 -type bands for some 4-ABT analogs was also affected by the solution pH. In fact, Hill et al. first reported that the b_2 -type bands of 4-ABT on roughed Au and Ag film in the SERS spectra not only strongly depend on the pH of a surrounding solution but also on the electrostatic potential applied [5]. According to those result, they were supposed that the binding interaction with positively charged electrode may result in the benzenoid form of adsorbed 4-ABT tautomerizing to the quinoid one so that the relative SERS intensities change significantly. On the other hand, Zong et al. also reported that the b_2 -type bands are absent in the SERS of 4-ABT on Au at acidic pH, but they appear distinctly at basic pH [6]. The appearance of the b_2 -type bands at basic pH was attributed to the conversion of 4-ABT to 4,4'-DMAB on Au as reported by Tian [3]. The intensity of the b_2 -type bands was used in assigning the pH values of intact cells. Therefore, in this work is demonstrated that the pH dependence of the b_2 -type bands in the SERS of 4-ABT has nothing to do with the conversion of 4-ABT to 4,4'-DMAB. The SERS of 4,4'-DMAB itself is not subject to change upon the variation of pH. The absence of the b_2 -type bands in the SERS of 4-ABT at acidic pHs is associated with the protonation of the amine group, thereby the highest occupied molecular orbital (HOMO)-to-lowest unoccupied molecular orbital (LUMO) gap becomes a

blue-shift, hindering the occurrence of the CT associated with the chemical enhancement mechanism in SERS.

Results and Discussion

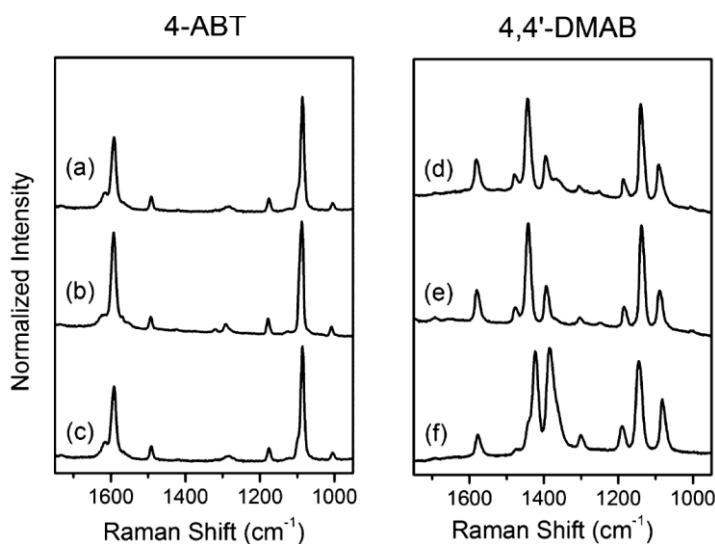


Figure 1. NR spectra of 4-ABT (a) in neat solid state and aqueous solution at pH (b) 3 and (c) 10. NR spectra of 4,4'-DMAB (d) in neat solid state and aqueous solution at pH (e) 4 and (d) 10.

Figure 1(a) shows the NR spectrum of 4-ABT in its neat solid state. As is already well known, only a few peaks that can be attributed to a_1 -type vibrations are exclusively identified [1]. The region of $1100\text{-}1500\text{ cm}^{-1}$, in which the b_2 -type bands are expected to appear, is mostly featureless. Figures 1(b) and (c) show the NR spectra of aqueous 4-ABT solutions at pH 3 and 10, respectively; due to a solubility problem, it was difficult to measure the NR spectra at pHs lower than 3. In general, the NR spectral pattern of 4-ABT is insensitive to the pH variation. Even though the NH_2 group of 4-ABT might be protonated at lower pHs, not only

the N–H stretching region around 3200 cm^{-1} but also the ring breathing and deformation regions around 1600 and 1000 cm^{-1} , respectively, were barely different at pH 3 and 10. Their NR spectral pattern is also much the same as that in the neat solid state. For a comparative study, this work was also measured the NR spectra of 4,4'-DMAB not only in its neat solid state but also in the dissolved state at pH 4 and 10, as shown in Figures 1(d) ~ (f), respectively. The first observation is that the a_g -type bands including the N=N stretching band appear distinctly in all NR spectra of 4,4'-DMAB [3]. The second observation is that the spectral pattern at pH 4 is nearly the same as that in the neat solid state, but it differs noticeably from that at pH 10. For instance, the N=N stretching peak appears at 1422 cm^{-1} at pH 10, while it is seen at 1442 cm^{-1} at pH 4. The deprotonation of the S–H groups must have resulted in a weakening of the N=N bond, probably suggesting that thioquinone type anions were formed at basic pHs. The NR spectral pattern of 4-ABT is, therefore, completely different from that of 4,4'-DMAB. SERS-active Ag or Au films were assembled onto the inside surface of a glass capillary modified earlier with 3-APS.

According to the TEM analyses shown in Figure 2(a), both the Au and Ag nanoparticles were mostly spherical with an average diameter of 23 ± 5 and 25 ± 13 nm, respectively. In the as-prepared state, the surface plasmon absorption bands were identified distinctly at 518 and 416 nm, respectively, in the UV-vis spectra, as shown in Figure 2(b). When Au and/or Ag nanoparticles were assembled onto an APS-modified glass substrate, the UV-vis absorption bands of metal nanoparticles were strongly red-shifted and broadened [7,8], as shown in Figure 2(c).

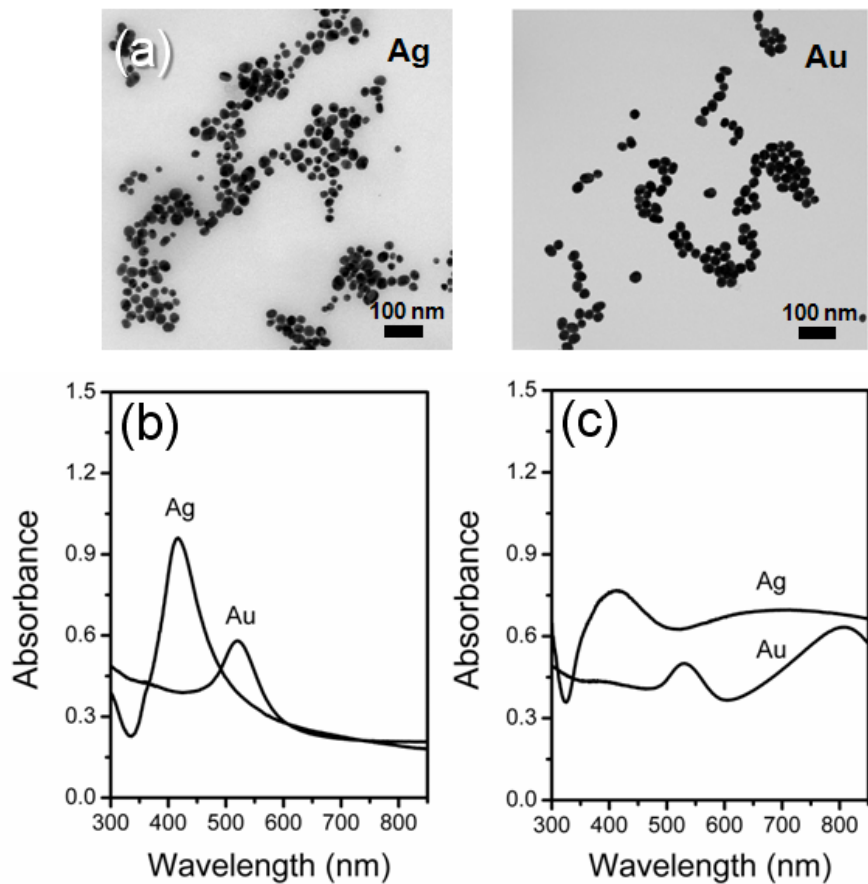


Figure 2. (a) TEM images and (b) UV-vis spectra of Au and Ag nanoparticles in as-prepared state. (c) UV-vis spectra of Au and Ag nanoparticles films assembled on 3-APS-modified glass substrates.

The Ag-coated film becomes then highly SERS active not only with the excitation at 514.5 nm but also with the excitation at 632.8 nm, while the Au-coated film is active only with the excitation at 632.8 nm. The SERS spectral feature of 4-ABT is dependent not only on the kinds of SERS substrates but also on the measurement conditions.

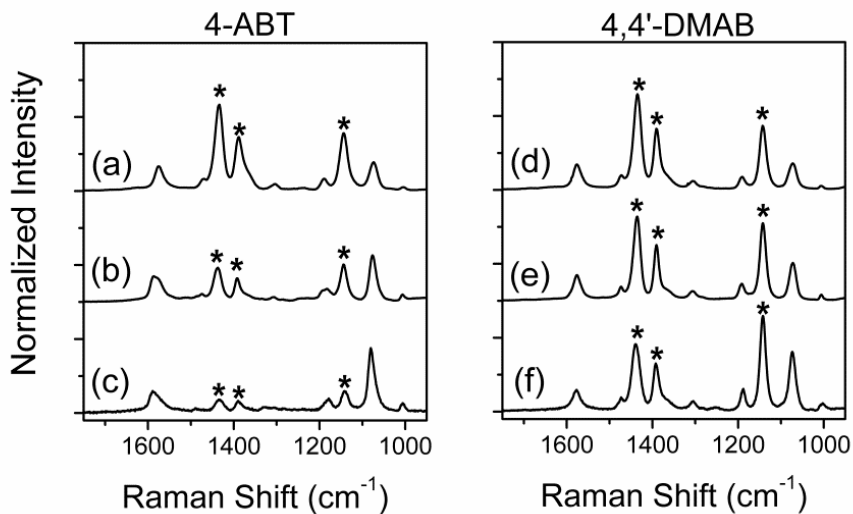


Figure 3. SERS spectra of 4-ABT on Ag measured in ambient conditions in air using (a) 514.5 and (b) 632.8 nm radiation as the excitation source, and (c) SERS spectrum of 4-ABT on Au taken under similar condition at 632.8 nm. SERS spectra of 4,4'-DMAB on Ag measured in ambient conditions in air using (d) 514.5 and (e) 632.8 nm radiation as excitation source, and (f) SERS spectrum of 4,4'-DMAB on Au taken under similar conditions at 632.8 nm.

Figures 3(a) and (b) show the SERS spectra of 4-ABT on Ag measured in ambient conditions using the 514.5 and 632.8 nm radiation as the excitation source, respectively. In contrast to the NR spectrum in Figure 1(a), the b_2 -type bands are distinctly observed in both SERS spectra (see the peaks marked with stars), although being less intense with the excitation at 632.8 nm. Figure 3(c) shows the SERS spectrum of 4-ABT, but this time adsorbed on Au, taken under similar conditions with the excitation at 632.8 nm. The b_2 -type bands are still observed, but very weakly in this case. As such, the intensities of the b_2 -type bands clearly depend on the kind of metallic substrate.

For comparison, Figures 3(d) and 3(e) show the SERS spectra of 4,4'-DMAB on Ag taken in similar conditions with the excitations at 514.5 and 632.8 nm, respectively. The SERS spectrum of 4,4'-DMAB on Au taken with the excitation at 632.8 nm is also shown in Figure 3(f). In contrast to 4-ABT, the SERS spectral feature of 4,4'-DMAB has virtually no dependence on the excitation wavelength nor on the kind of metal substrate. In addition, several a_g bands, including the N=N stretching band at $\sim 1440\text{ cm}^{-1}$, that are quite similar to the b_2 -type bands in the SERS of 4-ABT, are distinctly observed, not only in the NR spectrum but also in the SERS spectra (see the peaks marked with stars). At any rate, it is remarkable that the SERS spectral feature of 4-ABT on Ag, especially taken at 514.5 nm excitation, is nearly the same as that of 4,4'-DMAB, as reported by Huang et al. [3]: this work thus temporarily calls the a_g -bands of 4,4'-DMAB the same as the “ b_2 -type a_g ” bands. Due to such resemblance, 4-ABT was assumed by them to convert to 4,4'-DMAB via a surface-induced photoreaction [3]. If the b_2 -type bands in the SERS of 4-ABT are due to 4,4'-DMAB, the surface-induced photoreaction must be less favorable on Au than on Ag and less with the excitation at 632.8 nm than at 514.5 nm [9]. It is clearly noticed that the SERS spectral pattern of 4-ABT is highly dependent not only on the excitation wavelength but also on the kind of metal substrate. The present results subsequently confirmed that the SERS spectral pattern of 4-ABT is also dependent on the solution pH although the NR spectral pattern is insensitive to pH. Figure 4(a) shows the SERS spectra of 4-ABT on Ag taken at pH 10 and pH 2 using the 514.5 nm radiation as the excitation source. The b_2 -type bands appear more distinctly at pH 10 than at pH 2. This is also noticed that

the b_2 -type bands at pH 10 in Figure 4(a) are stronger than those measured in ambient conditions shown in Figure 3(a). Figure 4(b) shows the SERS spectra of 4-ABT on Ag taken at pH 10 and pH 2, but using the 632.8 nm radiation as the excitation source. Once again, the b_2 -type bands at pH 10 are much stronger than those measured in ambient conditions (Figure 3(b)). At pH 2, the b_2 -type bands are observed very weakly. A similar trend is observed using Au as the SERS substrate. Figure 4(c) shows the SERS spectra of 4-ABT on Au taken at pH 10 and pH 2 using the 632.8 nm radiation as the excitation source. The b_2 -type bands at pH 10 are once again stronger than those measured in ambient conditions (Figure 3(c)).

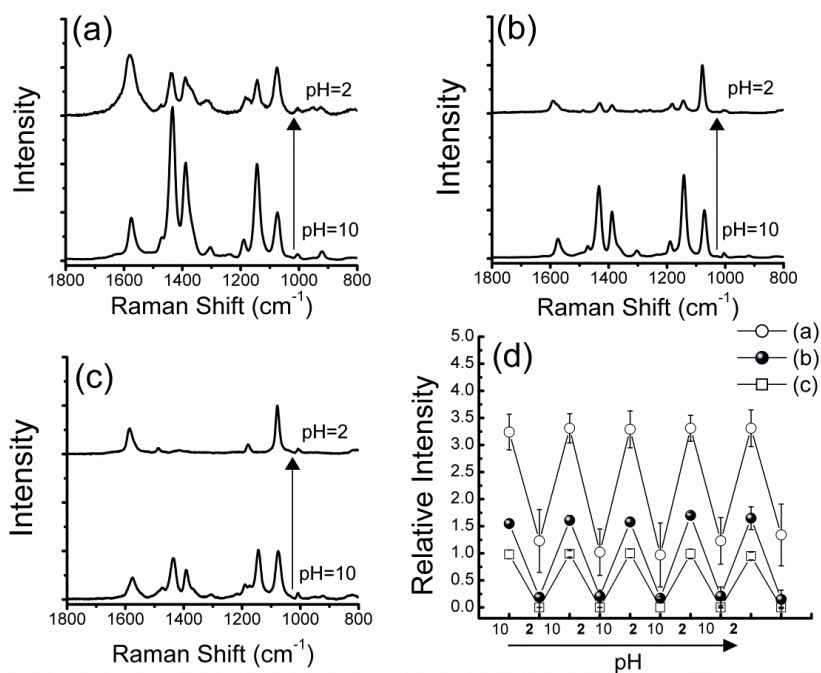


Figure 4. SERS spectra of 4-ABT on Ag taken at pH 10 and 2 using (a) 514.5 (b) 632.8 nm radiation as the excitation source. (c) SERS spectra of 4-ABT on Au taken at pH 10 and 2 using 632.8 nm radiation as the excitation source. (d) Relative intensity of a typical b_2 -type band at ~ 1437 cm⁻¹ (19b) and an a_1 band at ~ 1076 cm⁻¹ (7a) measured following repeated changes in the solution pH between 10 and 2.

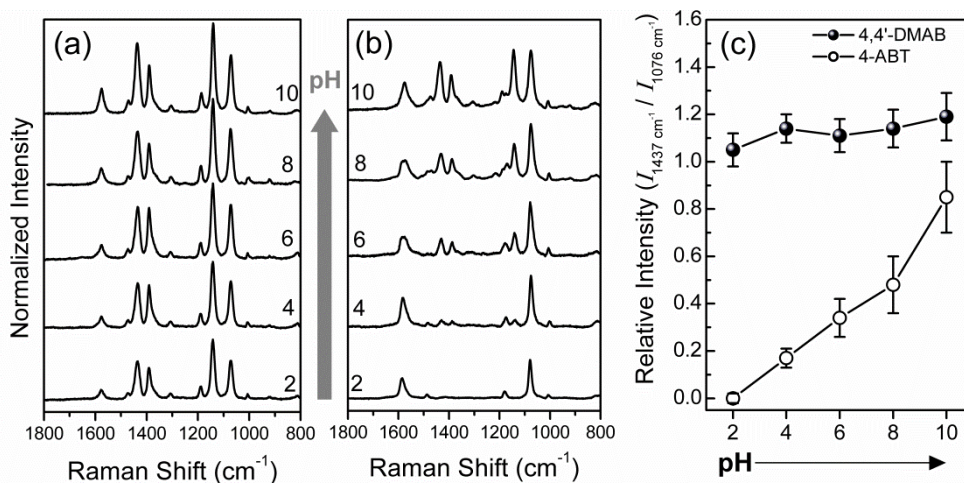


Figure 5. SERS spectra of (a) 4,4'-DMAB and (b) 4-ABT on Au measured as a function of solution pH using 632.8 nm radiation as the excitation source. (c) Relative intensity of the band at $\sim 1437 \text{ cm}^{-1}$ and the band at 1076 cm^{-1} , drawn versus the solution pH for both spectra in (a) and (b).

The b_2 -type bands were hardly detected at pH 2. All these pH dependencies of the SERS spectral pattern of 4-ABT were reversibly observed, following the repeated changes in the solution pH between 10 and 2, as illustrated in Figure 4(d). This reversibility strongly suggests that the appearance of the b_2 -type bands in the SERS of 4-ABT has nothing to do with any surface-induced photoreaction of 4-ABT.

For a comparative study, this work also measured the SERS spectra of 4,4'-DMAB on Au as a function of the solution pH, as shown in Figure 5(a). The SERS spectra of 4-ABT on Au measured similarly as a function of the solution pH are reproduced in Figure 5(b). It is seen that the SERS spectral pattern of 4,4'-DMAB is barely affected by the solution pH, although the NR spectral pattern is very susceptible to pH (see Figures 1(d) and (f)). The SERS spectra shown in Figure 5(a) are also mostly the same as those measured in ambient conditions shown in Figures

3(d) ~ (f). The b_2 -type a_g bands are observed at all pHs in the SERS of 4,4'-DMAB. However, in the SERS of 4-ABT in Figure 5(b), the b_2 -type bands are almost absent at pH 2, but they grow in intensity upon the increase in the solution pH, attaining a maximum at pH 10. This can be seen more clearly in Figure 5(c) in which is shown the relative peak intensity of the band at $\sim 1437\text{ cm}^{-1}$ and the band at $\sim 1076\text{ cm}^{-1}$ drawn versus the solution pH for both the SERS spectra of 4-ABT and 4,4'-DMAB. As mentioned above, the changes in the relative peak intensities in the SERS of 4-ABT were reversible against the repeated pH variation. The invariance of the SERS of 4,4'-DMAB against the pH variation contrasts obviously with what has been observed for 4-ABT. The question is then how we can rationalize the pH dependence of the SERS of 4-ABT. If the b_2 -type bands in the SERS of 4-ABT were due to a photoreaction product including 4,4'-DMAB, there would be no reason for them to disappear at lower pHs since the photoreaction could not be pH-reversible in any sense. Presumably, the absence of a weak feature of the b_2 -type bands at pH 2 would then be associated with the protonation of the amine group, hindering the involvement of the chemical enhancement mechanism. According to a preliminary density functional theory (DFT) calculation, the LUMO-HOMO energy gap of HS-C₆H₄-NH₃Cl is greater by 0.32 eV than that of 4-ABT. This suggests that the LUMO energy level is very sensitive to the electronic charge of the amine nitrogen atom [4]. This work thus was attempted to measure the UV-vis spectra of 4-ABT at various solution pHs. As shown in Figure 6, the absorption bands observed around 260 and 300 nm are seen to blue-shift as the solution pH is decreased, in agreement with the ab initio quantum mechanical

calculation.

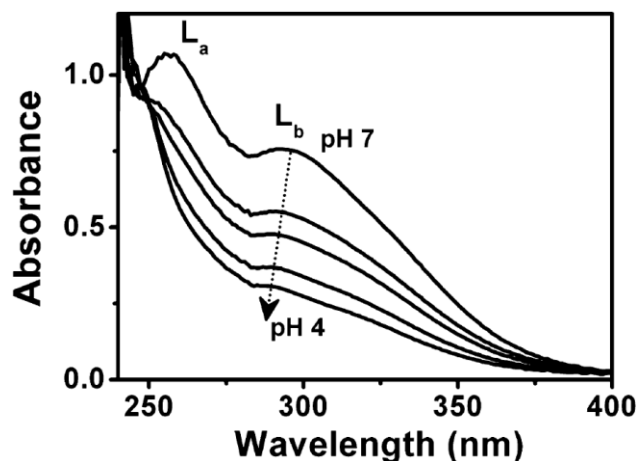


Figure 6. UV-vis spectra of 4-ABT at various solution pHs.

The bands around 260 and 300 nm can be assigned to L_a and L_b with Platt's notation, respectively, and are actually symmetry-forbidden for benzene, but substituents on the benzene ring lower the symmetry and introduce some allowed character into the symmetry-forbidden transitions [1,2]. It is noteworthy that the UV-vis absorption band of 4-ABT at acidic pH resembles to some extent that of para-substituted (but not amino) benzenethiol derivatives such as 4-(methyl)benzenethiol (4-MBT), 4-mercaptophenol (4-MP), 4-(fluoro)benzenethiol (4-FBT), 1,4-benzenedithiol (1,4-BDT), and 4-(chloro)benzenethiol (4-CBT). According to the recent report [4], there were also found that the b_2 -type bands are also observed in the SERS spectra of multiple 4-ABT derivatives including 4-DEABT, 4-BABT, 4-(acetamido)benzenethiol (4-AABT), 4-(dimethylamino)benzenethiol (4-DMABT), and 4-(azido)benzenethiol (4-AZBT). In contrast to this, no such b_2 -type bands were observed at all in the SERS spectra

of para-substituted (but not amino) benzenethiol derivatives such as 4-MBT, 4-MP, 4-FBT, 1,4-BDT, and 4-CBT. The difference between 4-ABT derivatives and para-substituted (but not amino) benzenethiol derivatives appears to be associated with the LUMO-HOMO energy gap [4]. According to *ab initio* DFT calculation, the LUMO-HOMO energy gap for (non-amino) para-substituted benzenethiols was ~1 eV greater than that for 4-ABT derivatives, in agreement with the UV-vis spectra. In particular, the energy gap computed for 4-ABT derivatives (~300 nm) was consonant with the interpretation of Osawa et al., that the appearance of the b_2 -type bands in the SERS spectrum of 4-ABT is associated with an intensity borrowing from an intense $\pi \rightarrow \pi^*$ molecular transition (${}^1A_1 \rightarrow {}^1B_2$) at 300 nm [1]. The disappearance or substantial weakening of the b_2 -type bands at acidic pHs in the SERS of 4-ABT can then be attributed to the shift of the LUMO to higher energies caused by the protonation of the amine group. The importance of LUMO levels in SERS has also been emphasized in the recent time-dependent DFT study of Morten and Jensen on pyridine derivatives, in which the magnitude of chemical enhancement was governed to a large extent by the LUMO of the molecules, as well as the HOMO of the metal substrates [10]. Hence, we must conclude that the b_2 -type bands observable in the SERS spectrum of 4-ABT have nothing to do with any surface-induced photoreaction, but are simply, due to an intrinsic characteristic of 4-ABT derivatives, associated with the CT chemical enhancement mechanism in SERS.

Summary and Conclusion

As one of several attempts to explore the origin of the b_2 -type bands observable in the SERS of 4-ABT, this work has minutely described for their pH dependence, coupled with using different SERS substrates and excitation wavelengths. Consulting the recent claim that those b_2 -type bands might be associated with a surface-induced photoreaction product such as 4,4'-DMAB, this work also examined the pH dependence of the SERS spectral feature of 4,4'-DMAB. Regarding, first, the NR spectra, there was no pH dependence for 4-ABT, but there was for 4,4'-DMAB. In all NR spectra of 4-ABT, only a_1 -type bands were exclusively observed with a comparable spectral pattern. In contrast, the NR spectrum of 4,4'-DMAB at pH 10 was noticeably different from that at pH 4. The N=N stretching band had red-shifted by as much as 20 cm^{-1} at pH 10, suggesting that thioquinone type anions were formed at basic pHs. Distinct differences were observed even in the SERS spectra of 4-ABT and 4,4'-DMAB. The SERS spectral feature of 4,4'-DMAB had virtually no dependence either on the excitation wavelength or on the kind of metal substrate or even on the solution pH. Several bands including the N=N stretching band similar to the b_2 -type bands in the SERS of 4-ABT were clearly observed in all conditions. However, the SERS spectral pattern of 4-ABT displayed substantial changes, depending not only on the excitation wavelength and the kind of SERS substrates but also on the solution pH. The b_2 -type bands were the most intensely observed when 4-ABT adsorbed on Ag was irradiated with a laser light at 514.5 nm at pH 10, more than in ambient conditions. At acidic pHs, however, the b_2 -type bands of 4-ABT were faintly

observed. The pH dependence was reversible, indicating that the appearance and disappearance of the b_2 -type bands had nothing to do with the formation of any surface-induced photoreaction product like 4,4'-DMAB. The b_2 -type bands observable in the SERS of 4-ABT were thus concluded to be an intrinsic characteristic of 4-ABT, mostly associated with the chemical enhancement mechanism in SERS. It is presumed that when the amine group is protonated at acidic pHs, the electron population in the benzene ring moiety decreases, resulting in the up-shift of the LUMO level of 4-ABT, as revealed by UV-vis spectra and from an ab initio calculation, thereby prohibiting the charge transfer resonance chemical enhancement.

References

1. Osawa, M.; Matsuda, N.; Yoshii, K.; Uchida, I. *J. Phys. Chem.* **1994**, *98*, 12702.
2. Lombardi, J. R.; Birke, R. L. *Acc. Chem. Res.* **2009**, *42*, 734.
3. Huang, Y. F.; Zhu, H. P.; Liu, G. K.; Wu, D. Y.; Ren, B.; Tian, Z. Q. *J. Am. Chem. Soc.* **2010**, *132*, 9244.
4. Kim, K.; Shin, D.; Choi, J.-Y.; Kim, K. L.; Shin, K. S. *J. Phys. Chem. C* **2011**, *115*, 24960.
5. Hill, W.; Wehling, B. *J. Phys. Chem.* **1993**, *97*, 9451.
6. Zong, S.; Wang, Z.; Yang, J.; Cui, Y. *Anal. Chem.* **2011**, *83*, 4178.
7. Grabar, K. C.; Freeman, R. G.; Hommer, M. B.; Natan, M. J. *Anal. Chem.* **1995**, *67*, 735.
8. Freeman, R. G.; Grabar, K. C.; Allison, K. J.; Bright, R. M.; Davis, J. A.; Guthrie,

A. P.; Hommer, M. B.; Jackson, M. A.; Smith, P. C.; Walter, D. G.; et al.
Science **1995**, *267*, 1629.

9. Kim, K. L.; Lee, S. J.; Kim, K. *J. Phys. Chem. B* **2004**, *108*, 9216.

10. Morton, S.; Jensen, L. *J. Am. Chem. Soc.* **2009**, *131*, 4090.

Chapter. 5

Similarity and Dissimilarity in SERS of 4- ABT and Its Analog molecules

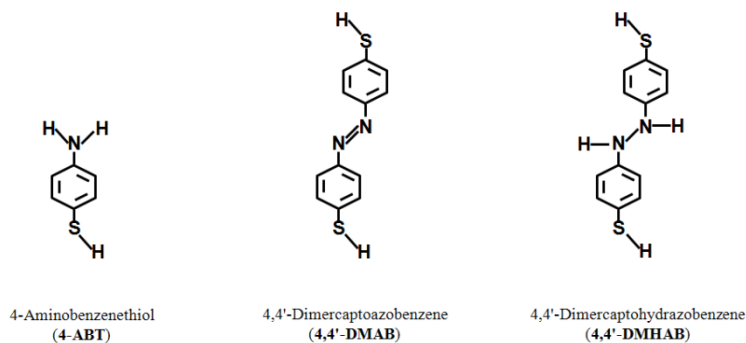
5-1. Similarity and Dissimilarity in SERS of 4-ABT, 4,4'-DMAB and 4,4'-Dimercaptopyridazobenzene (4,4'-DMHAB) on Ag

Introduction

Two enhancement mechanisms in SERS phenomenon, one called a long-range electromagnetic (EM) effect and the other called a short-range chemical effect, are simultaneously operative [1]. Both mechanisms also suggest the possibility of enhanced absorption and enhanced photochemistry for surface-adsorbed molecules [2-10]. In light of this, 4,4'-DMAB has recently come to researchers attention since its SERS spectral feature is remarkably similar to that of 4-ABT, especially in Ag nanoaggregates [11-26]. 4-ABT itself is an unusual molecule in the sense that its SERS spectral feature is dependent not only on the nature of the SERS substrate but also on the measurement conditions [11-26]. In the normal Raman (NR) spectrum, only peaks assignable to totally symmetric (a_1) vibrations are exclusively observed, but in the SERS spectrum, non- a_1 type peaks are usually additionally identified [27]. The origin of these additional bands is not clearly known. One claim is that those bands are due to the b_2 -type bands of 4-ABT arising from the charge transfer chemical enhancement mechanism [27]. Another claim is that those bands must arise from the N=N stretching vibrations of 4,4'-DMAB produced from 4-ABT via a catalytic coupling reaction on metal substrates [11]. The basis for this

claim is the spectral similarity of 4-ABT and 4,4'-DMAB. Even though there is a wealth of SERS data on 4-ABT in the literature [11-26], only limited data is available on 4,4'-DMAB [11,17], hindering the exploration of the origin of the similarity in the SERS of 4-ABT and 4,4'-DMAB. The lack of data for 4,4'-DMAB is partly due to the fact it has to be custom synthesized [17,23].

As noted in section 3, the appearance of the b_2 -type bands is a general phenomenon in the SERS of 4-ABT analogs [28]. The appearance of the b_2 -type bands in SERS spectra seems thus to be a common feature of 4-ABT derivatives possibly including 4,4'-DMAB. 4,4'-Dimercaptohydrazobenzene (4,4'-DMHAB) is an important derivative of 4-ABT in the sense that it may be converted either into 4-ABT by reduction or into 4,4'-DMAB by oxidation (See scheme 2). This type of conversion is possible because its central moiety, hydrazobenzene ($C_6H_5NHNHC_6H_5$), can be converted into aniline by reduction or into azobenzene by oxidation and even into benzidine by rearrangement in the presence of hydrochloric acid [29]. Supposedly then, the SERS characteristics of 4,4'-DMHAB would resemble those of 4-ABT under one set of conditions but those of 4,4'-DMAB under other conditions. Bearing this in mind, this section will be reported to carefully analyze the SERS spectra of 4-ABT, 4,4'-DMAB, and 4,4'-DMHAB on Ag.



Scheme 2. Structure formula of 4-ABT, 4,4'-DMAB, and 4,4'-DMHAB

Firstly present results confirmed that the SERS spectral patterns of 4,4'-DMAB and 4,4'-DMHAB on Ag measured under ambient conditions were in fact quite similar to that of 4-ABT on Ag, whereas the normal Raman spectral patterns are clearly dissimilar to one another. Naturally then a reasonable assumption would have been that the three SERS spectra were all derived from a common species that might be either 4-ABT or 4,4'-DMAB or 4,4'-DMHAB. A more detailed spectral analysis led us to conclude, however, that those three molecules were not subjected to any photoreaction by the irradiation of a visible laser; though 4,4'-DMAB would be converted to 4-ABT by an electrochemical reduction, the reverse is not true, at least in the potential region of 0.0 and -1.2 V vs a saturated Ag/AgCl electrode. This work clearly supports our previous proposition that the appearance of the b_2 -type bands in SERS spectra is a common feature of 4-ABT derivatives including 4,4'-DMAB and 4,4'-DMHAB, and it must therefore be associated with the chemical enhancement mechanism in SERS [17,28], coupled with an appropriate energy gap between the lowest unoccupied molecular orbital and the highest occupied molecular orbital [31].

Results and Discussion

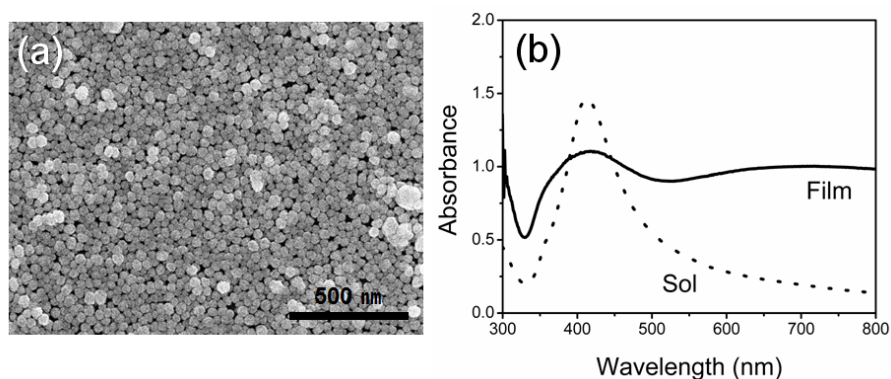


Figure 1. (a) TEM image of Ag nanoparticle film. (b) UV–vis extinction spectra of Ag nanoparticles in the colloidal state (dot line) and in the film state (solid line).

Figure 1(a) shows the FE-SEM image of Ag nanoparticles prepared in this work. They are mostly faceted spherical particles with a mean diameter of 55 ± 16 nm. The isolated Ag nanoparticles exhibit the surface plasmon resonance (SPR) absorption band at 412 nm, as can be seen in Figure 1(b). These colloidal Ag nanoparticles could be assembled into a close-packed aggregate, as shown in Figure 1(a), by adsorption onto a 3-APS modified glass substrate. Due to the stronger interparticle interaction, the SPR band is broadened into the visible and near infrared region, as can be seen in Figure 1(b). According to the electromagnetic enhancement mechanism, the Ag nanoparticle film must be highly SERS active, not only with the excitation at 488 nm but also with the excitation at 632.8 nm, both of which are used in this work [1].

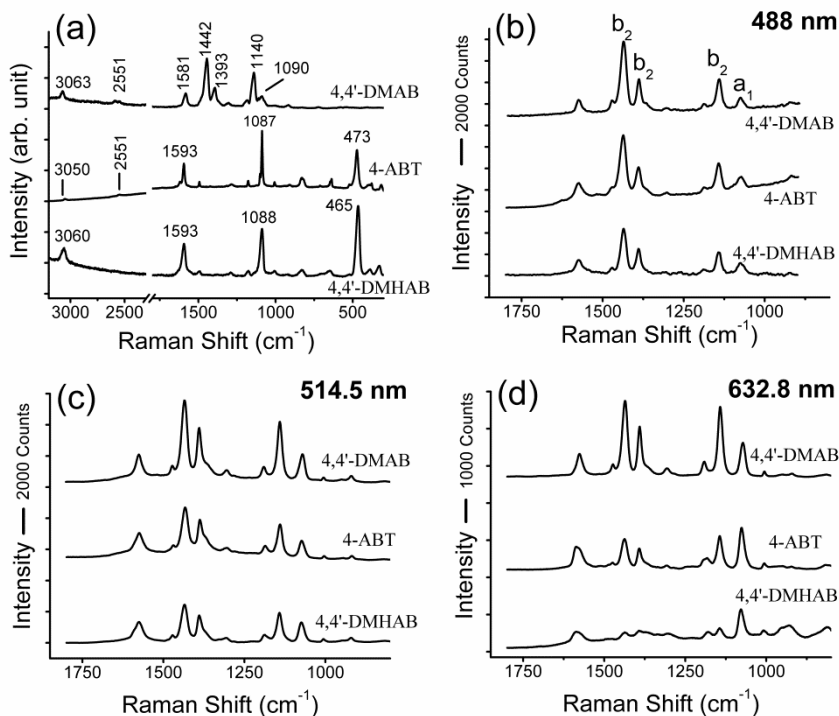


Figure 2. (a) NR spectra of 4,4'-DMAB, 4-ABT, and 4,4'-DMHAB in the neat state taken using 488 nm radiation as the excitation source. SERS spectra of 4,4'-DMAB, 4-ABT, and 4,4'-DMHAB on Ag taken under ambient conditions using (b) 488, (c) 514.5, and (d) 632.8 nm radiation as the excitation sources.

Figure 2(a) shows the NR spectra of 4,4'-DMAB, 4-ABT, and 4,4'-DMHAB in their neat state, taken using 488 nm radiation as the excitation source. Although not shown, their spectral pattern was insensitive to the excitation wavelength. As is already well known, the spectral region between 1100 and 1500 cm^{-1} is almost featureless in the NR spectra of 4-ABT and 4,4'-DMHAB. In contrast, very intense peaks are identified in that region in the NR spectrum of 4,4'-DMAB. These bands, such as that at 1442 cm^{-1} , can be attributed at least partly to the stretching motion of the N=N bond [11,17]. Figures 2(b) ~ (d) show the SERS spectra of 4,4'-DMAB,

4-ABT, and 4,4'-DMHAB on Ag taken under ambient conditions using 488, 514.5, and 632.8 nm radiation as the excitation sources, respectively. All the peak intensities are normalized with respect to that of a silicon wafer at 520 cm^{-1} measured at each excitation wavelength. In contrast to the NR spectra, the SERS spectral pattern looks insensitive to the molecules. Several very intense peaks are identified even in the region of 1100 and 1500 cm^{-1} in the SERS spectra of 4-ABT and 4,4'-DMHAB, as in that of 4,4'-DMAB. That was the reason why a few researchers claimed that 4-ABT on Ag must have converted to 4,4'-DMAB by a photoinduced coupling reaction [11-16]. Conversely, Kim et al. claimed recently that the appearance of those bands in the SERS of 4-ABT had nothing to do with any surface-induced photoreaction, but were a phenomenon common to all 4-ABT derivatives, including 4-DEABT and 4-BABT, associated with the chemical enhancement mechanism in SERS [28]. Although the SERS spectral patterns of 4,4'-DMAB, 4-ABT, and 4,4'-DMHAB in Figures 2(b) ~ (d) look similar to one another, there are obvious differences. The peak at $\sim 1072\text{ cm}^{-1}$ in the SERS of 4-ABT in Figure 2(b) can be assigned to the a_1 -type 7a band, whose counterpart appears at 1087 cm^{-1} in the NR spectrum in Figure 2(a). A similar band is observed also in the SERS spectrum of 4,4'-DMAB, as well as in that of 4,4'-DMHAB. This band might be assumed to be a 7a analog-mode: For an easy comparison of the SERS spectra of 4,4'-DMAB, 4-ABT, and 4,4'-DMHAB, the present work presumes (for a while) the SERS peaks of 4,4'-DMAB and 4,4'-DMHAB appearing at similar positions to be of the same types as those of 4-ABT.

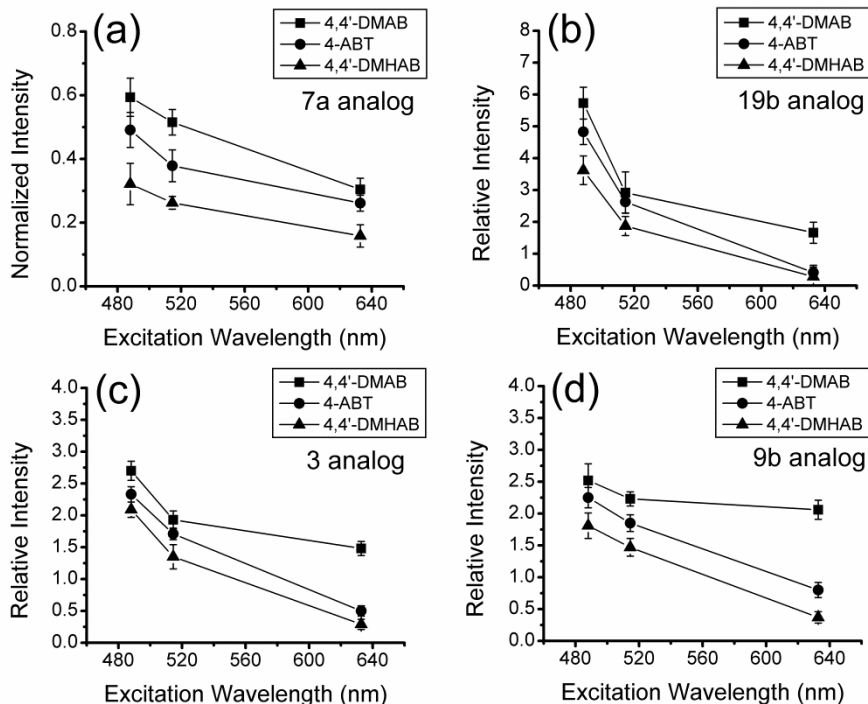


Figure 3. (a) Normalized peak intensities of 7a analogue-bands in Figure 2(b) ~ (d) drawn versus the excitation wavelength. Intensities of (b) 19b, (c) 3, and (d) 9b analogue-bands with respect to that of the 7a analogue-band in Figure 2(b) ~ (d) drawn versus the excitation wavelength.

On this basis, Figure 3(a) shows the intensities of these a_1 -analogue bands in Figures 2(b) ~ (d) drawn versus the excitation wavelength. For all molecules, the a_1 -analogue band became intensified with excitation at lower wavelengths. The patterns of intensity variation are similar to one another, but the intensity is obviously larger at all excitation wavelengths in the order of 4,4'-DMAB > 4-ABT > 4,4'-DMHAB. This may be indicative of the presence of three different molecules on Ag, implying also that 4-ABT has not converted to 4,4'-DMAB as claimed by Kim et al. [28]. According to a separate SERS measurement of benzenethiol (BT), the SERS

activity of our Ag film at 632.8 nm excitation was 33% higher than that at 488 nm excitation. This observation is consonant with the UV-vis measurement; the SPR absorbance of the Ag nanoparticle film at 632.8 nm (1.0) is higher than that at 488 nm (0.9) as shown in Figure 1(d). Presuming that the SERS of BT is mostly due to electromagnetic enhancement, the opposite excitation wavelength dependence in Figure 3(a) suggests that the 7a band of 4-ABT, as well as their analogs of 4,4'-DMAB and 4,4'-DMHAB, must be subjected to not only electromagnetic enhancement but also chemical enhancement [35].

Assuming that 4-ABT on Ag was not subjected to any photoreaction, the peaks appearing at 1435, 1388, and 1141 cm^{-1} in its SERS spectra in Figures 2(b) ~ (d) had to be assigned to the b_2 -type 19b, 3, and 9b modes, respectively. Once again, the SERS peaks of 4,4'-DMAB and 4,4'-DMHAB appearing at similar positions were assumed to be of the same types as those of 4-ABT. Based on this presumption, the relative intensities of the 19b, 3, and 9b analog-bands with respect to the 7a analog-band were calculated, and their variation against the excitation wavelength is shown in Figures 3(b) ~ (d). Regardless of the molecules used, the three relative intensities all increased as the excitation wavelength was decreased from 632.8 nm to 488 nm. Although the intensity variations look comparable to one another, the absolute values are clearly larger for all excitations in the order of 4,4'-DMAB > 4-ABT > 4,4'-DMHAB. This may also be indicative of the presence of three different molecules on Ag, implying that the photoreaction of 4,4'-DMAB, 4-ABT, and 4,4'-DMHAB on Ag is not likely to occur. The excitation wavelength-dependent relative peak intensities might then suggest that the 19b, 3, and 9b

analog-bands are associated with the chemical enhancement mechanism.

At previous result, it is reported already that the SERS spectral pattern of 4-ABT is subjected to change upon treatment with a borohydride solution [30]. For instance, the b_2 -type bands disappear upon contact with a borohydride solution, though they reappear when the 4-ABT-adsorbed Ag substrate is fully washed with water. The observed SERS spectral variation could be attributed to the potential lowering of the Ag substrate by the borohydride. Therefore, this work investigated again that how the SERS spectral patterns of 4,4'-DMAB and 4,4'-DMHAB would be affected by borohydride. In order to reduce the possibility of a surface-induced photoreaction as much as possible, this work used the 632.8 nm radiation as the excitation source. Figure 4(a) shows a series of SERS spectra of 4,4'-DMAB on Ag taken under ambient conditions after soaking for 10 min in a solution of borohydride at different concentrations. It is seen that all the SERS peaks decrease in intensity upon contact with a borohydride solution. As shown in Figure 4(b), the 7a analog-band at 1072 cm^{-1} decreases in intensity by almost 60% when the 4,4'-DMAB-adsorbed Ag substrate is soaked in a 30 mM solution. This may indicate that a fair amount of 4,4'-DMAB is desorbing from Ag through the treatment with borohydride; when the borohydride concentration is increased further up to 500 mM, the intensity decrease is, however, marginal. At any rate, an interesting observation is that the intensity ratios of the 19b, 3, and 9b analog-bands with respect to that of the 7a analog-band are also variable, depending on the concentration of the borohydride solution, as shown for 19b/7a in Figure 4(c).

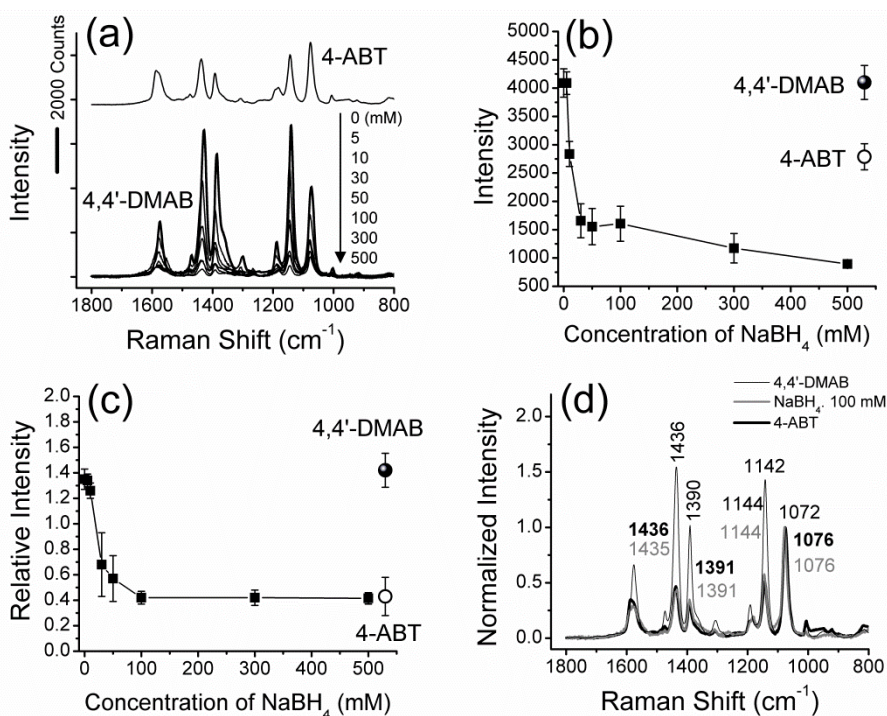


Figure 4. (a) A series of SERS spectra of 4,4'-DMAB on Ag taken under ambient conditions after soaking for 10 min in a solution of borohydride at different concentrations. Excitation wavelength was 632.8 nm. (b) Intensity of the 7a analogue-band at 1072 cm^{-1} in panel a, drawn versus the concentration of borohydride. For comparison, authentic intensities of the 7a analogue-bands of 4,4'-DMAB (black) and 4-ABT (white) are shown together. (c) Intensity of the 19b analogue-band with respect to that of the 7a analogue-band drawn versus the concentration of borohydride. For comparison, relative intensities of the authentic bands of 4,4'-DMAB (black) and 4-ABT (white) are shown together. (d) Spectral comparison of 4-ABT on Ag (thick black) with that of 4,4'-DMAB on Ag after treatment with a 100 mM solution of borohydride (gray); see, for comparison, the SERS spectrum of 4,4'-DMAB on Ag (thin black); all SERS spectra were normalized with respect to the intensity of the 7a analogue-band.

Before the treatment with borohydride, the intensity ratio of the 19b and 7a analogue-bands is 1.35. The ratio gradually decreases down to ~ 0.4 as the 4,4'-DMAB-adsorbed Ag substrate is soaked in a 100 mM solution, and then this value is

maintained until up to 500 mM of borohydride. It is noteworthy that the intensity ratio (0.4) observable from 4,4'-DMAB after soaking in 100 mM solution of borohydride is the same as that observable from the SERS of 4-ABT without any treatment. This may indicate that 4,4'-DMAB on Ag is reduced to 4-ABT by borohydride. Such a possibility could be ascertained by comparing spectra in all regions. Indeed, as shown in Figure 4(d), the SERS spectral pattern of 4,4'-DMAB after treatment with a 100 mM solution of borohydride overlaps exactly with that of 4-ABT; they both differ significantly from the authentic SERS spectrum of 4,4'-DMAB. Although not shown here, no spectral variation was observed at all when 4,4'-DMHAB on Ag was treated with a borohydride solution, although some molecules could desorb at higher concentrations.

The b_2 -type bands of 4-ABT are very susceptible to the solution pH in contact with 4-ABT on Au [31]. Under very acidic conditions (e.g. pH 2), the b_2 type bands were barely seen, but they became distinct under basic conditions (e.g. pH 10). Much the same observation can be made for 4-ABT adsorbed on Ag. In this work, it is found that the authentic SERS peaks of 4,4'-DMAB on Ag were not affected by the solution pH [17,31]. However, once the 4,4'-DMAB on Ag was soaked in a 100 mM borohydride solution, the b_2 -type peaks became considerably weaker upon soaking in an acidic solution, and they reappeared distinctly when soaked in a basic solution, as shown in Figure 5(a).

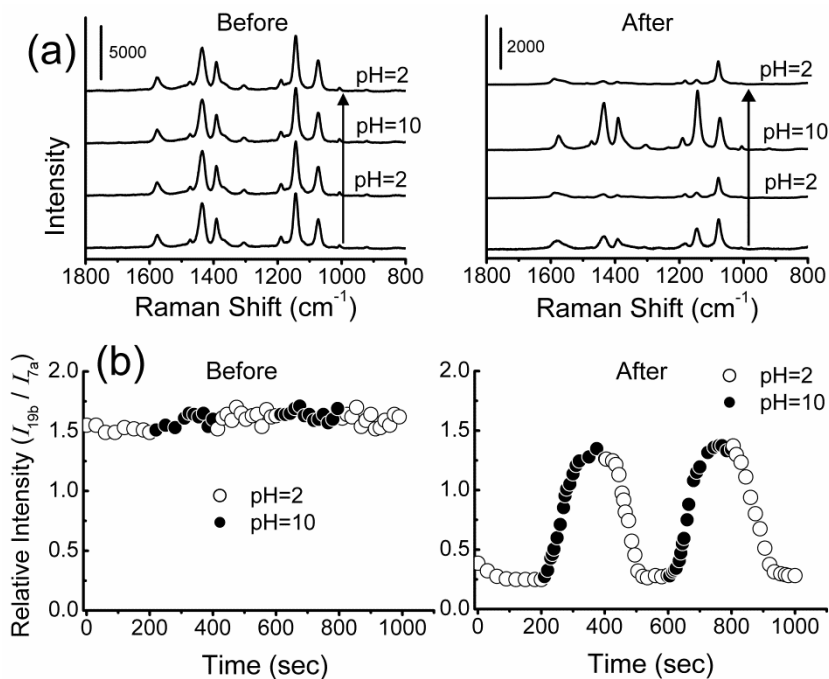


Figure 5. (a) pH dependency of SERS spectrum of 4,4'-DMAB on Ag measured before and after being soaked in a 100 mM borohydride solution: Excitation wavelength was 632.8 nm. (b) Variation of the 19b analogue-band intensity with respect to that of the 7a analogue-band measured as a function of time at pH 2 (filled circles) and 10 (open circles) before (blue) and after (red) treating with borohydride.

This was reproducibly observed as in Figure 5(b), ensuring that 4,4'-DMAB on Ag was reduced to 4-ABT by borohydride. Conversely, no pH dependence was observed at all for 4,4'-DMHAB on Ag even after treating with a borohydride solution. A separate measurement using a silver wire indicated that a solution of borohydride at 100 mM should correspond to the application of -1.21 V to Ag; similarly, 300 mM to -1.26 V and 500 mM to -1.29 V. Based on the effect of borohydride, this suggested that it would be useful to compare the potential-dependent SERS spectra of 4,4'-DMAB, 4-ABT, and 4,4'-DMHAB on Ag.

Figure 6(a) shows the potential-dependent SERS spectra of 4,4'-DMAB on Ag in 0.1 M NaClO₄ solution. The spectra shown in dark were measured as the electrode potential was gradually lowered from 0.0 V down to -1.2 V. As potential is lowered, the relative peak intensities are subjected to change [23]. In this context it should be mentioned that the variation is reproducible as far as the potential lowering is maintained above > -0.9 V. However, once the potential was lowered below -1.0 V, the original spectral pattern was not recovered at all even after raising the potential. This is evident from the spectra shown in red in Figure 6(a), which were measured after excursing first down to -1.2 V. The spectral variation in Figure 6(a) has been analyzed in terms of the relative intensity of the 19b and 7a analog-bands, and the results are collectively summarized in Figure 6(b). In Figure 6(b), the filled triangles correspond to the potential-dependent data observable under the very first measurement or at potentials always maintained above -0.9 V, while the empty triangles correspond to the potential-dependent data observable after the potential was excursed once down to -1.2 V. This work is also added the potential-dependent SERS data of 4-ABT on Ag as filled circles in Figure 6(b). It is notable that the empty triangles overlap exactly with the filled circles. This can be understood by presuming that 4,4'-DMAB is converted to 4-ABT by electrochemical reduction. This is consonant with the observation made using borohydride. The fact that the filled triangles were never recovered once the potential was excursed down to -1.2 V suggests that the conversion of 4,4'-DMAB to 4-ABT on Ag must be an irreversible process, at least under our experimental conditions.

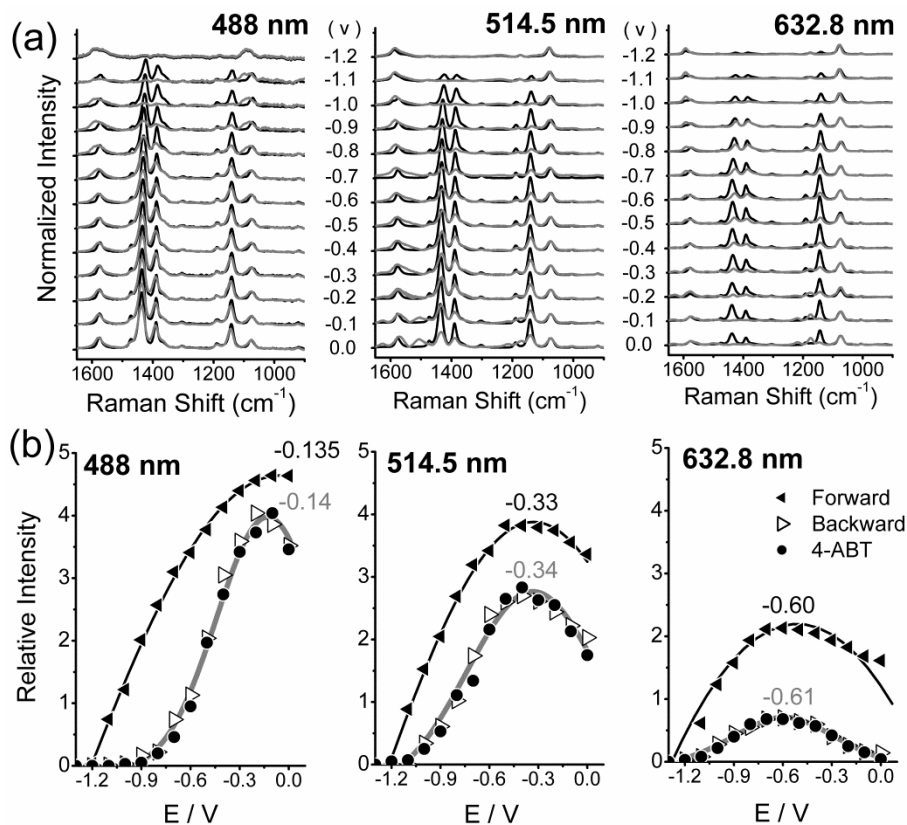


Figure 6. (a) Potential-dependent SERS spectra of 4,4'-DMAB on Ag in 0.1 M NaClO₄ solution taken using 488, 514.5, and 632.8 nm radiation as the excitation sources. Spectra in red were measured from 0.0 V after excusing first down to -1.2 V. (b) Variation of the 19b analogue-band intensity with respect to that of the 7a analogue-band in panel a, drawn versus the potential applied: the filled triangles correspond to the data observable under the very first measurement; the empty triangles correspond to the data observable after the potential was excused once down to -1.2 V; the filled circles represent the data measured separately for 4-ABT on Ag.

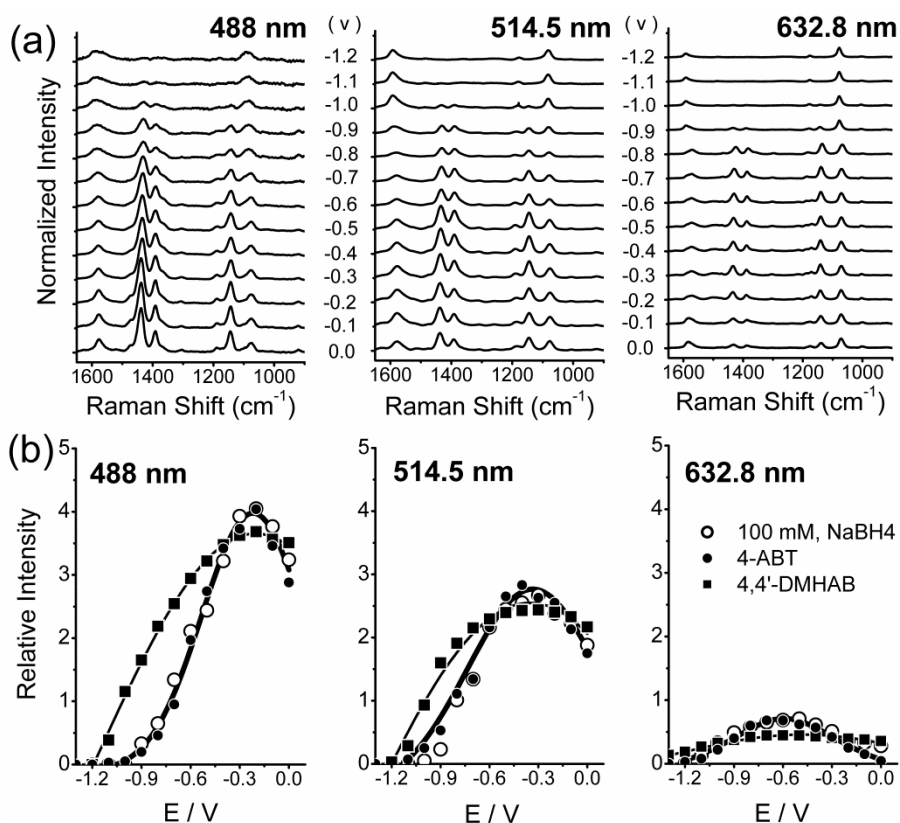


Figure 7. (a) Potential-dependent SERS spectra of 4,4'-DMAB adsorbed on Ag measured after being soaked for 10 min in a 100 mM borohydride solution taken using 488, 514.5, and 632.8 nm radiation as the excitation sources. (b) Variation of the 19b analogue-band intensity with respect to that of the 7a analogue-band in panel a, drawn versus potential applied (empty circles); see, for comparison, the data obtained from the authentic SERS spectra of 4-ABT (filled circles) and 4,4'-DMHAB (filled squares) on Ag.

Conversely, this may also imply that the conversion of 4-ABT on Ag to 4,4'-DMAB is an unfeasible process, not only photochemically but also electrochemically, at least in the potential region below 0.0 V.

To make sure that 4,4'-DMAB on Ag was converted to 4-ABT by borohydride, this work has taken a series of potential-dependent SERS spectra using 4,4'-DMAB-

adsorbed Ag as the working electrode immediately after being soaked for 10 min in a 100 mM borohydride solution. The spectra measured during the potential scan from 0.0 to -1.2 V are shown in Figure 7(a). The SERS spectral variation was the same as that of 4-ABT on Ag. This is evident from Figure 7(b) in which are shown the relative peak intensities of the 19b and 7a analog-bands in Figure 7(a) (see the empty circles), along with the relative intensities obtained separately from the authentic SERS spectra of 4-ABT on Ag (see the filled circles). Regardless of the excitation wavelength, the plot of the empty circles overlaps with that of the filled circles. This clearly supports the hypothesized conversion of 4,4'-DMAB on Ag to 4-ABT by borohydride. As shown in Figure 8, this work was also measured the potential dependent SERS spectra of 4,4'-DMHAB on Ag. The potential-dependency was reproducible in the region of 0.0 and -1.2 V, suggesting that neither electrochemical nor photochemical reaction took place for 4,4'-DMHAB on Ag. The relative intensities of the 19b and 7a analog-bands are also plotted in Figure 7(b) (see the filled squares). The pattern of variation is qualitatively similar to that of 4-ABT, but in quantitative terms, it is obviously different from that of 4-ABT, as well as from that of 4,4'-DMAB. This shows that 4,4'-DMAB is not converted at all to 4,4'-DMHAB. Taken together, we conclude that 4,4'-DMAB on Ag would convert to 4-ABT, but not 4-ABT to 4,4'-DMAB. Both the 4-ABT and 4,4'-DMHAB on Ag must be very stable so as not to be subjected to photochemical and electrochemical reaction. The 19b, 3, and 9b analog-bands appearing in the SERS of 4-ABT derivatives must all be associated with the chemical enhancement mechanism.

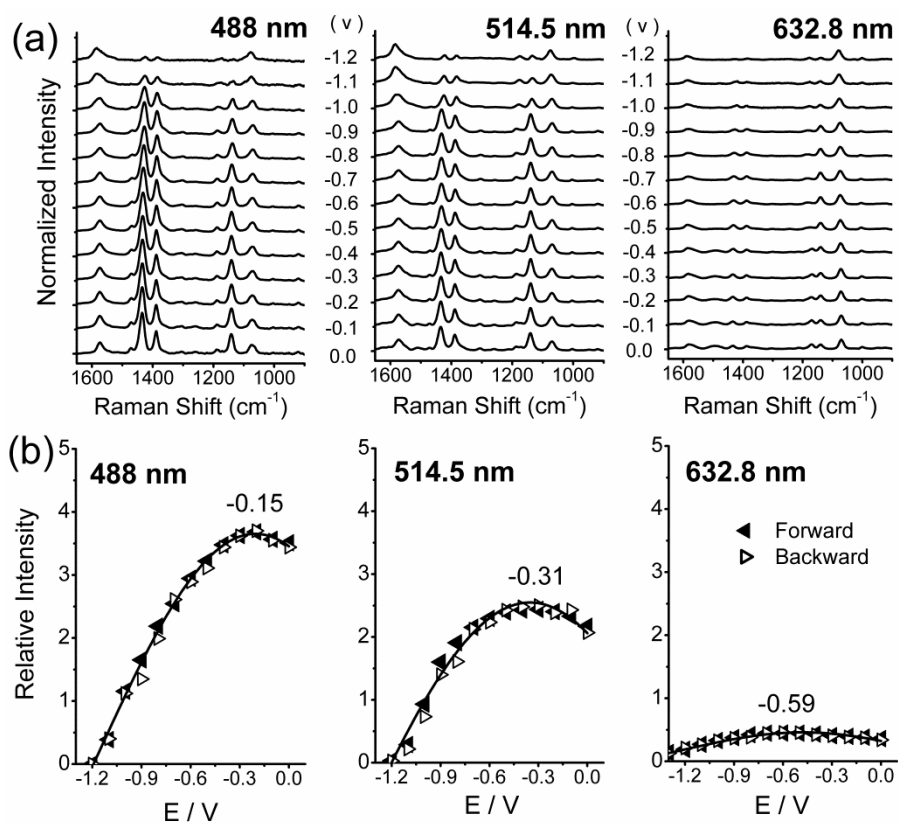


Figure 8. (a) Potential-dependent SERS spectra of 4,4'-DMHAB on Ag in 0.1 M NaClO₄ solution taken using 488, 514.5, and 632.8 nm radiation as the excitation sources. (b) Variation of 19b analog-band intensity with respect to that of 7a analog-band in (a) drawn versus potential applied: the filled triangles and empty triangles correspond to the data observable under the first forward and second backward sweep measurement, respectively.

Summary and Conclusion

It has long been known that the SERS spectral pattern of 4-ABT is considerably different to its NR spectrum. As a result, there has been a debate about whether the SERS spectrum of 4-ABT is due to 4-ABT itself or a certain photoreaction product. If it were due to a photoreaction product, 4,4'-DMAB has been claimed to be the most probable one. In light of this, this study has examined the similarity and dissimilarity in the SERS of 4-ABT and 4,4'-DMAB, along with the SERS of their analog molecule, 4,4'-DMHAB. Firstly, present results confirmed that the SERS spectral patterns of 4-ABT, 4,4'-DMAB, and 4,4'-DMHAB on Ag measured under ambient conditions are in fact comparable to one another. Since all the SERS peaks therein could be correlated fairly well with the NR peaks of 4,4'-DMAB (though not to the NR spectra of 4-ABT and 4,4'-DMHAB), it appeared that this work was witnessing the photoconversion of 4-ABT and 4,4'-DMHAB to 4,4'-DMAB. However, the excitation wavelength dependence of the absolute and relative peak intensities suggested that the similarity in the SERS spectral patterns does not guarantee such a photoconversion. On the other hand, the spectral dissimilarity could be evidenced by taking the SERS spectra after treating the substrates with a borohydride solution. By the treatment of borohydride, the SERS spectrum of 4,4'-DMAB became exactly the same as that of 4-ABT, although the spectrum of 4,4'-DMHAB was invariant, suggesting that 4,4'-DMAB could be reduced to 4-ABT. A separate potential-dependent SERS spectral measurement showed that the SERS spectral pattern of 4,4'-DMAB became indeed the same as that of 4-ABT as long as the electrode potential was once lowered below -1.0 V. The pH-dependency also

supported the conversion of 4,4'-DMAB to 4-ABT by an electrochemical reaction. No such reaction took place for 4,4'-DMHAB on Ag, however. Thus, overall, it appeared that 4,4'-DMAB might be reduced to 4-ABT, but the reverse reaction barely took place, not only electrochemically but also photochemically. Accordingly, the b_2 -type bands appearing in the SERS of 4-ABT have to be attributed to the chemical enhancement of 4-ABT itself.

References

1. Chang, R. K.; Furtak, T. E. *Surface Enhanced Raman Scattering*, Plenum Press: New York, **1982**.
2. Nitzan, A.; Brus, L. E. *J. Chem. Phys.* **1981**, *75*, 2205.
3. Goncher, G. M.; Harris, C. B. *J. Chem. Phys.* **1982**, *77*, 3767.
4. Goncher, G. M.; Parsons, C. A.; Harris, C. B. *J. Phys. Chem.* **1984**, *88*, 4200.
5. Wolkow, R. A.; Moskovits, M. *J. Chem. Phys.* **1987**, *87*, 5858.
6. Suh, J. S.; Jang, N. H.; Jeong, D. H.; Moskovits, M. *J. Phys. Chem.* **1996**, *100*, 805.
7. Sandroff, C. J.; Herschbach, D. R. *J. Phys. Chem.* **1982**, *86*, 3277.
8. Lee, S. B.; Kim, K.; Kim, M. S. *J. Phys. Chem.* **1992**, *96*, 9940.
9. Han, S. W.; Lee, I.; Kim, K. *Langmuir* **2002**, *18*, 182.
10. Kim, K. L.; Lee, S. J.; Kim, K. *J. Phys. Chem. B* **2004**, *108*, 9216.
11. Huang, Y. F.; Zhu, H. P.; Liu, G. K.; Wu, D. Y.; Ren, B.; Tian, Z. Q. *J. Am. Chem. Soc.* **2010**, *132*, 9244.

12. Wu, D.-Y.; Liu, X.-M.; Huang, Y.-F.; Ren, B.; Xu, X.; Tian, Z. Q. *J. Phys. Chem. C* **2009**, *113*, 18212.
13. Zhao, L.-B.; Huang, R.; Huang, Y.-F.; Wu, D.-W.; Ren, R.; Tian, Z. Q. *J. Chem. Phys.* **2011**, *135*, 134707.
14. Huang, Y.; Fang, Y.; Yang, Z.; Sun, M. *J. Phys. Chem. C* **2010**, *114*, 18263.
15. Sun, M.; Huang, Y.; Xia, L.; Chen, X.; Xu, H. *J. Phys. Chem. C* **2011**, *115*, 9629.
16. Fang, Y.; Li, Y.; Xu, H.; Sun, M. *Langmuir* **2010**, *26*, 7737.
17. Kim, K.; Shin, D.; Kim, K. L.; Shin, K. S. *Phys. Chem. Chem. Phys.* **2012**, *14*, 4095.
18. Uetsuki, K.; Verma, P.; Yano, T.-A.; Saito, Y.; Ichimura, T.; Kawata, S. *J. Phys. Chem. C* **2010**, *114*, 7515.
19. Park, W.-H.; Kim, Z. H. *Nano Lett.* **2010**, *10*, 4040.
20. Kim, N. J. *J. Phys. Chem. C* **2010**, *114*, 13979.
21. Hill, W.; Wehling, B. *J. Phys. Chem.* **1993**, *97*, 9451.
22. Zong, S.; Wang, Z.; Yang, J.; Cui, Y. *Anal. Chem.* **2011**, *83*, 4178.
23. Kim, K.; Kim, K. L.; Choi, J.-Y.; Shin, D.; Shin, K. S. *Phys. Chem. Chem. Phys.* **2011**, *13*, 15603.
24. Kim, K.; Shin, D.; Lee, H. B.; Shin, K. S. *Chem. Commun.* **2011**, *47*, 2020.
25. Zhou, Q.; Li, X.; Fan, Q.; Zhang, X.; Zheng, J. *Angew. Chem. Int. Ed.* **2006**, *45*, 3970.
26. Kim, N. H.; Lee, S. J.; Moskovits, M. *Adv. Mater.* **2011**, *23*, 4152.
27. Osawa, M.; Matsuda, N.; Yoshii, K.; Uchida, I. *J. Phys. Chem.* **1994**, *98*, 12702.

28. Kim, K.; Shin, D.; Choi, J.-Y.; Kim, K. L.; Shin, K. S. *J. Phys. Chem. C* **2011**, *115*, 24960.
29. Hans, E. F.-D. *The Fundamental Processes of Dye Chemistry*; D. Van Nostrand: New York, **1921**.
30. Kim, K.; Lee, H. B.; Shin, D.; Ryoo, H.; Lee, J. W.; Shin, K. S. *J. Raman Spectrosc.* **2011**, *42*, 2112.
31. Kim, K.; Kim, K. L.; Shin, D.; Choi, J.-Y.; Shin, K. S. *J. Phys. Chem. C* **2012**, *116*, 4774.

5-2. Photoreduction of 4,4'-DMAB on Ag Revealed by Raman Scattering Spectroscopy

Introduction

Both mechanisms in SERS suggest the possibility of enhanced absorption and photochemistry for surface-adsorbed molecules, although experimentally distinguishing the contributions of each mechanism is not so straightforward. However, the direct observation of a surface-enhanced photochemical reaction has indeed been reported [1-8].

The compound 4,4'-DMAB has recently come to a lot of attention, because its SERS spectral features are remarkably similar to those of 4-aminobenzenethiol (4-ABT), especially in Ag nanoaggregates [9-14]. As mentioned above repeatedly, 4-ABT itself is an unusual molecule in the sense that its SERS spectral features are dependent not only on the nature of the SERS substrate, but also on the measurement conditions [15-17]. According to Kim et al., the appearance of the b_2 -type bands is a general phenomenon in the SERS of 4-ABT analogs, possibly including 4,4'-DMAB from charge-transfer chemical enhancement effect [25-27]. On the other hand, another claim by Tian and Sun is that the b_2 -type bands appearing in the SERS of 4-ABT must be the N=N stretching vibrations of 4,4'-DMAB produced from 4-ABT via a catalytic coupling reaction on the metal

substrates [9-13]. The basis for this claim is the spectral similarity of 4-ABT and 4,4'-DMAB as described in section 4. However, only limited data are available on 4,4'-DMAB, which hinders exploration of the origin of the spectral similarity, since 4,4'-DMAB has to be custom synthesized.

Kim et al. recently investigated the SERS of 4,4'-DMAB trapped in Au nanogaps [26]. First, 4,4'-DMAB is probably adsorbed on a flame-annealed Au substrate via one of its two thiol groups, such that Au nanoparticles can be further adsorbed on the pendent thiol group, forming a SERS hot site. The most distinctive feature in the SERS of 4,4'-DMAB was the appearance of a_g bands, which were quite similar to the b_2 -type bands occurring in the SERS of 4-ABT. In an electrochemical environment, the a_g bands of 4,4'-DMAB at 1431, 1387, and 1138 cm^{-1} become weaker at lower potentials, completely disappearing at -1.0 V versus a saturated Ag/AgCl electrode [10]. However, the bands were restored when the electrode potential was increased, implying that neither an electro- nor photo-chemical reaction took place to break the azo group, which agrees with cyclic voltammetry data [26]. Thus, it was concluded that the appearance and disappearance of these a_g bands were associated with the charge-transfer phenomenon. There are also examined the similarity and dissimilarity of the SERS spectra of 4-ABT and 4,4'-DMAB, along with the SERS spectrum of the analogous molecule 4,4'-dimercaptopyrazobenzene (4,4'-DMHAB) [27]. In fact, under ambient conditions, the SERS spectra of 4-ABT, 4,4'-DMAB, and 4,4'-DMHAB on Ag were comparable to one another, although the excitation wavelength

dependence of the peak intensities indicated that the similarity of the SERS spectral patterns was not necessarily the result of photoconversion of the three molecules. On the other hand, spectral dissimilarity was observed not only in the potential-dependent SERS spectra, but also in the SERS spectra taken after treating the probing substrates with a borohydride solution. It appeared that 4,4'-DMAB on Ag could be converted to 4-ABT either by lowering the potential below -1.0 V or by treatment with 100 mM borohydride. Conversely, however, an electrochemical reaction did not take place for 4-ABT or 4,4'-DMHAB on Ag when the electrode potential was lowered even to -1.0 V or when the substrates were treated with a 100 mM borohydride solution [27]. These observations support that the b_2 -type bands appearing in the SERS of 4-ABT must be attributable to the chemical enhancement of 4-ABT itself.

In this section, it will show that 4,4'-DMAB on Ag can be converted to 4-ABT even photochemically. For that purpose, this work carefully examined the spectral variation of 4,4'-DMAB and 4-ABT on Ag as a function of laser irradiation time. When 514.5-nm radiation (with 2.1 mW power at the sampling position) was used as the excitation source, the SERS spectral pattern of 4,4'-DMAB varied gradually for 2 h under ambient conditions, finally becoming the same as that of 4-ABT on Ag. Supposing that the observed spectral variation is suggestive of the photoconversion of 4,4'-DMAB to 4-ABT, this work attempted to conduct two different reactions after exposure of 4,4'-DMAB on Ag to 514.5-nm radiation: a 1-ethyl-3-(3-(dimethylamino)propyl) carbodiimide (EDC)-mediated coupling

reaction with 4-cyanobenzoic acid (4-CBA) [28-30], and the biomimetic growth of a calcite crystal [30-33]. Although the EDC coupling reaction did not take place for neat 4,4'-DMAB on Ag, it did proceed after exposure to 514.5-nm radiation, as evidenced by the appearance of the CN stretching band of 4-CBA. As for the crystal growth, micrometer-sized calcite crystals readily grew after laser exposure, although only nanometer-sized calcite crystals were formed in the neat state, supporting the proposed photoconversion of 4,4'-DMAB to 4-ABT on Ag. The present observation completely contradicts claims made by a number of researchers that 4-ABT on Ag is converted photochemically to 4,4'-DMAB, not the reverse one.

Results and Discussion

Silver was used in this work as the SERS substrate since 4-ABT on Ag is known to exhibit a SERS spectrum similar to that of 4,4'-DMAB, especially when excited with a 514.5-nm laser. The Ag substrate prepared using citrate-reduced Ag nanoparticles is further known to be SERS active, not only with 514.5-nm radiation, but also 632.8-nm radiation, allowing for investigation of the excitation wavelength dependence. Figure 1(a) shows the field emission scanning electron microscopy (FE-SEM) image of the Ag nanoparticle film assembled on an amine-modified glass substrate. The Ag nanoparticles themselves are faceted and spherical in shape, with a mean diameter of 55 ± 16 nm. Isolated Ag nanoparticles exhibit a surface plasmon resonance (SPR) absorption band at 412 nm, but as they assemble into a close-packed aggregate, the SPR band is broadened into the visible and near

infrared region, as can be seen in Figure 1(b).

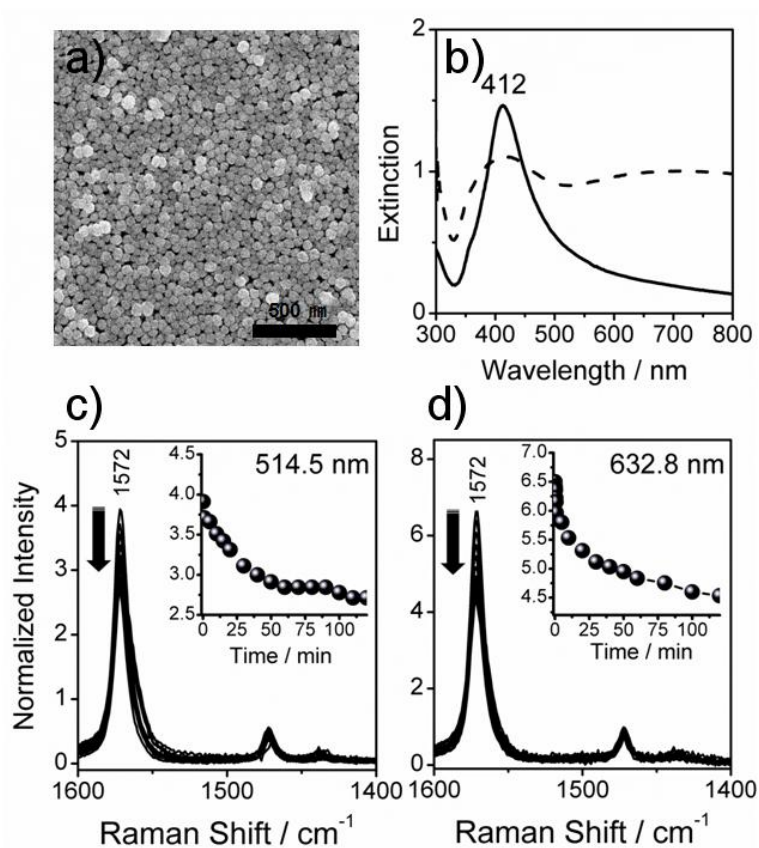


Figure 1. (a) FE-SEM image of Ag nanoparticle film (b) UV-vis extinction spectra of Ag nanoparticles in the colloidal state (solid line) and film state (dashed line). SERS spectra of BT on Ag nanoparticle film measured using (c) 514.5-nm and (d) 632.8-nm radiation as the excitation source. Insets show the variation of the SERS peak intensity as a function of laser irradiation time.

According to the electromagnetic enhancement mechanism, the Ag nanoparticle film must then be highly SERS active not only upon excitation at 514.5-nm but also upon excitation at 632.8-nm [34]. This was tested using BT as the probe molecule. Figures 1(c) and d show the SERS spectra of BT adsorbed on the Ag film measured using 514.5-nm and 632.8-nm radiation as the excitation source,

respectively. Indeed, very intense SERS spectra were obtained at both excitation wavelengths.

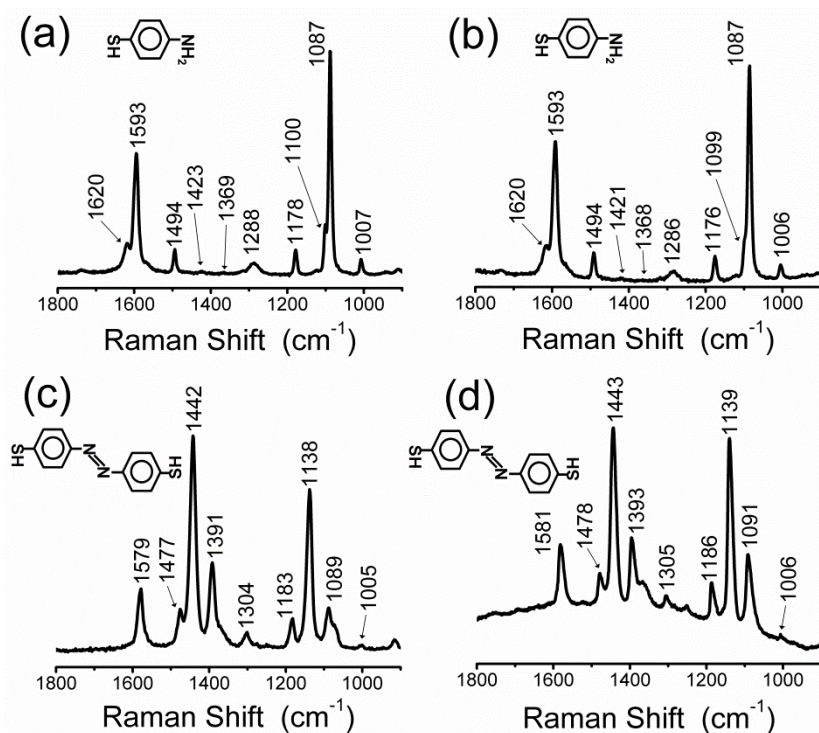


Figure 2. NR spectra of 4-ABT in the neat state measured using (a) 514.5-nm and (b) 632.8-nm radiation as the excitation source. NR spectra of 4,4'-DMAB in the neat state measured using (c) 514.5-nm and (d) 632.8-nm radiation as the excitation source.

For later reference, this study monitored the variation of the peak intensities of BT at 1572 cm^{-1} for 2 h, which might occur owing to a local heating of the Ag substrate. As shown in the insets of Figures 1(c) and 1(d), the SERS activity of Ag was lowered by about 37% after laser irradiation (not only at 514.5-nm, but also at 632.8-nm) for 2 h.

Figures 2(a) and 2(b) show the normal Raman (NR) spectra of 4-ABT in the neat state measured using 514.5-nm and 632.8-nm radiation as the excitation source,

respectively. Similarly, Figures 2(c) and 2(d) show the NR spectra of 4,4'-DMAB measured with excitation at 514.5-nm and 632.8-nm, respectively. For both 4-ABT and 4,4'-DMAB, the NR spectral patterns were insensitive to the excitation wavelength. It is well known that the spectral region between 1100 and 1500 cm^{-1} is almost featureless in the NR spectrum of 4-ABT, ignoring the very weak peaks at 1178 (ν_{9a} , a_1), 1288 ($\nu_{7a'}$, a_1), and 1494 cm^{-1} (ν_{19a} , a_1) [15]. The most intense NR peak for 4-ABT is at 1087 cm^{-1} , which can be attributed to the a_1 -type 7a band. In contrast, very intense peaks are identified in the region between 1100 and 1500 cm^{-1} in the NR spectrum of 4,4'-DMAB. These bands, including the band at 1442 cm^{-1} , can be attributed at least partly to the stretching motion of the N=N bond [10,26,27]. An a_g -type band of 4,4'-DMAB that can be correlated with the 7a band of 4-ABT appears at $\sim 1090 \text{ cm}^{-1}$, but its intensity is several times lower than that of the N=N stretching band at 1442 cm^{-1} . Here, it is clear that the NR spectral pattern of 4,4'-DMAB is very different from that of 4-ABT.

This work was subsequently recorded the SERS spectra of 4,4'-DMAB and 4-ABT on the Ag film using 514.5-nm radiation as the excitation source. The peak intensities were normalized with respect to that of a silicon wafer at 520 cm^{-1} . Major peaks with vibrational assignments in the NR and SERS spectra of 4,4'-DMAB and 4-ABT are collectively summarized in Table 4 (see page 140~141). This work noticed that the SERS peaks of 4-ABT and 4,4'-DMAB varied as a function of laser irradiation time, as collectively shown in Figures 3(a) and (b), respectively.

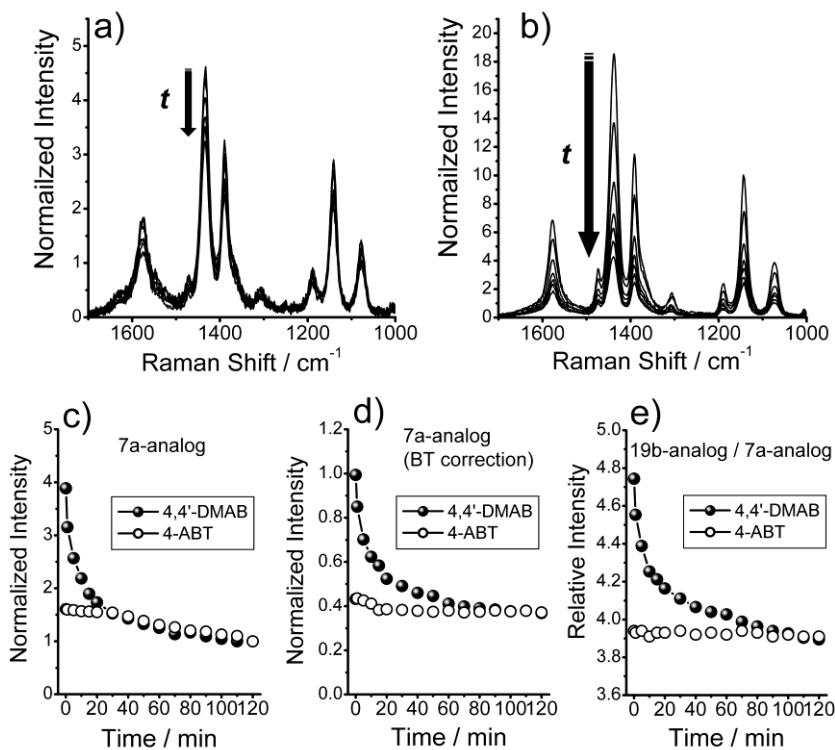


Figure 3. SERS spectra of (a) 4-ABT and (b) 4,4'-DMAB on Ag nanoparticle film measured using 514.5-nm radiation as the excitation source. Spectra measured over time are shown by different lines. (c) Normalized peak intensities of 7a-analog bands in (a) (empty circles) and (b) (filled circles) shown versus laser irradiation time. (d) The data shown in (c) corrected for the degradation of the SERS activity of the Ag film by referring to the SERS data of BT in Figure 1(c). (e) Relative intensity of the 19b- to 7a-analog bands in (a) and (b) shown versus laser irradiation time.

As can be seen in Figure 1, the SERS peaks of BT on Ag were lowered by as much as 37% after laser irradiation for 2 h, but the spectral pattern itself was maintained. However, in the cases of 4-ABT and 4,4'-DMAB, the SERS spectral patterns themselves were found to vary upon laser irradiation.

At any rate, it is evident that the SERS spectral pattern of 4-ABT in Figure 3(a) is completely different from its NR spectral pattern shown in Figure 2(a). In contrast,

the SERS spectral pattern of 4,4'-DMAB in Figure 3(b) is comparable to the NR spectral pattern of 4,4'-DMAB in Figure 2(c). Conversely, the SERS spectral pattern of 4,4'-DMAB is surprisingly similar to that of 4-ABT. It is for this reason that a few researchers have claimed that 4-ABT on Ag must have been converted to 4,4'-DMAB by a photoinduced coupling reaction [9-14]. However, Kim et al., previously claimed that the appearance of new bands in the region of 1100–1500 cm^{-1} in the SERS of 4-ABT were not caused by any surface-induced photoreaction, but instead had to do with a phenomenon common to all 4-ABT derivatives, possibly including 4,4'-DMAB, that is associated with the chemical enhancement mechanism in SERS [25-27]. To prove their earlier proposition, this work carefully monitored the intensity variation of the SERS peaks of 4-ABT and 4,4'-DMAB as a function of laser irradiation time. Assuming that 4-ABT on Ag is not subjected to any photoreaction, the peaks appearing at 1435, 1388, and 1141 cm^{-1} in the SERS of 4-ABT in Figure 3(a) must be assigned to the b_2 -type 19b, 3, and 9b modes, respectively, while the peak at 1090 cm^{-1} is the a_1 -type 7a band. For easy comparison of the SERS spectra of 4,4'-DMAB and 4-ABT, this work further presumes (momentarily) that the SERS peaks of 4,4'-DMAB appearing at similar positions are of the same types as those of 4-ABT. On this basis, the variation of the intensity of the 7a-analog band at 1090 cm^{-1} in Figure 3(b) is plotted in Figure 3(c) as a function of laser irradiation time, along with a similar plot for the 7a band in Figure 3(a). The intensity of the 7a-analog band due to 4,4'-DMAB decreases rapidly for the first 20 min and then slowly as a function of laser irradiation time,

while the 7a band of 4-ABT decreases monotonously from the beginning. The decrease in the intensity of the 7a-analog band at longer irradiation times in Figure 3(c) must be attributed, at least partly, to the degradation of the Ag film, as seen from the SERS of BT in Figure 1(c) [1,35]. Shown in Figure 3(d) is the intensity variation of the 7a-analog bands after correction for the degradation of the Ag film (deduced from the SERS of BT). It is clear from the figure that the 7a-analog band from 4,4'-DMAB decreased in intensity by a noticeable amount after laser irradiation, while the 7a band of 4-ABT is affected only by a limited amount. This may indicate that 4,4'-DMAB rather than 4-ABT is subjected to a photoreaction. To closely examine this possibility, this work was calculated the relative intensity of the 19b-analog band with respect to the 7a-analog band, and examined its variation relative to the laser irradiation time. Figure 3(e) shows the variation of the intensity ratios of the 19b-analog bands to the 7a-analog bands in Figures 3(a) and 3(b). While the intensity ratio for 4-ABT as a function of laser irradiation time is remained nearly constant, the intensity ratio observed for 4,4'-DMAB decreases rapidly until reaches the same ratio as that for 4-ABT. Supposing that all of the SERS peaks of 4,4'-DMAB occur without any photoreaction, but by the electromagnetic enhancement mechanism alone, the intensity ratio in Figure 3(e) must remain constant over time. However, the intensity ratio is found to decrease by as much as 62% over 2 h, and then becomes the same as that of 4-ABT. This may suggest that 4,4'-DMAB is converted to 4-ABT by a surface-induced photoreaction.

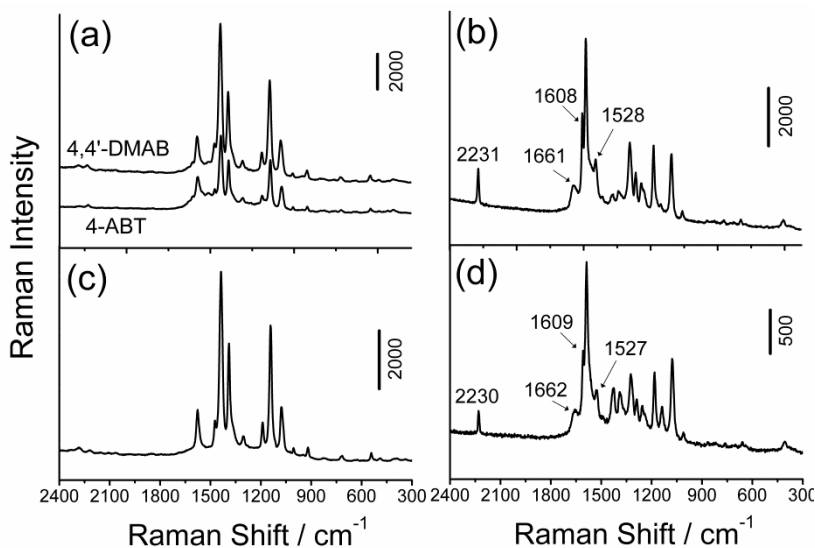


Figure 4. (a) SERS spectra of 4-ABT and 4,4'-DMAB on Ag measured before an EDC coupling reaction with 4-CBA. (b) SERS spectrum of 4-ABT on Ag measured after an EDC coupling reaction with 4-CBA. The EDC coupling reaction was performed for 30 min by injecting 0.02 M 4-CBA in DMF containing 0.02 M EDC into a glass capillary coated with 4-ABT-adsorbed Ag nanoparticle film. SERS spectra of 4,4'-DMAB on Ag measured after EDC coupling (c) without irradiation and (d) following 514.5-nm laser irradiation for 2.5 h.

This process is actually opposite to that previously reported by several researchers [1-8]. If the conversion of 4,4'-DMAB to 4-ABT occurs, it must be via a reductive reaction. 4,4'-DMAB on Ag could be reduced to 4-ABT upon treatment with a borohydride solution, as well as by lowering potential to -1.2 V versus a saturated Ag/AgCl electrode [27]. This study suppose that 4,4'-DMAB on Ag can be reduced to 4-ABT solely by a surface-induced photoreaction, similar to 4-nitrobenzenethiol on Ag [30,36,37].

To verify the occurrence of such a photoreaction, this study was attempted an EDC coupling reaction [30] with 4-CBA to form amide bonds after the irradiation of

4,4'-DMAB on Ag with 514.5-nm light. This work was first confirmed that 4-ABT on Ag reacts readily with 4-CBA in DMF. This is evident from Figure 4(a), which shows the SERS spectrum measured after the reaction. The peak at 2231 cm^{-1} is due to the CN stretching vibration arising from the formation of amide bonds between the amine group of 4-ABT and the acid group of 4-CBA. The bands at 1661 and 1528 cm^{-1} can be attributed to the amide I and II bands, respectively [38,39]. In contrast, here is also observed that the as-prepared 4,4'-DMAB on Ag did not react with 4-CBA, as can be seen in Figure 4(b), while the laser-irradiated 4,4'-DMAB on Ag readily reacted with 4-CBA to form amide bonds. This is evident from Figure 4(c), which shows the SERS spectrum of 4,4'-DMAB on Ag measured after EDC coupling with 4-CBA following 514.5-nm laser irradiation for 2.5 h. As seen for 4-ABT, this study attributes the newly observable peaks at 2230 and 1662 cm^{-1} in Figure 4(c) to the CN stretching and the amide I band arising from the formation of the amide bond, respectively. This observation strongly supports this study proposition that 4,4'-DMAB on Ag can be converted to 4-ABT by surface-induced photo-reduction. The photoconversion of 4,4'-DMAB upon 514.5-nm radiation was further confirmed by the selective growth of calcium carbonate. It is well known that functionalized organic surfaces can promote the nucleation of inorganic crystals such as calcite [30-33].

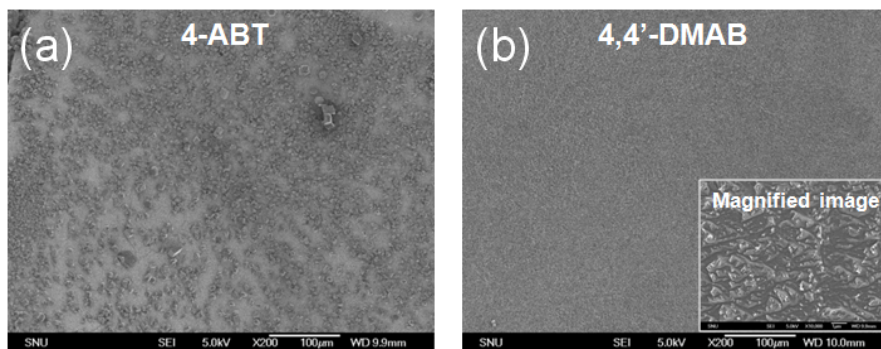


Figure 5. FE-SEM images of calcite crystals grown on (a) 4-ABT and (b) 4,4'-DMAB on roughened Ag foil. Inset shows the magnified image of (b).

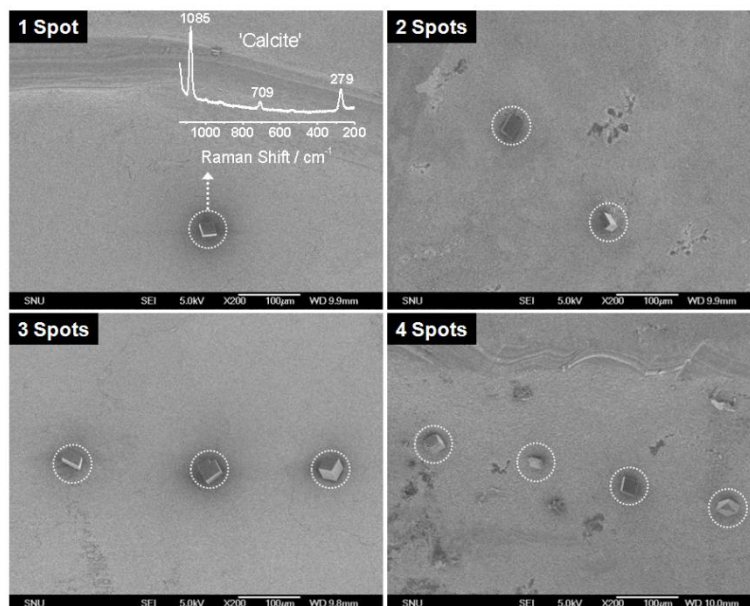


Figure 6. FE-SEM images of calcite crystals grown on 4,4'-DMAB on roughened Ag foil after irradiation with a 514.5-nm laser beforehand at different locations, each with either one, two, three, or four spots. Inset shows the Raman spectrum of the grown calcite.

This work was observed earlier that the crystallization of calcite occurs very facily on the amine-terminated regions, especially when carbonate ions are allowed to react with the amine groups before a calcium chloride solution is added. In fact, calcite grew readily on 4-ABT on Ag irrespective of the irradiation of either 514.5 or 632.8 nm radiation, while it grew on 4,4'-DMAB on Ag only after the irradiation of 514.5 nm radiation beforehand (see Figure 5). For clarity, after 4,4'-DMAB was self-assembled on Ag, different locations, each with one, two, three, or four spots, were irradiated with a focused Ar⁺ laser and then calcite crystals were grown on the spots after exposing the whole substrate to carbonate ions. As shown in Figure 6, the crystals grew to sizes of approximately 15 μm at specific sites, supposedly those exposed to the laser beam to produce the amine functionalities. The identity of calcite was confirmed from its Raman spectrum, as shown in the inset of Figure 6 (1 spot sample) [33]. At most, the sizes of the calcite crystals grown on the intrinsic surface of 4,4'-DMAB were as large as 10–20 nm. On the other hand, the growth of a calcite crystal was not observed on 4,4'-DMAB on Ag when it was similarly exposed to 632.8-nm radiation beforehand. This study was separately examined the excitation wavelength dependence. Figures 7(a) and 7(b) show a series of SERS spectra of 4-ABT and 4,4'-DMAB on Ag, respectively, measured as a function of time using 632.8-nm radiation as the excitation source. The measured intensities changed, but their variation was not the same as that observed for irradiation with 514.5-nm light.

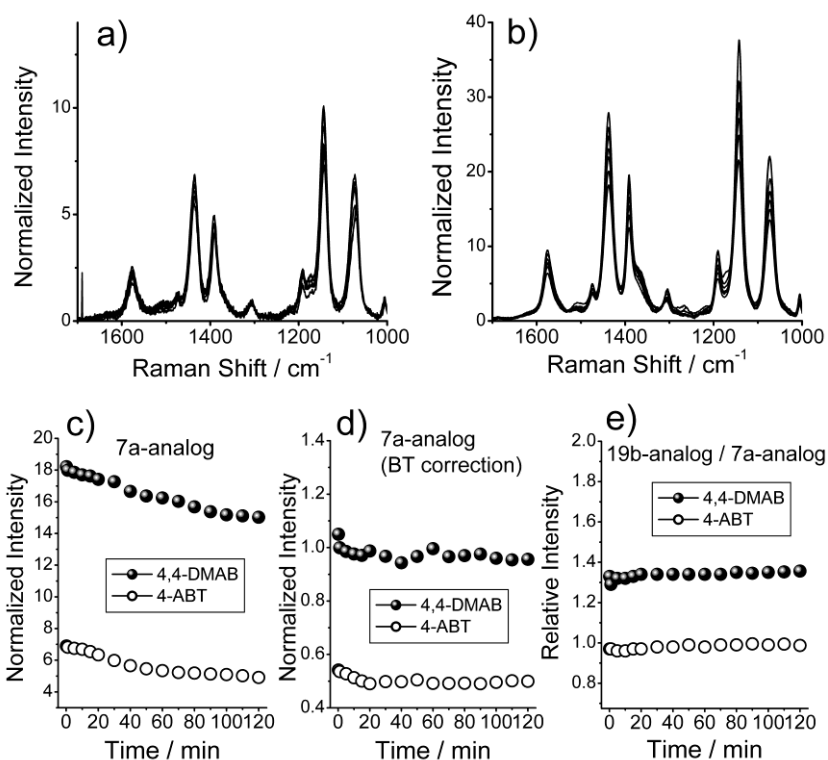
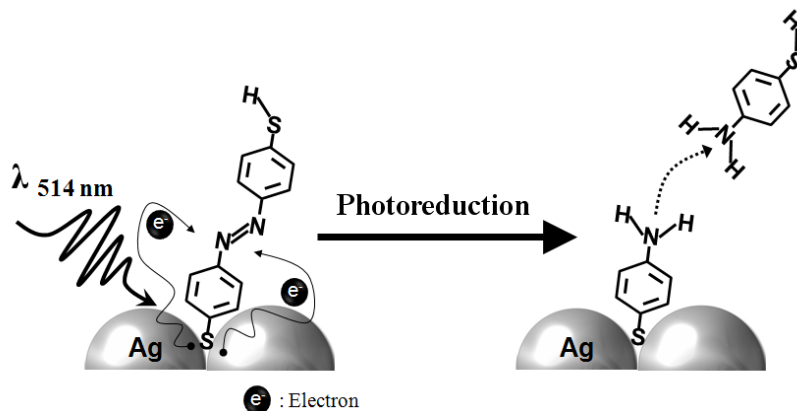


Figure 7. SERS spectra of (a) 4-ABT and (b) 4,4'-DMAB on Ag nanoparticle film measured using 632.8-nm radiation as the excitation source. Spectra measured over time are shown by different lines. (c) Normalized peak intensities of 7a-analog bands in (a) (empty circles) and (b) (filled circles) shown versus laser irradiation time. (d) The data shown in (c) corrected for the degradation of the SERS activity of the Ag film by referring to the SERS data of BT in Figure 1(d). (e) Relative intensity of the 19b- to 7a-analog bands in (a) and (b) shown versus laser irradiation time.

Figure 7(c) shows the variation of the intensity of the 7a-analog band at 1090 cm^{-1} as a function of laser irradiation time. Correcting for the effect of the degradation of the Ag film by referring to the SERS of BT in Figure 1(d), the 7a-analog band intensities remained at a fairly constant level throughout, without merging together.



Scheme 3. Schematic representation of the photoreduction of 4,4'-DMAB on Ag to 4-ABT.

A similar trend is seen for the intensity of the 19b-analog band relative to that of the 7a-analog band shown in Figure 7(d). That is, the relative intensities also remained fairly constant for both 4,4'-DMAB and 4-ABT. All of these observations suggest that no photoreaction takes place from 4,4'-DMAB to 4-ABT or from 4-ABT to 4,4'-DMAB upon irradiation at 632.8-nm.

Two particular questions are now raised: namely, how does the conversion of 4,4'-DMAB to 4-ABT on Ag proceed under 514.5-nm irradiation and what is the hydrogen source? The detailed mechanism of the azo-to-amine conversion on Ag is a matter of conjecture, but photoelectrons are known to be ejected from Ag even upon irradiation by a visible laser: Scheme 3 shows the schematic representation of the photoreduction of 4,4'-DMAB on Ag to 4-ABT suggested in this study. Although the work function of bulk silver was known to be ~ 4.3 eV, it has been observed by Fedurco et al. that the surface roughening of Ag results in a drastic increase of the photocurrent for the wavelength close to the surface plasmon

frequency [40]. Thus, plasmonic nanostructures of noble metals (mainly silver and gold) have recently received significant attention for their potential future use in solar energy conversion [41]. Theoretically, it has also been suggested that excited plasmon states can interact through an electron-scattering process with the unpopulated adsorbate levels, leading to an electron-induced dissociation reaction on a photo-excited plasmonic metal [42,43]. On the other hand, water in ambient condition has been claimed to act as a hydrogen source when 4-nitrobenzenethiol on Ag is converted to 4-ABT upon irradiation with an Ar⁺ laser [37]. A similar assumption must be made in order to explain the photo-induced conversion of 4,4'-DMAB to 4-ABT on Ag. It should be noted that the photoconversion of 4,4'-DMAB to 4-ABT is a quite slow process even on the Ag nanostructures under the irradiation with a focused Ar⁺ laser. At any rate, a novel experiment that clearly elucidates the mechanism of the photo-induced surface reaction, along with the origin of the hydrogen source, must be devised and this will be one of our future research directions.

Summary and Conclusion

It has been claimed in the literature that 4-ABT on Ag can be converted to 4,4'-DMAB via a catalytic coupling reaction. The basis for this claim was the spectral similarity of 4-ABT and 4,4'-DMAB. This work has argued against this view for a while, for several reasons. One reason was the observation that the appearance of the so-called b₂-type bands was a general phenomenon in the SERS of 4-ABT

analogs, possibly including 4,4'-DMAB. Another specific reason was that 4,4'-DMAB on Ag seemed capable of being converted to 4-ABT not only by treatment with a 100 mM borohydride solution, but also by exposure to a potential below -1.0 V, while the reverse reaction from 4-ABT to 4,4'-DMAB on Ag appeared to be insignificant electrochemically as well as photochemically. Developing a proper explanation of the origin of the b_2 -type bands in the SERS of 4-ABT is a challenging step toward a deeper understanding of the SERS mechanisms. In this sense, it is of utmost importance to examine the SERS spectrum of 4,4'-DMAB itself more carefully and to compare its measured characteristics with those of 4-ABT. Thus, this work carried out a SERS analysis of 4,4'-DMAB on Ag as a function of laser irradiation time. First, this study found that when 514.5-nm radiation was used as the excitation source, the SERS spectral pattern of 4,4'-DMAB on Ag varied as a function of laser irradiation time, finally becoming the same as that of 4-ABT on Ag. This suggested the possibility of the photoconversion of 4,4'-DMAB on Ag to 4-ABT. To confirm this premise, this study carried out an EDC coupling reaction and attempted to grow a calcite crystal on 4,4'-DMAB on Ag. It was found that the EDC coupling reaction with 4-CBA proceeded readily on 4,4'-DMAB on Ag after it was exposed to 514.5-nm radiation, but did not proceed without laser irradiation. Furthermore, the growth of a calcite crystal occurred readily on 4,4'-DMAB on Ag when it was similarly exposed to 514.5-nm radiation beforehand. On these grounds, this study finally arrived at the conclusion that, firstly, the appearance of the so-called b_2 -type bands in the SERS

of 4-ABT must be due to the involvement of the chemical enhancement mechanism, not due to the formation of 4,4'-DMAB, and secondly, even under ambient conditions, 4,4'-DMAB on Ag could be converted to 4-ABT upon irradiation with 514.5-nm light, but not with 632.8-nm light. This observation is, in fact, opposite to claims previously made by several researchers.

Table 4. Vibrational assignments for the normal Raman and SERS spectra of 4,4'-DMAB and 4-ABT.

4,4'-DMAB					
Normal Raman ^{a,b}			SERS ^{a,b}		Assignment ^{c,d}
Calculation ^c (PW91PW91)	Experiment				
	514.5 nm	632.8 nm	514.5 nm	632.8 nm	
	3062 vw	3062 vw	3077 w	3075 vw	vCH, ν_2
	2550 vw	2552 vw			vSH
1608.5	1579 s	1581 s	1575 s	1575 s	vCC (ν_{8a}), a_{g20}
1571.6	1525 vw	1523 vw			vCC (ν_{8b}), a_{g19}
1485.4	1477 w	1478 w	1471 sh	1471 sh	β CH+vNN+vCC (ν_{19a}), a_{g18}
1446.5	1442 vs	1443 vs	1436 vs	1436 vs	vNN+vCC+ β CH, a_{g17}
1407.2	1391 s	1393 s	1391 s	1391 s	vNN+vCC+ β CH, a_{g16}
1354.4	1304 w	1305 w	1306 w	1306 w	vCC (ν_{15}), a_{g15}
1205.1	1183 s	1186 s	1188 s	1188 s	vCN+ β CH+vCC, a_{g13}
1143.2	1138 vs	1139 vs	1140 vs	1140 vs	β CH+vCN, a_{g12}
1091.7	1089 s	1091 s	1072 s	1072 s	vCC+vCN (ν_1), a_{g10}
	1005 vw	1006 vw	1006 vw	1006 vw	α CCC+vCC (ν_{12})

4-ABT					
Normal Raman ^{a,b}			SERS ^{a,b}		Assignment ^f
Calculation ^c (B3LYP)	Experiment				
	514.5 nm	632.8 nm	514.5 nm	632.8 nm	
	3050 m	3050 w	3079 w	3078 vw	vCH, (ν_2), a_1
	2551 m	2551 w			vSH
1664	1616 w	1616 w			δ NH
1637.3	1593 s	1592 s	1591 w	1591 m	vCC, (ν_{8a}), a_1
1606.5	1581 sh	1581 sh	1573 m	1576 w	vCC, (ν_{8b}), b_2
1526.3	1494 vw	1494 vw	1487 vw	1487 vw	vCC+ δ CH, (ν_{19a}), a_1
	1480 vw	1480 vw	1472 w	1474 w	
1453.1	1423 vw	1421 vw	1436 vs	1435 vs	vCC+ δ CH, (ν_{19b}), b_2
	1369 vw	1368 vw	1389 s	1390 s	δ CH+vCC, (ν_3), b_2
1346.7	1309 vw	1309 vw	1306 vw		vCC+ δ CH, (ν_{14}), b_2
	1288 w	1286 w			vCH, (ν_{7a}), a_1
	1206 w	1206 w	1187 w	1185 w	
1202.1	1178 m	1176 m	1176 m	1174 m	δ CH, (ν_{9a}), a_1
1146.8	1142 sh	1142 sh	1142 m	1143 s	δ CH, (ν_{9b}), b_2
	1118 w	1118 w			δ CH, (ν_{15}), b_2
1108.8	1087 vs	1087 vs	1073 m	1074 s	vCS, (ν_{7a}), a_1
1023.4	1007 m	1006 m	1005 w	1006 vw	γ CC+ γ CCC, (ν_{18a}), a_1

^aUnits of wavenumber (cm^{-1}). ^bvs, very strong; s, strong; w, weak; vw, very weak; sh, shoulder; v, stretch; α , β , and δ , bend. ^{c,d}Taken from Ref. S1 and S2, respectively. ^{e,f}Taken from Ref. S3 and S4, respectively. Ring modes of 4-ABT correspond to those of benzene under C_{2v} symmetry. Calculation information on PW91PW91 and B3LYP, see Ref. S4 and Ref. S3, respectively.

References

1. Nitzan, A.; Brus, L. E. *J. Chem. Phys.* **1981**, *75*, 2205.
2. Goncher, G. M.; Harris, C. B. *J. Chem. Phys.* **1982**, *77*, 3767.
3. Sandroff, C. J.; Herschbach, D. R. *J. Phys. Chem.* **1982**, *86*, 3277.
4. Goncher, G. M.; Parsons, C. A.; Harris, C. B. *J. Phys. Chem.* **1984**, *88*, 4200.
5. Wolkow, R. A.; Moskovits, M. *J. Chem. Phys.* **1987**, *87*, 5858.
6. Suh, J. S.; Jang, N. H.; Jeong, D. H.; Moskovits, M. *J. Phys. Chem.* **1996**, *100*, 805.
7. Lee, S. B.; Kim, K.; Kim, M. S. *J. Phys. Chem.* **1992**, *96*, 9940.
8. Kim, K. L.; Lee, S. J.; Kim, K. *J. Phys. Chem. B* **2004**, *108*, 9216.
9. Fang, Y.; Li, Y.; Xu, H.; Sun, M. *Langmuir* **2010**, *26*, 7737.
10. Huang, Y. F.; Zhu, H. P.; Liu, G. K.; Wu, D. Y.; Ren, B.; Tian, Z. Q. *J. Am. Chem. Soc.* **2010**, *132*, 9244.
11. Sun, M.; Xu, H. *Small* **2012**, *8*, 2777.
12. Wu, D.-Y.; Liu, X.-M.; Huang, Y.-F.; Ren, B.; Xu, X.; Tian, Z. Q. *J. Phys. Chem. C* **2009**, *113*, 18212.
13. Sun, M.; Huang, Y.; Xia, L.; Chen, X.; Xu, H. *J. Phys. Chem. C* **2011**, *115*, 9629.
14. Zong, S.; Wang, Z.; Yang, J.; Cui, Y. *Anal. Chem.* **2011**, *83*, 4178.
15. Osawa, M.; Matsuda, N.; Yoshii, K.; Uchida, I. *J. Phys. Chem.* **1994**, *98*, 12702.
16. Zhou, Q.; Li, X.; Fan, Q.; Zhang, X.; Zheng, J. *Angew. Chem. Int. Ed.* **2006**, *45*, 3970.

17. Uetsuki, K.; Verma, P.; Yano, T.-A.; Saito, Y.; Ichimura, T.; Kawata, S. *J. Phys. Chem. C* **2010**, *114*, 7515.
18. Park, W.-H.; Kim, Z. H. *Nano Lett.* **2010**, *10*, 4040.
19. Kim, N. J. *J. Phys. Chem. C* **2010**, *114*, 13979.
20. Ikeda, K.; Suzuki, S.; Uosaki, K. *Nano Lett.* **2011**, *11*, 1716.
21. Wang, X.; Shi, W.; She, G.; Mu, L. *J. Am. Chem. Soc.* **2011**, *133*, 16518.
22. Kim, K.; Shin, D.; Lee, H. B.; Shin, K. S. *Chem. Commun.* **2011**, *47*, 2020.
23. Ye, J.; Hutchison, J. A.; Uji-i, H.; Hofkens, J.; Lagae, L.; Maes, G.; Borghsa, G.; Van Dorpea, P. *Nanoscale* **2012**, *4*, 1606.
24. Kim, K.; Kim, K. L.; Shin, D.; Choi, J.-Y.; Shin, K. S. *J. Phys. Chem. C* **2012**, *116*, 4774.
25. Kim, K.; Shin, D.; Choi, J.-Y.; Kim, K. L.; Shin, K. S. *J. Phys. Chem. C* **2011**, *115*, 24960.
26. Kim, K.; Shin, D.; Kim, K. L.; Shin, K. S. *Phys. Chem. Chem. Phys.* **2012**, *14*, 4095.
27. Kim, K.; Kim, K. L.; Lee, H. B.; Shin, K. S. *J. Phys. Chem. C* **2012**, *116*, 11635.
28. Katz, E.; Itzhak, N.; Willner, I. *Langmuir* **1993**, *9*, 1392.
29. Checkik, V.; Crooks, R. M.; Stirling, C. J. M. *Adv. Mater.* **2000**, *12*, 1161.
30. Han, S. W.; Lee, I.; Kim, K. *Langmuir* **2002**, *18*, 182.
31. Albeck, S.; Aizenberg, J.; Addadi, L.; Weiner, S. *J. Am. Chem. Soc.* **1993**, *115*, 11691.
32. Aizenberg, J.; Black, A.; Whitesides, G. M. *J. Am. Chem. Soc.* **1999**, *121*, 4500.
33. Lee, I.; Han, S. W.; Choi, H. J.; Kim, K. *Adv. Mater.* **2001**, *13*, 1617.

34. Moskovits, M. *Rev. Mod. Phys.* **1985**, *57*, 783.
35. Lee, S. J.; Baik, J. M.; Moskovits, M. *Nano Lett.* **2008**, *8*, 3244.
36. Matsuda, N.; Sawaguchi, T.; Osawa, M.; Uchida, I. *Chem. Lett.* **1995**, 145.
37. Kim, K.; Lee, Y. M.; Lee, H. B.; Park, Y.; Bae, T. Y.; Jung, Y. M.; Choi, C. H.; Shin, K. S. *J. Raman Spectrosc.* 2010, *41*, 187.
38. Han, S. W.; Han, H. S.; Kim, K. *Vib. Spectrosc.* **1999**, *21*, 133.
39. Bahng, M. K.; Cho, N. J.; Park, J. S.; Kim, K. *Langmuir* **1998**, *14*, 463.
40. Fedurco, M.; Shklover, V.; Augustynski, J. *J. Phys. Chem. B* **1997**, *101*, 5158.
41. Christopher, P.; Xin, H.; Linic, S. *Nat. chem.* **2011**, *3*, 467.
42. Buntin, S. A.; Richter, L. J.; Cavanagh, R. R.; King, D. S. *Phys. Rev. Lett.* **1998**, *61*, 1321.
43. Olsen, T.; Gavnholt, J.; Schiøtz, J. *Phys. Rev. B* **2009**, *79*, 035403.

5-3. Visible-Light Response of 4-Aminobenzenethiol and 4,4'-Dimercaptoazobenzene Silver Salts

Introduction

Silver thiolate (AgSR) and silver carboxylate (AgCO₂R) are members of a class of organic-inorganic heterostructured materials that possess a layered structure [1-5]. Upon heating, AgSR and AgCO₂R undergo dramatic structural changes to producing thiol- and acid-derivatized Ag nanoparticles, respectively [5-11]. Ag nanostructures are also produced by irradiation with a visible laser, which suggests that AgSR and AgCO₂R can be used as photo-imaging materials [12-15]. In this investigation, 4-ABT and 4,4'-DMAB silver salts are chosen as model silver thiolate compounds because their SERS characteristics are often difficult to distinguish [16-25]. Each salt has two reaction sites: the silver ion and the amine or azo group.

In this work, it was examined for the photo-responses of the silver salts of 4-ABT and 4,4'-DMAB, i.e., Ag-4ABT and Ag-4,4'DMAB, respectively, to provide further evidence for the feasibility of the photoconversion of 4,4'-DMAB on Ag to 4-ABT as described in section 5. The initial goal of this study is to determine whether 4,4'-DMAB forms a layered silver salt with 1:1 composition likely 4-ABT or a 1:2 adduct with the formula of [C₁₂H₈N₂S₂Ag₂]. Secondly, the NR spectra of

the Ag salts and those of their parent thiol molecules are compared to ensure that the NR spectral pattern of 4-ABT is intrinsically different from that of 4,4'-DMAB. Thirdly, the aim of this study is to elucidate the effect of visible-light laser illumination on the Raman spectra of the Ag salts. Accordingly, it was determined that the layered compounds had 1:1 compositions via X-ray diffractograms and elemental analyses, the NR spectra of Ag-4ABT and Ag-4,4'DMAB were different, and prolonged irradiation of the salts with an argon laser at 514.5 nm changed the Raman spectra until they were the same for both salts; in contrast, the spectral dissimilarity persisted under illumination with 632.8 nm radiation. Based on the spectral similarities, this work conclude that 4,4'-DMAB on Ag converts to 4-ABT under 514.5 nm irradiation [25].

Results and Discussion

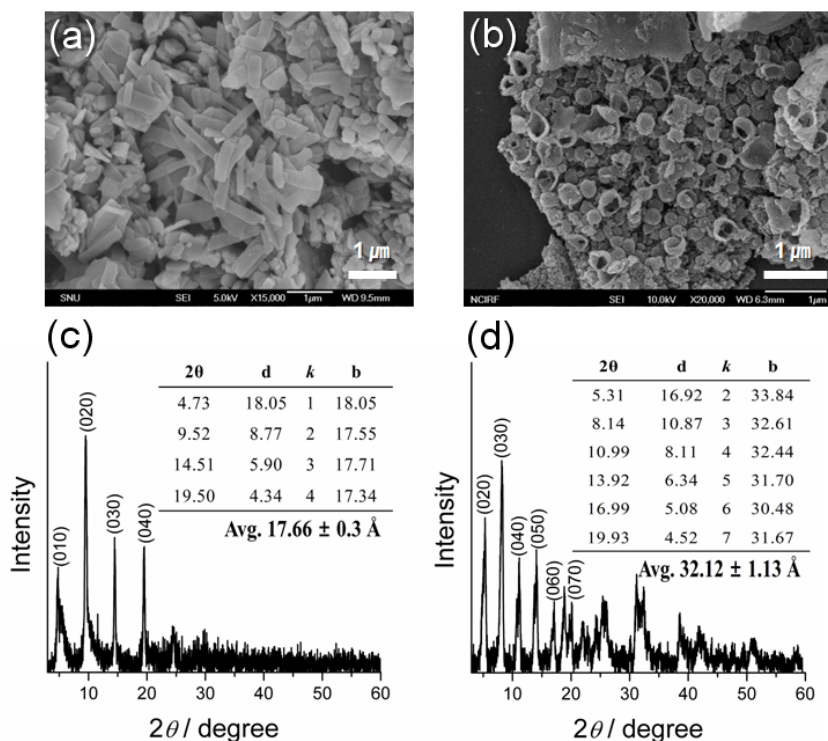


Figure 1. FE-SEM images of (a) Ag-4ABT and (b) Ag-4,4'DMAB, and XRD patterns of (c) Ag-4ABT and (d) Ag-4,4'DMAB. Insets in (c) and (d) display the interlayer spacings derived from different XRD reflections.

The addition of aqueous AgNO_3 solution to toluene solutions of 4-ABT and 4,4'-DMAB resulted in the formation of precipitates, which did not dissolve in either polar or nonpolar solvents. The FE-SEM images shown in Figures 1(a) and 1(b) reveal that the Ag-4ABT and Ag-4,4'DMAB salts had plate-like and tubular morphologies, respectively, up to the micrometer range in size. This difference in morphology must originate from the different energies of the intermolecular interactions in the two Ag salts [2-5,7,9].

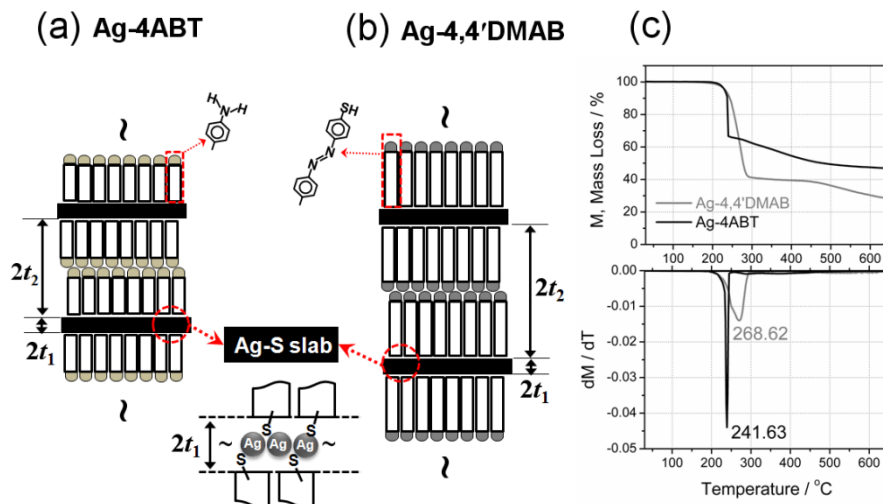


Figure 2. Schematic structures of (a) Ag-4ABT and (b) Ag-4,4'DMAB, and (c) their TGA and DSC data.

The elemental analysis data were in good agreement with that expected for a 1:1 Ag-4ABT salt. According to earlier publication, it was proposed that the silver salt of 4-ABT comprised a layered structure [10]. As expected, the XRD pattern of Ag-4ABT shown in Figure 1(c) reveals a well-developed progression of intense reflections, which were indexed as $(0\ k\ 0)$. Accordingly, a layered structure is shown in the schematic representation of the Ag-4ABT salt in Figure 2(a); in this structure, the silver thiolate layers are separated by a distance equal to twice the length of the 4-aminophenyl ring [9,10]. The inset of Figure 1(c) shows the interlayer spacings that were derived from different reflections: The average interlayer-thickness, i.e. the sum of $2t_1$ and $2t_2$ in Figure 2(a), is $17.66 \pm 0.30 \text{ \AA}$, which agrees well with the previously published value [10].

The XRD pattern of Ag-4,4'DMAB, which is shown in Figure 1(d), also shows evidence of a layered structure. With the intense reflections therein assigned as $(0\ k\ 0)$

0), the interlayer spacing was calculated to be $32.12 \pm 1.13 \text{ \AA}$, which is about twice that of Ag-4ABT; this indicates that, in agreement with the elemental analyses, the Ag^+ ions and 4,4'-DMAB form a 1:1 salt. Accordingly, the layered structure of the Ag-4,4'DMAB salt can be drawn as shown in Figure 2(b). Similar to an amine group of 4-ABT, one thiol moiety from 4,4'-DMAB must remain intact and not bind to Ag. The van der Waals interaction of two $-\text{SH}$ groups that are in direct contact in interlayers of Ag-4,4'DMAB with one above and the other below is presumed to be stronger than that of the two corresponding $-\text{NH}_2$ groups in Ag-4-ABT. This is evident from the TGA curves shown in Figure 2(c): The decomposition of Ag-4ABT at $242 \text{ }^\circ\text{C}$ is abrupt, whereas that of Ag-4,4'DMAB at $269 \text{ }^\circ\text{C}$ is quite gradual.

Figures 3(a) and (b) show the Raman spectra of neat 4-ABT and pelletized Ag-4ABT, respectively, and Figures 3(c) and (d) show the Raman spectra of neat 4,4'-DMAB and pelletized Ag-4,4'DMAB, respectively; these spectra were recorded using 514.5 nm radiation for excitation. Further, it should be noted that the spectra of the pelletized Ag salts (Figures 3(b) and (d)) were recorded with spinning at 3000 rpm to suppress the photoinduced reaction [9,10,30]. Also, the spectra obtained using a 632.8 nm excitation source were the same as those in Figure 3 (data not shown) [10].

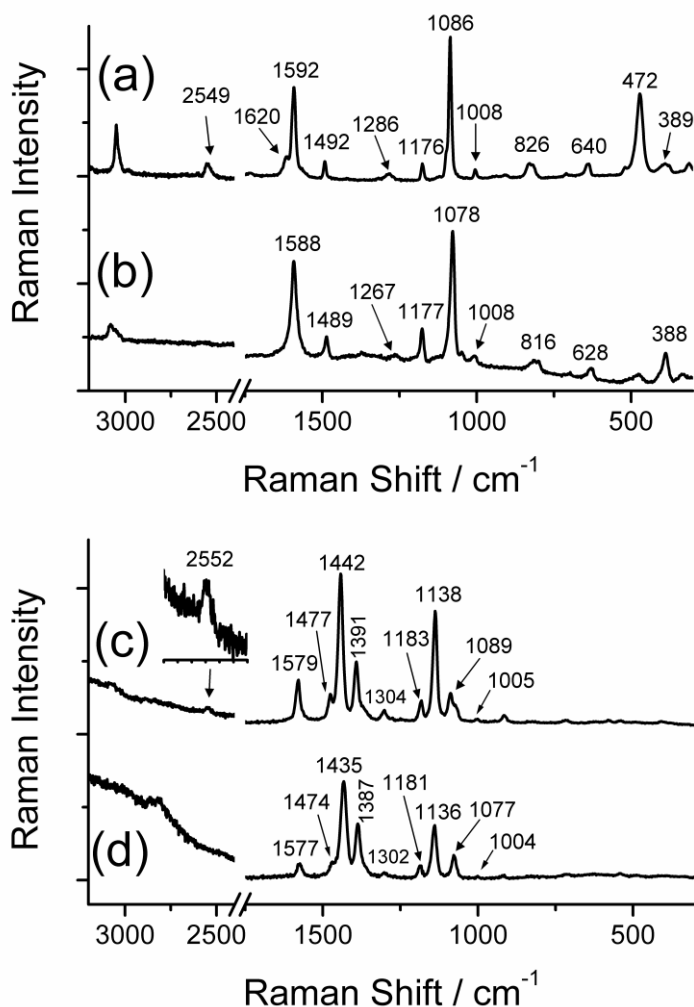


Figure 3. Raman spectra of (a) 4-ABT, (b) Ag-4ABT, (c) 4,4'-DMAB, and (d) Ag-4,4'DMAB measured using 514.5 nm radiation for excitation. The salt spectra in (b) and (d) were measured with spinning at 3000 rpm.

Comparing the spectra shown in Figures 3(a) and (b), it is evident that the Raman spectral patterns of Ag-4ABT and neat 4-ABT are quite similar. Likewise, the Raman spectral pattern of Ag-4,4'DMAB in Figure 3(d) is similar to that of 4,4'-DMAB in Figure 3(c). This suggests that the Ag salt does not undergo a

photoreaction, at least while spinning at 3000 rpm. The most obvious differences in the spectra of Ag-4ABT and neat 4-ABT shown in Figures 3(a) and (b) are observed in the S–H stretching and C–C–C bending regions around 2549 and 472 cm^{-1} , respectively. The absence of the S–H stretching band in the Raman spectrum of Ag-4ABT is expected; however, the reason behind the weakening of the C–C–C bending band at 472 cm^{-1} upon the formation of the Ag salt is not clear. The spectral differences of 4,4'-DMAB and pelletized Ag-4,4'DMAB (Figures 3(c) and (d)) are not as substantial. A weak S–H stretching band is apparent at 2552 cm^{-1} for neat 4,4'-DMAB, while it is difficult to confirm the presence of the S–H stretching band for Ag-4,4'DMAB due to the noisy and uneven background [24,25].

Comparing the Raman spectrum of Ag-4ABT with that of Ag-4,4'DMAB, the most obvious differences are in the spectral region between 1100 and 1500 cm^{-1} ; while this region is nearly featureless in the Raman spectrum of Ag-4ABT, several intense peaks are evident in the spectrum of Ag-4,4'DMAB. A similar difference is evident in the Raman spectra of 4-ABT and 4,4'-DMAB. The three intense bands at ~1440, ~1387, and ~1139 cm^{-1} in the spectra of 4,4'-DMAB and Ag-4,4'DMAB (Figures 3(c) and (d)) are at least partly due to the stretching motion of the azo moiety [24,25]. The most intense peak for Ag-4ABT is found outside of the spectral region, i.e., at ~1078 cm^{-1} and is attributed to the intrinsic a_1 -type 7a band. Similar a_g -type bands are also evident for Ag-4,4'DMAB and 4,4'-DMAB at ~1077 cm^{-1} ; however, their intensity is several times lower than that of the N=N stretching band at ~1440 cm^{-1} . Overall, it is clear that the Raman spectral patterns

of Ag-4ABT and Ag-4,4'DMAB are significantly different [24,25].

The Raman spectra of the Ag salts vary as the spectra are acquired under static conditions. One reason for this spectral change is the production of SERS-active Ag nanoparticles [9-11]. The extent of the spectral variation depends on the excitation wavelength [9,10]. Initially, 514.5 nm radiation is used as the excitation source. Figures 4(a) and (b) show temporally evolved Raman spectra of Ag-4ABT and Ag-4,4'DMAB, respectively, that were measured in static conditions under illumination with a 514.5 nm laser. As indicated by the arrow in Figure 4(a), new peaks appeared in the spectrum of Ag-4ABT during laser irradiation that were notably at nearly the same positions as those in the NR spectrum of Ag-4,4'DMAB (Figure 3(d)). The three peaks evolved in the region between 1500 and 1100 cm^{-1} at 1433, 1387, and 1139 cm^{-1} . Under static conditions, the Raman spectrum of Ag-4ABT increasingly resembles that of Ag-4,4'DMAB. In contrast, the peaks corresponding to Ag-4,4'DMAB weakened after prolonged laser irradiation, as is evident in Figure 4(b). It is very noteworthy that the Raman spectra of Ag-4,4'DMAB eventually become the same as those of Ag-4ABT. This is further evidenced by the temporal evolution of the Raman intensity of the a_1 -analog band ($\sim 1080 \text{ cm}^{-1}$) as well as the time dependent relative intensities of the b_2 -analog ($\sim 1433 \text{ cm}^{-1}$) and a_1 -analog bands ($\sim 1080 \text{ cm}^{-1}$); herein, the Raman peaks of Ag-4ABT and Ag-4,4'DMAB that appear in the spectral region between 1100 and 1500 cm^{-1} are tentatively assigned as b_2 -analog bands, whereas the band appearing at $\sim 1080 \text{ cm}^{-1}$ is assigned as an a_1 -analog band [24].

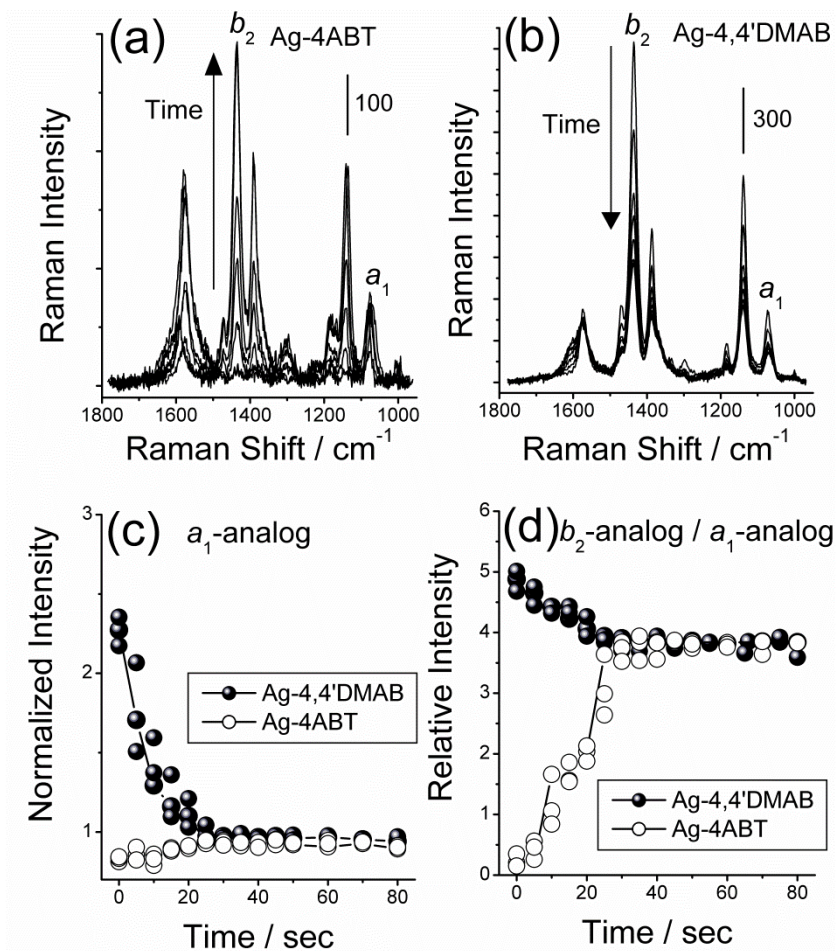


Figure 4. Temporally evolved Raman spectra of (a) Ag-4ABT and (b) Ag-4,4'DMAB under 514.5 nm light illumination and static conditions. Spectra measured over time are shown by different lines. (c) Temporal variation of the normalized peak intensities of the a_1 -analog band at $\sim 1080 \text{ cm}^{-1}$ for Ag-4ABT (empty circles) and Ag-4,4'DMAB (filled circles) shown versus laser irradiation time. (d) Temporal variation of the relative intensity of the b_2 -analog bands at $\sim 1433 \text{ cm}^{-1}$ with respect to the a_1 -analog band at $\sim 1080 \text{ cm}^{-1}$ in (a) and (b) shown versus laser irradiation time.

Figure 4(c) shows the temporal variation of the intensity of the a_1 -analog bands of Ag-4ABT (empty circles) and Ag-4,4'DMAB (filled circles), which are evident at

$\sim 1080\text{ cm}^{-1}$ in Figures 4(a) and (b), respectively. Initially, the a_1 -analog band of Ag-4,4'DMAB is at least three times as intense as that of Ag-4ABT. Over time, the intensity of the a_1 -analog band of Ag-4,4'DMAB decreases substantially, while the corresponding band of Ag-4ABT, though small, intensifies. After 20~30 min of laser irradiation, the intensity of the a_1 -analog band of Ag-4,4'DMAB is approximately equivalent to that of Ag-4ABT. Similar observations were made for the b_2 -analog bands; this is illustrated in Figure 4(d), which shows the temporal variation in the relative intensity of the b_2 -analog band at 1433 cm^{-1} and the a_1 -analog band at 1080 cm^{-1} . The initial intensity ratios were ~ 5.0 for Ag-4,4'DMAB (filled circles) and 0 for Ag-4ABT (empty circles). During laser irradiation, the ratio gradually decreased to 3.85 for Ag-4,4'DMAB and sharply increased to 3.85 for Ag-4ABT. That is, after 20~30 min of laser irradiation, the Raman spectral patterns of Ag-4ABT and Ag-4,4'DMAB became indistinguishable. Therefore, a reaction occurs under 514.5 nm irradiation that either convert 4-ABT to 4,4'-DMAB or 4,4'-DMAB to 4-ABT. As mentioned in Introduction, a few researchers have proposed that 4-ABT on Ag converts to 4,4'-DMAB with laser irradiation; this claim was based solely on the similarity of the SERS spectra [17-20]. The SERS spectral similarity is due to the conversion of 4,4'-DMAB on Ag to 4-ABT rather than from 4-ABT on Ag to 4,4'-DMAB [24,25]. One supporting evidence was that 4,4'-DMAB on Ag readily undergoes a coupling reaction with 4-cyanobenzoic acid to form amide bonds upon exposure to 514.5 nm radiation; this reaction did not proceed without laser irradiation [25].

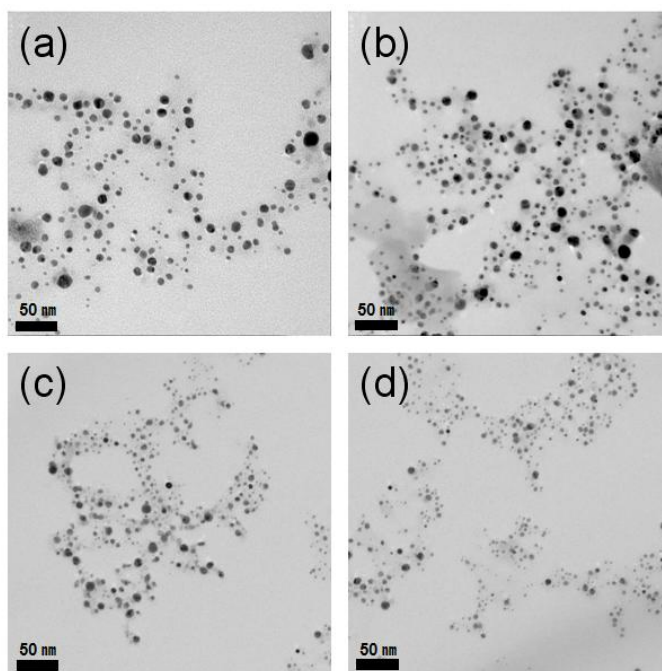


Figure 5. TEM images of Ag nanoparticles obtained from the photolysis of (a) Ag-4ABT and (b) Ag-4,4'DMAB using 514.5 nm radiation as excitation source, (c) Ag-4ABT and (d) Ag-4,4'DMAB using 632.8 nm radiation as excitation source, respectively.

A further evidence was that calcite crystals grew on 4,4'-DMAB on Ag only when exposed to 514.5 nm radiation, while the calcite crystals grow readily on 4-ABT on Ag even without radiation [25]. Since SERS-active Ag nanoparticles are produced from silver salts via laser irradiation (see Figure 5), the Raman spectra shown in Figures 4(a) and (b), which were measured under 514.5 nm irradiation, must be the SERS spectra of 4-ABT and 4,4'-DMAB on Ag, respectively [9]. Thus, the data shown in Figures 4(c) and (d) must be interpreted as characteristic of the photoinduced conversion of 4,4'-DMAB on Ag to 4-ABT.

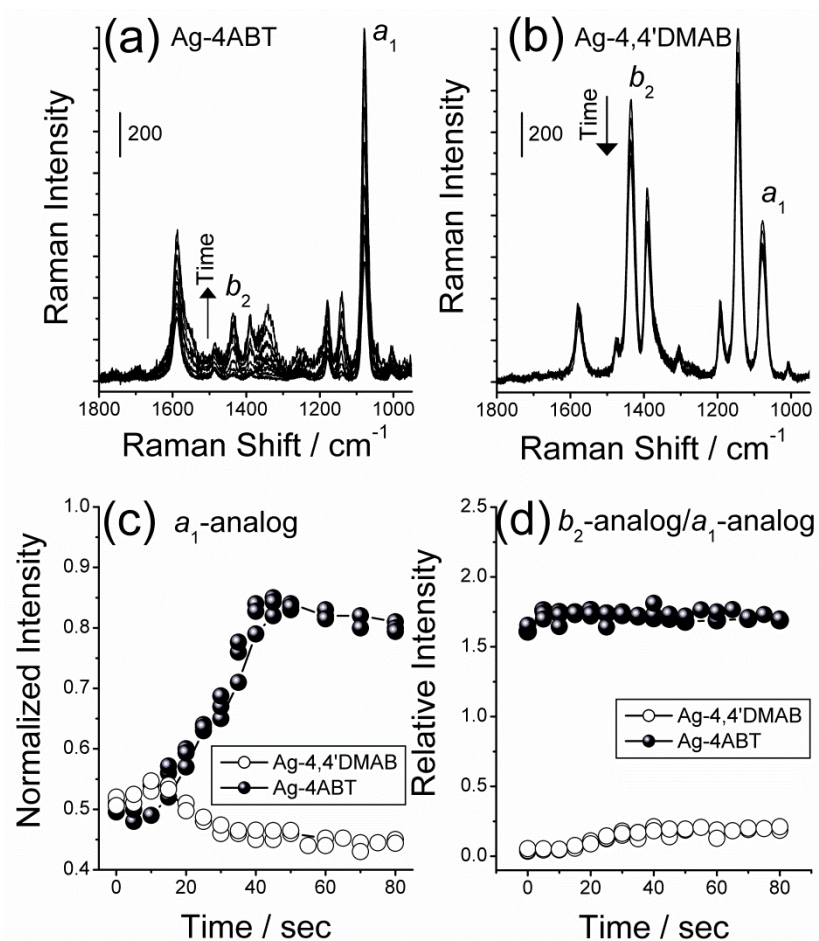


Figure 6. Temporally evolved Raman spectra of (a) Ag-4ABT and (b) Ag-4,4'DMAB under 632.8 nm light illumination and static conditions. Spectra measured over time are shown by different lines. (c) Temporal variation of the normalized peak intensities of the a_1 -analog band at $\sim 1080 \text{ cm}^{-1}$ for Ag-4ABT (empty circles) and Ag-4,4'DMAB (filled circles) shown versus laser irradiation time. (d) Temporal variation of the relative intensity of the b_2 -analog bands at $\sim 1433 \text{ cm}^{-1}$ with respect to the a_1 -analog band at $\sim 1080 \text{ cm}^{-1}$ in (a) and (b) shown versus laser irradiation time.

Under 632.8 nm irradiation, the changes in the Raman spectra of 4-ABT and 4,4'-DMAB Ag salts are not as significant as those under 514.5 nm irradiation. Figures

6(a) and (b) show the temporal evolution of the Raman spectra of Ag-4ABT and Ag-4,4'DMAB, respectively, that were measured in static conditions under 632.8 nm irradiation. The Raman peaks of Ag-4,4'DMAB decrease slightly, while those of Ag-4ABT increases in intensity, as shown in Figure 6(c), which displays the temporal intensity variation of the a_1 -analog band at $\sim 1080\text{ cm}^{-1}$ for Ag-4ABT (empty circles) and Ag-4,4'DMAB (filled circles). Figure 6(d) shows the variation of the relative intensity of the b_2 -analog band at $\sim 1433\text{ cm}^{-1}$ with respect to the a_1 -analog band at $\sim 1080\text{ cm}^{-1}$. The ratio remains fairly constant at ~ 0.1 for Ag-4ABT and ~ 1.7 for Ag-4,4'DMAB. Therefore, under 632.8 nm irradiation, the Raman spectral patterns of Ag-4ABT and Ag-4,4'DMAB remain dissimilar. The photoinduced conversion of Ag-4,4'DMAB on Ag to 4-ABT is thus unlikely to be significant under illumination with a 632.8 nm laser.

A possible explanation for this is that Ag nanoparticles are not produced by 632.8 nm light. However, this study has confirmed that 3~20 nm Ag nanoparticles were produced from all Ag thiolate salts by irradiation with either 514.5 or 632.8 nm light (see Figure 5). The observation that the b_2 -analog bands (in the region between 1100 and 1500 cm^{-1}) are not as intense in Figure 6(a) as in Figure 4(a) could be explained in terms of a small chemical enhancement of 4-ABT at 632.8 nm. The detailed mechanism of the photoconversion of Ag-4,4'DMAB to 4-ABT on Ag via 514.5 nm irradiation remains to be elucidated. It is well known that all silver thiolate salts produce Ag nanoparticles under visible-light irradiation, as seen in this work [9-11].

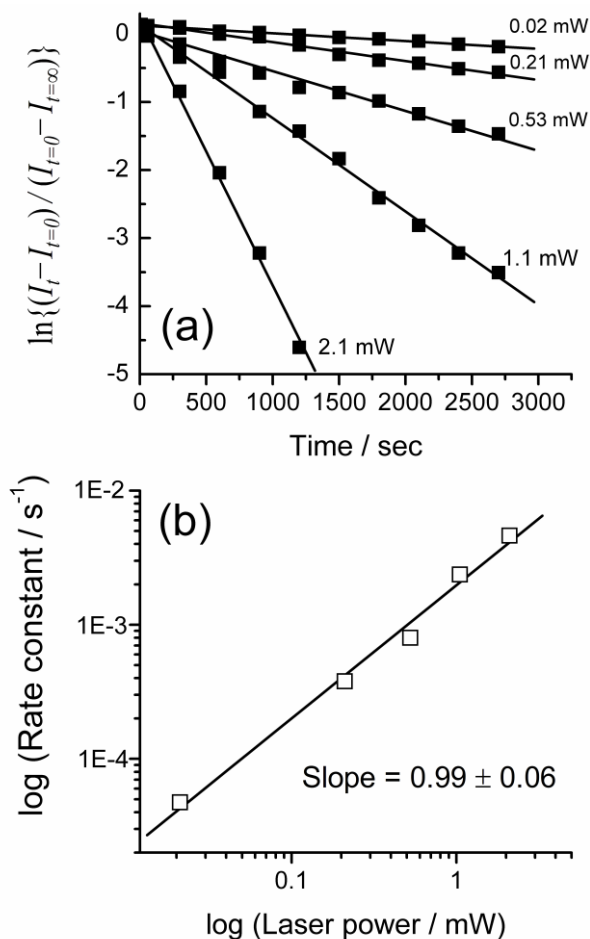


Figure 7. (a) The first-order kinetic plot for the photoreduction of Ag-4,4'DMAB to 4-ABT on Ag; I_t , $I_{t=0}$, and $I_{t=\infty}$ are the intensity ratios of the b_2 -analog band at $\sim 1433\text{ cm}^{-1}$ and the a_1 -analog band at $\sim 1080\text{ cm}^{-1}$ measured at time t , $t=0$, and $t=\infty$, respectively, after the irradiation of the 514.5 nm light at five different laser powers. (b) Log-log plot of the slope in (a) versus the laser power.

This reaction occurs via a reductive process. Therefore, it is likely that the first stage of the photoreaction includes the oxidation of thiolates to form disulfides, which are bound to Ag nanoparticles through Ag-S bonds. The measured Raman spectra must then correspond to the SERS spectra of the parent thiol molecules

adsorbed on Ag nanoparticles. Under illumination with a 514.5 nm laser, 4,4'-DMAB on Ag would further reduce, albeit slowly, to 4-ABT. Separately, the photoinduced conversion of Ag-4,4'DMAB to 4-ABT on Ag was found to occur at a rate that is 2.5 times faster than the rate of conversion of 4,4'-DMAB adsorbed on a citrate-reduced Ag nanoparticle film [24]. The faster conversion rate of the salt state could be indicative that fresh Ag nanoparticles are more efficient photoelectron emitters than aged ones [27,28]. Finally, this work examined the laser-power dependence of the photoreduction kinetics of Ag-4,4'DMAB.

Figure 6(a) shows a kinetic plot for typical experimental results after background correction. Here, $I_{t=\infty}$ means the intensity ratio of the b_2 -analog band at 1430 cm^{-1} and the a_1 -analog band at $\sim 1080\text{ cm}^{-1}$ after prolonged irradiation whereas I_t and $I_{t=0}$ are the same intensity ratio of b_2 -analog/ a_1 -analog but measured at time t and $t=0$, respectively, after the irradiation of the laser light at 514.5 nm. The data in Figure 4(d) indicates that the intensity ratio of 3.85 corresponds to full conversion of Ag-4,4'DMAB to 4-ABT on Ag. The intensity ratio, which started at ~ 5.0 ($I_{t=0}$), exponentially decreased to 3.85 ($I_{t=\infty}$) upon laser irradiation. The photoreduction of Ag-4,4'DMAB to 4-ABT on Ag may thus be presumed to be a unimolecular first-order reaction. Recalling that the Raman intensity of the product (or reactant) band depends on its concentration [29-31], a simple relationship between the SERS intensity ratio of Ag-4,4'DMAB to 4-ABT on Ag and the exposure time (t) is given by the following equation.

$$I_t - I_{t=\infty} = (I_{t=0} - I_{t=\infty})\exp(-kt)$$

The apparent rate constant k , in general, depends on the laser power (p), as $k = ap^n$, where n is the apparent number of laser photons required to initiate the photoreaction and a is a wavelength-dependent constant proportional to the absorption cross-section [29-31]. Accordingly, the natural logarithm of the difference of the intensity ratio should vary linearly with time. The photoreduction rate constant is then estimated from the slope of the initial decreasing part of the plot. A similar experiment was conducted at five different power levels; the power levels at the sampling position are 2.1, 1.1, 0.53, 0.21, and 0.02 mW, respectively. The rate constants at five different laser power levels were determined, and the resultant log-log plot is shown in Figure 6(b). The slope of this plot is 0.99 ± 0.06 . Since this value is close to 1, the photoinduced conversion of Ag-4,4'DMAB to 4-ABT on Ag is a single-photon process; however, a multi-photon process may be involved especially with radiation at wavelengths longer than 514.5 nm [29-31].

Summary and Conclusion

Ag thiolate is known to produce Ag nanoparticles upon irradiation with a visible laser; therefore, their Raman spectra usually correspond to the SERS spectra of their parent thiol molecules adsorbed on Ag. To elucidate the origin of the SERS spectral similarity of 4-ABT and 4,4'-DMAB on Ag, this work prepared 4-ABT and 4,4'-DMAB silver salts and examined their response to visible-light irradiation. From the XRD data, both Ag-4ABT and Ag-4,4'DMAB comprise a bilayer structure with a stoichiometric (1:1) composition of Ag(I) and 4-ABT or 4,4'-DMAB.

The intrinsic NR spectra of Ag-4ABT and Ag-4,4'DMAB were determined by measuring the Raman spectra with spinning at 3000 rpm. The most distinct spectral differences were in the region of 1100~1500 cm^{-1} , which contained three N=N stretching bands for Ag-4,4'DMAB, but was featureless for Ag-4ABT. Under static conditions, the Raman spectra of Ag-4ABT and Ag-4,4'DMAB evolved primarily due to the formation of SERS-active Ag nanoparticles. When the salts underwent 514.5 nm irradiation for 20~30 min, their Raman spectra became equivalent; the same effect did not occur with 632.8 nm irradiation. In light of the recent SERS study of 4,4'-DMAB on an Ag film, the spectral variation of Ag-4,4'DMAB under 514.5 nm radiation is a result of the formation of SERS-active Ag nanoparticles followed by photoinduced reduction of 4,4'-DMAB on Ag to 4-ABT. Ag nanoparticles produced in situ were more efficient photoelectron emitters under 514.5 nm radiation than aged ones. These observations clearly indicate that the appearance of the b_2 -type bands in the SERS of 4-ABT can be completely attributed to the chemical enhancement mechanism.

References

1. Kagan, C. R.; Mitzi, D. B.; Dimitrakopoulos, C. D. *Science* **1999**, *286*, 945.
2. Dance, I. G.; Fisher, K. J.; Banda, H.; Scudder, M. L. *Inorg. Chem.* **1991**, *30*, 183.
3. Baena, M. J.; Espinet, P.; Lequerica, M. C.; Levelut, A. M. *J. Am. Chem. Soc.* **1992**, *114*, 4182.

4. Fijolek, H. G.; Grohal, J. R.; Sample, J. L.; Natan, M. J. *Inorg. Chem.* **1997**, *36*, 622.
5. Binnemans, K.; Van Deun, R.; Thijs, B.; Vanwelkenhuysen, I.; Geuens, I. *Chem. Mater.* **2004**, *16*, 2021.
6. Hu, L.; de la Rama, L. P.; Efremov, M. Y.; Anahory, Y.; Schiettekatte, F.; Allen, L. H. *J. Am. Chem. Soc.* **2011**, *133*, 4367.
7. Lee, S. J.; Han, S. W.; Choi, H. J.; Kim, K. *J. Phys. Chem. B* **2002**, *106*, 2892.
8. Lee, S. J.; Kim, K. *Chem. Commun.* **2003**, 212.
9. Seo, Y. U.; Lee, S. J.; Kim, K. *J. Phys. Chem. B* **2004**, *108*, 4000.
10. Lee, Y. M.; Kim, K.; Shin, K. S. *J. Phys. Chem. C* **2008**, *112*, 10715.
11. Kim, K.; Lee, Y. M.; Lee, H. B.; Park, Y.; Bae, T. Y.; Jung, Y. M.; Choi, C. H.; Shin, K. S. *J. Raman Spectrosc.* **2010**, *41*, 187.
12. Abe, K.; Hanada, T.; Yoshida, Y.; Tanigaki, N.; Takiguchi, H.; Nagasawa, H.; Nakamoto, M.; Yamaguchi, T.; Yase, K. *Thin Solid Films* **1998**, *327*, 524.
13. Geuens, I.; Vanwelkenhuysen, I. *J. Imaging Sci. Technol.* **1999**, *43*, 521.
14. Furutani, M.; Kudo, K. *J. Mater. Chem.* **2012**, *22*, 3139.
15. Zhang, R.; Lin, W.; Moon, K.-S.; Wong, C. P. *ACS Appl. Mater. Interfaces* **2010**, *2*, 2637.
16. Osawa, M.; Matsuda, N.; Yoshii, K.; Uchida, I. *J. Phys. Chem.* **1994**, *98*, 12702-12707.
17. Fang, Y.; Li, Y.; Xu, H.; Sun, M. *Langmuir* **2010**, *26*, 7737.
18. Huang, Y. F.; Zhu, H. P.; Liu, G. K.; Wu, D. Y.; Ren, B.; Tian, Z. Q. *J. Am. Chem. Soc.* **2010**, *132*, 9244.

19. Huang, Y. F.; Wu, D. W.; Zhu, H. P.; Zhao, L. B.; Liu, G. K.; Ren, B.; Tian, Z. *Q. Phys. Chem. Chem. Phys.* **2012**, *14*, 8485.
20. Sun, M.; Huang, Y.; Xia, L.; Chen, X.; Xu, H. *J. Phys. Chem. C* **2011**, *115*, 9629.
21. Ikeda, K.; Suzuki, S.; Uosaki, K. *Nano Lett.* **2011**, *11*, 1716.
22. Zhou, Q.; Li, X.; Fan, Q.; Zhang, X.; Zheng, J. *Angew. Chem. Int. Ed.* **2006**, *45*, 3970.
23. Ye, J.; Hutchison, J. A.; Uji-i, H.; Hofkens, J.; Lagae, L.; Maes, G.; Borghsa, G.; Van Dorpea, P. *Nanoscale* **2012**, *4*, 1606.
24. Kim, K.; Kim, K. L.; Lee, H. B.; Shin, K. S. *J. Phys. Chem. C* **2012**, *116*, 11635.
25. Kim, K.; Kim, K. L.; Shin, K. S. *Langmuir* **2012**, In Press.
26. Kim, K.; Shin, D.; Choi, J.-Y.; Kim, K. L.; Shin, K. S. *J. Phys. Chem. C* **2011**, *115*, 24960.
27. Jana, N. R.; Sau, T. K.; Pal, T. *J. Phys. Chem.* **1999**, *103*, 115.
28. Henglein, A. *Chem. Rev.* **1989**, *89*, 1861.
29. Suh, J. S.; Jang, N. H.; Jeong, D. H.; Moskovits, M. *J. Phys. Chem.* **1996**, *100*, 805.
30. Joo, T. H.; Yim, Y. H.; Kim, K.; Kim, M. S. *J. Phys. Chem.* **1989**, *93*, 1422.
31. Kim, K. L.; Lee, S. J.; Kim, K. *J. Phys. Chem. B* **2004**, *108*, 9216.

IV. Appendix

List of Publications

1. Kwan Kim,* **Kyung Lock Kim**, and Kuan Soo Shin, "Visible-Light Response of 4-Aminobenzenethiol and 4,4'-Dimercaptoazobenzene Silver Salts" **2012**, Submitted.
2. Kwan Kim,* **Kyung Lock Kim**, and Kuan Soo Shin, "Photoreduction of 4,4'-Dimercaptoazobenzene on Ag Revealed by Raman Scattering Spectroscopy" *Langmuir* **2012**, in Press.
3. Kwan Kim,* Seung Hun Lee, **Kyung Lock Kim**, and Kuan Soo Shin, "Visible Light Response of Silver 4-Aminobenzenethiolate and Silver 4-Dimethylaminobenzenethiolate Probed by Raman Scattering Spectroscopy", *J. Raman Spectrosc.*, **2012**, in Press.
4. Kwan Kim,* Dongha Shin, **Kyung Lock Kim**, and Kuan Soo Shin, "Surface Potential Variation of Gold Nanoparticles by Organic Vapors Revealed by Raman Scattering of 1,4-Phenylenediisocyanide", *J. Raman Spectrosc.*, **2012**, *43*, 1427-1431.
5. Kwan Kim,* **Kyung Lock Kim** and Kuan Soo Shin, "Selective Detection of Aqueous Nitrite Ions by Surface-enhanced Raman Scattering of 4-Aminobenzenethiol on Au", *Analyst* **2012**, *137*, 3836-3840.
6. Kwan Kim,* **Kyung Lock Kim**, Hyang Bong Lee and Kuan Soo Shin, "Similarity and Dissimilarity in Surface-Enhanced Raman Scattering of 4-Aminobenzenethiol, 4,4'-Dimercaptoazobenzene, and 4,4'-

- Dimercaptohydrazobenzene on Ag", *J. Phys. Chem. C* **2012**, *116*, 11635-11642.
7. Kwan Kim,* Dongha Shin, **Kyung Lock Kim** and Kuan Soo Shin, "Surface-Enhanced Raman Scattering of 4,4'-Dimercaptoazobenzene Trapped in Au Nanogaps", *Phys. Chem. Chem. Phys.*, **2012**, *14*, 4095-4100.
 8. Kwan Kim,* **Kyung Lock Kim** and Kuan Soo Shin, "Surface Characteristics of Ag-Doped Au Nanoparticles Probed by Raman Scattering Spectroscopy", *J. Raman Spectrosc.*, **2012**, *43*, 228-236.
 9. Kwan Kim,* **Kyung Lock Kim**, Dongha Shin, Jeong-Yong Choi and Kuan Soo Shin, "Surface-Enhanced Raman Scattering of 4-Aminobenzenethiol on Ag and Au: pH Dependence of ν_2 -Type Bands", *J. Phys. Chem. C* **2012**, *116*, 4774-4779.
 10. Kwan Kim,* Dongha Shin, Jeong-Yong Choi, **Kyung Lock Kim**, and Kuan Soo Shin, "Surface-Enhanced Raman Scattering Characteristics of 4-Aminobenzenethiol Derivatives Adsorbed on Silver", *J. Phys. Chem. C* **2011**, *115*, 24960-24966.
 11. Kwan Kim,* **Kyung Lock Kim**, and Kuan Soo Shin, "Co-reduced Pt/Ag Alloy Nanoparticles: Surface-Enhanced Raman Scattering and Electrocatalytic Activity", *J. Phys. Chem. C* **2011**, *115*, 23374-23380.
 12. Kwan Kim,* **Kyung Lock Kim**, Jeong-Young Choi, Dongha Shin, and Kuan Soo Shin, "Effect of Volatile Organic Chemicals on Surface-enhanced Raman Scattering of 4-Aminobenzenethiol on Ag: Comparison

- with the Potential Dependence", *Phys. Chem. Chem. Phys.*, **2011**, *13*, 15603-15609.
13. Kwan Kim,* **Kyung Lock Kim** and Kuan Soo Shin, "Co-reduced Ag/Pd Bimetallic Nanoparticles: Surface Enrichment of Pd Revealed by Raman Spectroscopy", *J. Phys. Chem. C* **2011**, *115*, 14844-14851.
 14. Kwan Kim,* Hyang Bong Lee, Jeong-Yong Choi, **Kyung Lock Kim** and Kuan Soo Shin, "Surface-Enhanced Raman Scattering of 4-Aminobenzethiol in Nanogaps between a Planar Ag Substrate and Pt Nanoparticles", *J. Phys. Chem. C* **2011**, *115*, 13223-13231.
 15. Kwan Kim,* **Kyung Lock Kim**, Jeong-Yong Choi and Kuan Soo Shin, "Effect of Organic Vapors and Potential-Dependent Raman Scattering of 2,6-Dimethylphenylisocyanide on Platinum Nanoaggregates", *Phys. Chem. Chem. Phys.*, **2011**, *13*, 5981-5986.
 16. Kwan Kim,* **Kyung Lock Kim**, Hyang Bong Lee and Kuan Soo Shin, "Surface-Enhanced Raman Scattering on Aggregates of Platinum Nanoparticles with Definite Size", *J. Phys. Chem. C* **2010**, *114*, 18679-18685.
 17. Kwan Kim,* **Kyung Lock Kim**, Dongha Shin, Ji Won Lee and Kuan Soo Shin, "Effect of Polar Organic Vapors on Surface Potential of Au Nanoparticle Aggregates Probed By Surface-Enhanced Raman Scattering of 2,6-Dimethylphenylisocyanide", *Chem. Comm.*, **2010**, *46*, 3753-3755.
 18. Kwan Kim,* Ji Won Lee, Dongha Shin, **Kyung Lock Kim** and Kuan Soo Shin, "Surface Potential of Au Nanoparticles Affected by Layer-by-Layer

Deposition of Polyelectrolytes: A Surface-Enhanced Raman Scattering Study", *J. Phys. Chem. C* **2010**, *114*, 9917-9922.

19. Kwan Kim,* Dongha Shin, **Kyung Lock Kim**, and Kuan Soo Shin, "Electromagnetic field enhancement in the gap between two Au nanoparticles: the size of hot site probed by surface-enhanced Raman scattering", *Phys. Chem. Chem. Phys.*, 2010, *12*, 3747-3752.
20. Kwan Kim,* **Kyung Lock Kim**, Jeong-Yong Choi, Hyang Bong Lee, and Kuan Soo Shin, "Surface Enrichment of Ag Atoms in Au/Ag Alloy Nanoparticles Revealed by Surface-Enhanced Raman Scattering of 2,6-Dimethylphenyl Isocyanide", *J. Phys. Chem. C* **2010**, *114*, 3448-3453.

List of Presentations

· International conferences

1. **Kyung Lock Kim**, Kuan Soo Shin, Kwan Kim, "Co-reduced Pt/Ag Alloy Nanoparticles: Surface-Enhanced Raman Scattering and Electrocatalytic Activity" *The Second International Advances in Applied Physics and Materials Science (APMAS)*, Antalya, Turkey, 2012, 04, 26 – 29, Poster presentation.
2. **Kyung Lock Kim**, Kuan Soo Shin, Kwan Kim, "Effect of Volatile Organic Chemicals on Surface-enhanced Raman Scattering of 4-Aminobenzenethiol on Ag: Comparison with the Potential Dependence", *The Third Asian Spectroscopy Conference (ASC)*, Xiamen, China, 2011, 11, 28 – 12, 01, Poster presentation.

3. **Kyung Lock Kim**, Kuan Soo Shin, Kwan Kim, “Surface-Enhanced Raman Scattering on Aggregates of Platinum Nanoparticles with Definite Size”, *The Asian CORE Winter School* , OKAZAKI, Japan, 2011, 02,19 – 2011, 02, 22, Poster presentation.

·Domestic conferences

1. **Kyung Lock Kim**, Kuan Soo Shin, Kwan Kim, “Co-reduced Ag/Pd Bimetallic Nanoparticles: Surface Enrichment of Pd Revealed by Raman Spectroscopy”, *The 108th Annual Meeting of the Korean Chemical Society (KCS)*, Convention Center, Daejun, Korea, 2011, 08, Poster presentation.
2. **Kyung Lock Kim**, Kuan Soo Shin, Kwan Kim.*, “Surface Enrichment of Ag Atoms in Au/Ag Alloy Nanoparticles Revealed by Surface-Enhanced Raman Scattering of 2,6-Dimethylphenyl Isocyanide”, *The 105th Annual Meeting of the Korean Chemical Society (KCS)*, Songdo convensiA, Incheon, Korea, 2010, 02, Poster presentation.

Abstract (Korean)

주조 금속으로 만들어진 나노구조체에 분자가 흡착하면 분자의 라만 산란 세기가 백만 배 이상 증가하는 데 이를 표면 증강 라만 산란 (SERS)이라 하며 나노 표면 분석법의 하나로 각광을 받고 있다. SERS 현상은 크게 두 가지 이론으로 설명하고 있다. 고전 전자기 이론에 따라 나노구조체 부근에서 전자기장이 증가하기 때문이라는 전자기장 증대 이론과 분자가 나노구조체에 화학 흡착하면 새로운 에너지 준위가 형성되어 나노구조체에서 분자로 또는 분자에서 나노구조체로의 전자 전이가 가능한 새로운 공명 라만 산란을 통해 라만 산란 세기가 증가할 수 있다는 화학적 증강 이론이다. 실제 상황에서는 두 가지 경우가 모두 발생하고 있는데 실험적으로 두 효과를 구분해 내는 것이 용이하지는 않다.

4-아미노벤젠치올 (4-ABT) 분자는 특이한 분자이다. 분자 자체의 정규 라만 (NR) 산란에서는 a_1 유형의 진동 띠만이 관찰된다. 그런데 가령 은에 흡착하게 되면 $1100-1500\text{ cm}^{-1}$ 영역에 a_1 띠로 볼 수 없는 강한 진동 띠들이 3-4 개 나타나며 그 원인이 최근 논란의 대상이 되고 있다. 일찍이 일본의 Osawa 교수 연구진은 전위-의존성 SERS 연구를 기반으로 위의 진동 띠들이 4-ABT 자체의 고유 b_2 유형 진동 띠이며, SERS 스펙트럼에 나타나는 것은 화학 증강에 의한 것으로 Herzberg-

Teller 유형의 intensity-borrowing 이 관여하기 때문으로 해석하였다. 그러나 약 2 년 전 중국 연구진들은 b_2 유형 진동 띠가 4-ABT 에 의한 것이 아니라 금속 표면 유발 광 촉매 반응으로 생성되는 4,4'-다이머캡토아조벤젠 (DMAB)의 N=N 신축 진동 띠 때문이라고 주장하였다. 많은 연구자들이 새로운 주장에 동조하는 추세에 있을 때, 본 연구실에서는 다년간 수행해 온 귀금속 나노 틴체에서의 4-ABT SERS 연구를 기초로써 열역학적으로 불안정한 시스 형태의 아조벤젠이 형성되기는 어렵다고 보고 b_2 -유형의 진동 띠가 반응 생성물에 기인하지는 않을 것으로 판단하였다. 본 연구실의 전임자는 b_2 -유형의 진동 띠는 4-ABT 뿐만 아니라 4-ABT 의 유도체 있는 아민기에서 수소가 탄소나 질소로 바뀐 화합물의 SERS 에서도 광 반응과 무관하게 NR 에 없는 b_2 -유형의 진동 띠가 나타남을 발견한 바 있다. 이전 연구의 연장 선상으로 본 연구에서는 4-ABT 와 DMAB 의 SERS 를 직접 비교해 보는 방법으로 유사성과 이질성을 구체적으로 살펴보았다.

관련 연구와 직접 연구로 대별한다면 관련 연구로는, 첫째, 은 나노구조체에서는 광 반응이 잘 일어나는 4-니트로벤젠치올이 일반적으로 촉매로 많이 사용되고 있는 백금 나노구조체에서는 광 반응이 일어나지 않음을 SERS 로 확인하였다. 그런데 4-ABT 의 경우엔 여전히 b_2 -유형의 진동 띠가 관찰되었다. 이러한 결과는 b_2 -유형의

진동 띠가 4-ABT 에 의한 것임을 암시한다고 판단하였다. 둘째, 4-ABT 가 흡착된 은 전극에 아세톤이나 암모니아 등 휘발성 유기물을 노출하면 b_2 -유형 진동 띠의 크기가 반복적으로 감소와 증가를 하게 되는데 이것은 마치 전위-의존성 SERS 와 유사한 형태를 보이게 됨을 관찰하였다.

4-ABT 와 DMAB 의 직접 비교 연구로는 첫째, DMAB 의 SERS 스펙트럼은 용액의 pH 가 산성에서 염기성이 될 때 주목할만한 변화를 나타내지 않으나 4-ABT 에서는 b_2 -유형의 진동 띠가 산성에서는 약해지든가 사라지고 염기성에서는 크게 나타나는 것이 반복적으로 관찰되었다. 이러한 결과는 b_2 -유형의 진동 띠가 광 반응 생성물에 기인하지 않기 때문으로 판단하였다. 둘째, 은 표면에 흡착된 4-ABT 와 DMAB 그리고 이 분자의 유사체인 4,4'-다이머캡토히드로아조벤젠 (DMHAB)의 SERS 를 비교해 보았는데 대기 환경에서는 모든 스펙트럼 패턴이 상당히 유사였다. 반면에 전위를 아주 낮춰주거나 진한 borohydride 용액으로 처리하면 DMAB 의 SERS 스펙트럼 패턴이 4-ABT 와 같아짐을 발견하였다. 그러나 DMHAB 는 아무런 변화가 없었다. 대기 환경 하에서도 초록색 가시광선 레이저를 장시간 쬐여주면 DMAB 가 4-ABT 로 광 환원이 일어남을 발견하였다. 광 환원이 일어나 4-ABT 로 변환됨은 아마이드 커플링 반응과 선택적 탄산칼슘 성장으로도 확인하였다.

결론적으로, 4-ABT 와 DMAB 의 SERS 를 직접 비교하는 실험을 통해 4-ABT 의 SERS 에 나타나는 b_2 -유형의 진동 띠는 광 반응 생성물이 아니라 4-ABT 자체의 고유 진동 띠로 Osawa 가 주장한 바와 같이 화학증강에 의해 나타나게 됨을 알 수 있었다. pH 효과 등은 양자 계산을 통해 양성자가 아민기에 붙게 되면 LUMO 에너지가 높아져 금속에서 분자로의 전하-이동이 어려워지기 때문에 b_2 -유형의 진동 띠가 약해진다고 해석할 수 있었다.

주요어: 라만 분광, 표면 증강 라만 산란, 전자기장 효과, 화학적 효과, 4-아미노벤젠치올, 4,4'-다이머캡토아조벤젠

학번: 2009-30486